ON THE COVER

In 1914, physicist Ernest Rutherford proved that gamma rays were a form of high-energy electromagnetic radiation. Though Frenchman Paul Villard was credited with their discovery, it was Rutherford, then at McGill University, who gave them their name in 1903 and worked to understand their properties.

The penetrating properties of gamma rays are now used in broad applications such as life-saving gamma knife surgeries, and their detection is a key part of understanding astronomical phenomena in our universe. In this issue, on pg. 17, we feature a novel heptagonal gamma ray detector, born from the Rutherford Physics Building at McGill University — 100 years on.

McGill Science Undergraduate Research Journal

THE 2013 - 2014 MSURJ COMMITTEE

Editors-in-Chief
Yuhao Shi
Computer Science and Biology

Janine Hsu
Interdepartmental Honours Immunology

Managing Editor
Debbie Wang
Psychology

Associate Editors
Blair Jia
Quantitative Biology

Brian Krug
Biology

Jassi Pannu
Honours Biology

Chief Journalist
Kate Sheridan
Honours Cognitive Science

Senior Editors
Ariana Aimani
Computer Science and Biology

Deborah Baremberg
Cognitive Science

Kaien Gu
Biochemistry

Kevin Liang
Neuroscience

Farah Musharbash
Physiology

Kate Sheridan
Honours Cognitive Science

Junior Editors
Kuan-Ting (Michael) Chen
Honours Physiology

Sapan Patel
Physiology

Adam Pietrobon
Biochemistry

Tatiana Sanchez
Psychology

Manjot Sangha
Biochemistry & Computer Science

Assistant Editor:
Danielle Toccalino
Cognitive Science

Faculty of Science Advisor:
Victor Chisholm
Office for Undergraduate Research in Science

Layout Designer
Clayton Nguyen

Graphic Designer
Irene Xie

805 Sherbrooke St. West Room 1B21
Montréal, Québec, H3A 2K6 Canada
Phone: (514) 398-6979
Fax: (514) 398-6766
Email: mcgillsurj@gmail.com
Website: msurj.mcgill.ca

TABLE OF CONTENTS

FOREWORD

DEAR READER,

Each year, we never ceased to be amazed by the exceptional research done by undergraduate students here at McGill University. It has been a privilege for the McGill Science Undergraduate Research Journal to share the inspiring work of young scientists with the student body.

The two us have been part of MSURJ for nearly half of its existence. These four years have been an experiment, in which we tested many hypotheses, and was not always assured that our efforts would yield expected results. But the vision of the MSURJ editorial board remains the same — to inspire students to pursue their scientific interests. In our effort on this front, we introduced tutorials on lab-related skills in our Outreach Program. Our online blog, The Abstract (msurjblog.com), also continues to engage students of all disciplines in the discussion of science.

As you read this year's journal, we hope that the works of your peers will kindle your inner curiosity and encourage you to dive into the boundless world of research.

YUHAO SHI AND JANINE HSU

EDITORS-IN-CHIEF

ACKNOWLEDGEMENTS

The publication of the McGill Science Undergraduate Research Journal would not have been possible without the support and contribution of many individuals.

We thank Professor Martin Grant, Dean of the Faculty of Science, whose unwavering support throughout the past nine years has allowed this journal to flourish. We also extend our gratitude to Mr. Victor Chisholm for providing us with continued encouragement and valuable advice.

We thank all of our donors in the McGill community for their generous support:

- Faculty of Science
- Faculty of Medicine
- Biochemistry Department
- McGill School of Environment
- Science Undergraduate Society
- McGill Immunology Student Association
- McGill Anatomy and Cell Biology Student Society
- Biochemistry Undergraduates
- McGill Physics Students Association

We wish to thank the professors and post-doctoral fellows who graciously offered their time to review students' article submissions.

We would like to acknowledge the tireless efforts of the MSURJ board of editors in assembling this edition of the journal.

Lastly, we wish to recognize the student contributors whose commendable efforts have made this journal possible

RESEARCH ARTICLE

Parrotfish Body Size As An Indicator of Diurnal Fish Species Richness On Fringing Coral Reefs in Barbados.

Aaron Eger[1]*, Catherine Pigeon-Dubeau[2], Lauriane Sibileau[3],

[1] McGill School of Environment, McGill University, Montreal, QC, Canada
[2] School of Environment, McGill University, Montreal, QC, Canada
[3] Department of Biology, McGill University, Montreal, QC, Canada

*Email Correspondence:
aaron.eger@mail.mcgill.ca

Keywords
Coral reefs: *Tropical and subtropical marine ecosystems containing a wide diversity of life.*
Parrotfish: *An abundant grouping of reef fish found in many different locations, known ecosystem engineers.*
Biodiversity: *the variety of different species in an ecosystem*

Abstract

Background: Coral reefs around the world are host to some of the most condensed and varied ecosystems. However, over the past decades, their biodiversity has alarmingly decreased. A rapid and reliable way of assessing their status is urgently needed to monitor and prevent their decline. The purpose of this study is to assess whether or not family *Scaridae* (common name: parrotfish) body size can be used as an index to evaluate the diurnal fish diversity on coral reefs.

Methods: We selected 6 accessible reefs on the West coast of Barbados and measured the size of parrotfish we encountered, as well as the number of fish species present on the reef; this data was then plotted and statistically analyzed to establish a possible correlation.

Results: Our results show that reef fish species richness is strongly correlated to both the ratio of large to small parrotfish and the average parrotfish size. It is however the large to small ratio that exhibited the strongest relationship. Further analysis revealed that the population size of large parrotfish correlates with reef biodiversity with a Pearson's r coefficient of 0.97.

Conclusion: This relationship could be due to the fact that large parrotfish (greater than or equal to 20 cm) have increased grazing rates compared to smaller ones, this increased grazing promotes coral polyp recruitment, thereby benefiting the diversity observed on coral reefs. Further research is needed to elucidate whether these results can be extended to other areas of the Caribbean and provide conservation efforts with an easy tool to survey and protect coral reef ecosystems.

Introduction

Barbados is an island nation situated in the western part of the North-Atlantic, around 13°N and occupies 429 km^2. As a seafaring country, fishing has traditionally been an integral source of employment and income for the nation. Mohammed *et al*. (1) found that in recent years the fishing industry has expanded in fleet size, landings, and species targeted. The same study explains that as a result of the heavy reliance on fishing and the small size of the country, many of the fisheries, including the shallow-shelf reef fisheries which target species such as parrotfish, surgeonfish, triggerfish and grunts, are considered overexploited. Once the top predators are depleted, fishermen proceed to hunt the smaller herbivorous parrotfish. The family *Scaridae* includes over ninety species of herbivorous, day-time active (diurnal) fish that graze primarily on algae-coated corals (2). We encountered 4 species in the sampled area: stoplight parrotfish (*Sparisoma viride)*, princess parrotfish (*Scarus taeniopterus*), redband parrotfish (*Sparisoma aurofrenatum*), and striped parrotfish (*Scarus iserti*). Because this family of fish is widespread and populous throughout the Caribbean it would make a convenient indicator species for the region (2). Parrotfish are also tied to the reef ecosystem through their role as algae grazers (3); in this way their presence can be representative of a healthy, low algae reef system (3). Additionally, if parrotfish are being harvested, this is indicative of overharvesting of larger, commercially valuable fish species (4). The need for an adequate and efficient indicator species is all the more vital given the current abasement of coral reefs worldwide (5). Such an indicator of reef fish diversity would permit a rapid assessment of reefs with abundant diurnal reef fish species,

allowing targeted conservation and preservation efforts.

It has already been shown by Vallès and Oxenford (4) that parrotfish size can be used as an index to estimate the fishing pressure and species abundance of large piscivorous fish, such as groupers and snappers upon which pelagic fisheries depend. They demonstrated that *Scaridae* body size and both fishing pressures and the secondary consequences of harvesting (ie. fewer piscivorous fish) are consistently negatively correlated (4). Since parrotfish are typically only fished after the piscivorous fish are depleted, their decline can be seen as a larger indicator of overall fish decline (4). Building on this, we are interested in determining if parrotfish body size structure within a population can be more broadly used as an indicator of the richness of diurnal fish species on a particular reef. Previous studies claim that as the parrotfish size exceeds 20 cm, its grazing rate drastically increases (3). If the overall grazing rate of a parrotfish community is be reduced, the result will likely be a growth in algal cover over reefs, reduced coral polyp recruitment, less reef growth, and fewer reef systems to support fish species (3). This threshold was the basis of our large to small analysis.

In this study, we assessed the body size of parrotfish, the structure of that body size within the community (proportion of the population to occupy different size classes) and the total number of diurnal reef fish species; the latter being the most widely used diversity measure in literature (6). This was done on 6 reefs along the West coast of Barbados to determine the presence or absence of a relationship between these variables. In order to capture variation in fish body size, we sampled three sites in a marine protected area (MPA) and three located in non-protected marine areas, this protected area was found to have a reduced fishing effort of 70% or greater compared to the surrounding non-protected areas (7). We expected larger and more populous parrotfish communities to reside in the protected areas due to the lack of or reduced fishing stressor (8). Ultimately, we predict that the larger the size of the parrotfish on the reef, the higher the species richness of fish will be. Two different measures for parrotfish size are used: 1) mean parrotfish body size, and 2) the ratio of large to small parrotfish, with the cutoff for large being greater than or equal to 20 cm. The two models were compared to determine which metric is a more rigorous predictor of biodiversity on the reef.

Methods

The 6 chosen sites were sampled over four days from May 17-20th, 2013. They had to be accessible using snorkeling gear, which restricted sampling to fringing reefs on the West coast of Barbados. Sites were chosen in an effort to survey areas with different amounts of fish species yet similar physical composition. We chose to assess 6 sites, three of which were located in the Folkestone Marine Reserve (hereinafter referenced to as Bellairs South, Bellairs North and Discovery Bay) and three in unprotected areas (Gibbes Beach, Sandy Lane and Batts Rock Beach).

Fish Sampling

We randomly and continuously snorkeled throughout each reef at a pre-practiced speed. One person assessed the *Scaridae* body size, another counted the number of fish species, while the last person held a watch and signaled every minute to the two others. This design was repeated thrice on each reef in order to have every person play all roles once and mitigate for possible observer bias.

Encountered parrotfish were identified according to species. Four different species were counted in our observations. These were: the redband parrotfish, the princess parrotfish, the spotlight parrotfish and the striped parrotfish. To estimate *Scaridae* body size, we first trained ourselves to evaluate the length of 30 and 60 centimeter sticks underwater. This was done to help account for the 33% magnification of objects under water (9). Once on the reef, we evaluated the length of each parrotfish we encountered and recorded it on an underwater slate, as the number of fish found per 5 cm fish length intervals. Each person scanned for Scaridae size on each reef for a set total time of ten minutes.

To assess the fish diversity on the reef, one person would record on a slate the number of new fish species seen every minute. This was done to establish a saturation curve of species richness. The biodiversity count would end after having assessed zero new species per minute, three times in a row or five times cumulatively, for a minimum sampling time of 10 minutes. The sites sampled for the longest periods were Bellairs North and South reefs which were both surveyed for 23 minutes, the shortest was Gibbes at 13 minutes, in between Discovery was 16 minutes, Sandy Lane and Batts were both 17 minutes.

Statistical Analysis

We calculated Pearson's r correlation coefficient between species richness variables and the ratio of large to small parrotfish, as well as the correlation coefficient (r) between species richness and average parrotfish size. We then calculated the significance of the results with α set at 0.05. Coefficients of determination (R^2) for our two models were also determined. This was done in order to establish which metric (the large-to-small ratio or the average size) would best describe general fish richness on a reef. Lastly, a one-way analysis of variance with α equals 0.05 was used to determine if there was a statistical significant difference in mean parrotfish abundance, average parrotfish size, diurnal reef fish species richness and large to small parrotfish ratio between protected and non-protected sites.

Results

Our parrotfish population size measurements showed relatively uniform distributions at all six sites. We also found a diminishing rate of discovery of new species over time (Fig. 1). Table 1 shows the variation in species abundance, average parrotfish size and other measured variables over the surveyed sites. The protected reefs possessed substantially greater parrotfish population than their non-protected counterparts. The non-protected sites showed smaller parrotfish abundance [$F(1,16)=18.04$, $p=0.001$)], lower large-to-small parrotfish ratios, smaller parrotfish size on average [$F(1,16)=15.80$, $p=0.001$)], and lower diurnal species richness [$F(1,16)=14.55$, $p=0.002$] all in comparison to the protected sites using a one-way ANOVA, $\alpha = 0.05$ (Table 2). The difference in parrotfish size, parrotfish abundance, and species diversity between the non-protected sites in the south (Batts Rock Beach and Sandy Lane) and the non-protected site in the north (Gibbes Beach) was not significant at $\alpha=0.05$ (ANOVA).

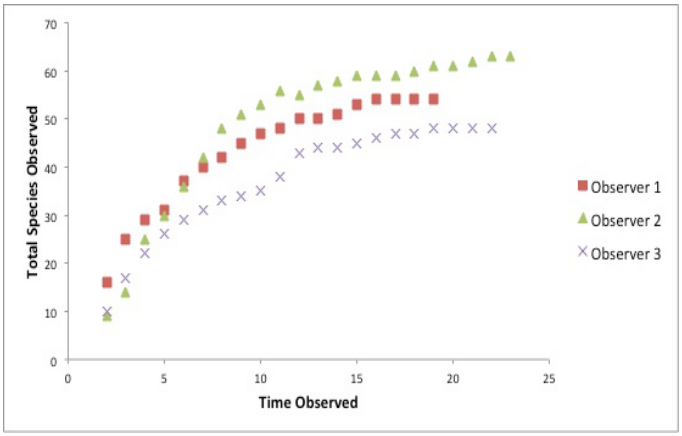

Fig. 1
Saturation curve from Bellairs North Reef, demonstrating the diminishing rate of discovery of species over time.

Site	Average Dirunal Reef Fish Species Richness	Parrotfish Average Length (cm)	Average Parrotfish Abundance	Average Number of Large	Average Number of Small	Large-Small Ratio	Average Proportion of Small Parrotfish	Average Proportion of Large Parrotfish
Bellairs South	54.33	23.35	34.33	53.00	24.00	2.21	0.31	0.69
Bellairs North	54.67	29.29	26.00	56.00	22.00	2.55	0.28	0.72
Discovery Bay	35.00	23.73	17.00	24.00	27.00	0.89	0.53	0.47
Gibbes Beach	21.67	11.00	8.33	1.00	24.00	0.04	0.96	0.04
Sandy Lane Bay	37.00	23.96	16.00	25.00	23.00	1.09	0.48	0.52
Batts Rock Beach	30.67	10.56	3.00	1.00	9.00	0.11	0.90	0.10

Table 1
Summary of general results obtained from the 6 sampled sites. This includes measurements like species richness, average parrotfish length and ratios of small to large and large to small parrotfish.

a) Parrotfish Abundance

	Protected	Non-Protected	
Mean	25.78	9.11	
Standard Deviation	10.08	6.07	
Degrees of Freedom		ANOVA	
Between Groups	1	P-Value	0.00061
Within Groups	16	F	18.04

b) Parrotfish Size

	Protected	Non-Protected	
Mean	27.56	15.99	
Standard Deviation	4.31	7.59	
Degrees of Freedom		ANOVA	
Between Groups	1	P-Value	0.00108
Within Groups	16	F	15.80

c) Diurnal Reef Fish Species Richness

	Protected	Non-Protected	
Mean	48.00	29.78	
Standard Deviation	10.84	9.38	
Degrees of Freedom		ANOVA	
Between Groups	1	P-Value	0.00153
Within Groups	16	F	14.55

d) Large to Small Parrotfish Ratio

	Protected	Non-Protected	
Mean	2.17	0.51	
Standard Deviation	1.69	0.70	
Degrees of Freedom		ANOVA	
Between Groups	1	P-Value	0.02067
Within Groups	16	F	6.59

Table 2
One-way analysis of variance (ANOVA), $\alpha = 0.05$ for:
a) parrotfish abundance
b) parrotfish size
c) diurnal reef fish species richness
d) large to small parrotfish ratio

	Large to Small & Population Size	Large to Small & Species Richness	Average Size & Species Richness	Population of Small & Species Richness	Population of Large & Species Richness	Population of Large & Small
Pearson's r	0.92	0.97	0.80	0.20	0.97	0.42
P-value	0.008	0.001	0.052	0.70	0.001	0.42

Table 3
Pearson's r values and their associated p-values for all examined variables.

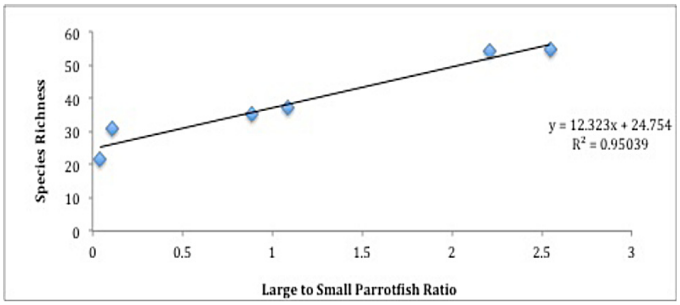

A

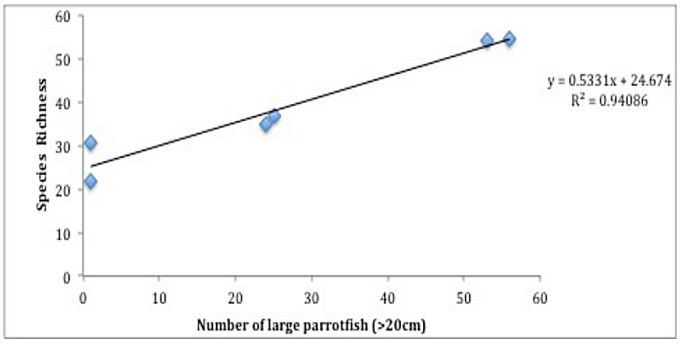

B

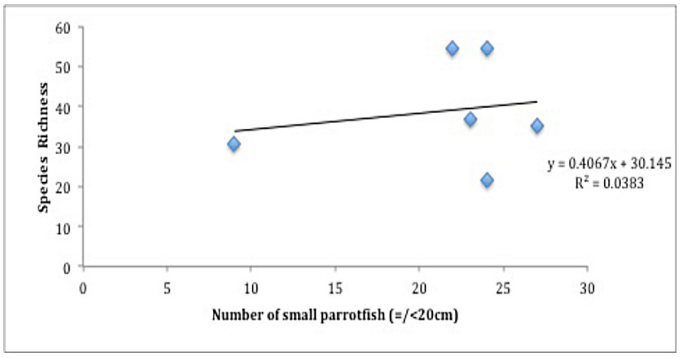

C

Fig. 2
A) Regression of diurnal reef fish species richness vs. number of large parrotfish.
B) Regression of diurnal reef fish species richness vs. number of small parrotfish.
C) Regression of diurnal reef fish species richness vs. ratio of large to small parrotfish.

When examined with Pearson's r, the variables showed strong correlation values. The strongest of which was the relationship between the large to small parrotfish ratio and the diurnal species richness (r=0.97, p=0.001). Large to small ratio was also highly correlated with parrotfish population (r=0.92, p=0.008) and diurnal species richness was correlated with parrotfish average size but was not considered significant with α set to 0.05 (r=0.80, p=0.052). The number of small parrotfish was not correlated to biodiversity (r=0.20, p=0.7) however the number of large parrotfish was (r=0.97, p=0.001). Finally, the Pearson's r for the abundance of small vs. large parrotfish resulted in a moderate correlation of 0.42 (p=0.42) (Table 3).

The large to small parrotfish ratio vs. diurnal reef fish species richness had a strong correlation with an R^2 value of 0.95 (Fig. 2a). Moreover, the coefficient of determination for population of large parrotfish vs. species richness and small parrotfish vs. species richness was 0.94 and 0.04 respectively (Fig. 2b and 2c).

Discussion

The results showed that the distribution of different size classes in communities of parrotfish, particularly the population of large parrotfish, is a more accurate linear measurement for predicting fish species richness on a particular reef than average parrotfish size or number of small-size parrotfish. We concluded that small parrotfish have a relatively small influence on overall fish species richness, while large parrotfish possess a significant one. Average parrotfish size and overall abundance showed notable relationships as well but were not as powerful as the population of large parrotfish. Secondly, the influence of marine reserves on both parrotfish populations and reef fish diversity was found as highly beneficial with more and larger parrotfish found within the reserve as well as greater numbers of diurnal fish diversity.

The positive correlation between *Scaridae* size and the number of fish species present on the reef was again a highlight of the study. However, such a statistical correlation does not provide any information with respect to the direction of that relationship. It could be thought, for example, that since high fish diversity is positively correlated with coral health (10). A reef with high fish diversity (as a result of good coral health) would be an ideal habitat for parrotfish, enabling them to graze *ad libitum* and allowing different species of large parrotfish to thrive. Nevertheless, the analysis highlighted above suggests a direction to the correlation we have established; larger parrotfish graze more on the algae thus increasing polyp recruitment, which is beneficial to the reef diversity, although behavioral studies are needed to further prove this causal relationship.

These results reinforce the paradigm of using MPAs to safeguard and nurture marine ecosystems. Parrotfish alter coral reefs in one of two ways: through eroding corals and feeding on the algae covering these

corals (12). The detrimental impact of parrotfish predation of coral polyps on reefs is a source of mortality for reefs but rarely results in the death of entire coral colonies. This is because their beneficial role as grazers greatly outweighs the negative impacts they impose from predation (12). Extensive algal coverage can have a suite of deleterious effects on coral reefs like the inhibition of juvenile coral growth, potentially leading to their death in addition to decreasing growth and fecundity of adult corals (12). Parrotfish graze on the algae and this function significantly increases beyond a length of 20 cm (3). Such a function is beneficial to coral health and has been shown to increase total density of coral recruitment 2-fold (13). While biodiversity has been established as a pertinent marker of coral reef health (14), it has also been shown that population size of a species such as parrotfish can override the biodiversity as a signal for coral reef health given their functional role in the ecosystem (14). Given these findings and prior knowledge, the province of parrotfish in coral reefs should be considered an essential one and be thoroughly examined when assessing reef fish diversity and inferentially, coral reef health.

There are several limitations associated with our study. The largest assumption is that the other factors of reef habitat quality (besides algal cover) are equivalent among sites. Factors such as reef complexity (15), water quality (16), nutrient input (16), and environmental variables such as temperature, salinity, and pH (17) all play a role in determining reef health and-or biodiversity. While large scale parameters like temperature, pH, and salinity could be considered constant over the small scale of the study (less than 15 km); the local scale variables could not be and were not accounted for in our study, further research should aim to control for this.

The sampling procedure relies on the fact that the species are evenly distributed amongst the reef and that they are equally visible to the observers. Visibility depends upon the water turbidity, time of day and cloud cover in the sky, which we could not control for. Spotting was also influenced by swimming rate, and as a result area covered; this was held fairly constant but could have been influenced by currents or individual fatigue. Misidentification of species would create an inaccurate count but it is assumed that improperly designated species such as juveniles that are aesthetically different from their terminal phase would be misclassified at each sites and the relative population would not be skewed. Due to time and equipment restrictions, we were limited to daytime measurements and 6 sampling sites all of which needed to be accessible by snorkeling from the shore. Due to the limited sample sites the values found to be insignificant have the possibility to be significant given more sampling sites. As such, the results are representative of the diurnal life on reefs located on the west coast of Barbados and not necessarily applicable in other regions containing parrotfish and coral reefs. It is possible that parrotfish exude a large presence on nocturnal biodiversity, which could be a matter for additional analysis. Finally, it is also assumed that the parrotfish are larger in MPAs due to reduced fishing stressors and that the parrotfish put no pressure on the biodiversity (i.e. predation) of the reef other than coral and algae grazing. Given the current literature these are reasonable assumptions.

There exist other indicators of diversity and health of coral reefs such as average parrotfish size and piscivorous fish (4), and other fish species such as the link between butterfly fish and coral reef health (18). That said they are not widespread and those mentioned focus on a specific group of fish and the other is positioned as healthy corals giving rise to healthy fish, not fish giving rise to healthy corals. Our results then provide several unique characteristics. Given the ubiquitous presence of parrotfish on coral reefs worldwide our measure is potentially applicable in many different locations as the mechanics are not unique to Barbados. The assessment is easy to apply in low budget scenarios or with non-scientifically trained personnel. If it can be assumed that reefs with higher fish diversity are indeed healthier this provides a crude tool to simply monitor reef health across time by observing abundance of large parrotfish, again with little time or money required. Lastly it provides yet another indication that marine reserves have positive and measurable effects on marine ecosystems.

Conclusion

The Caribbean is home to some of the most diverse and productive reef systems in the world. An easily measured indicator of fish species richness is an important asset in evaluating the state of coral reefs in Barbados in the face of mounting fishing pressures. We have successfully determined that the ratio of large to small parrotfish is an accurate linear measure of diurnal fish species richness at six sites. Primarily, our results demonstrate that the abundance of large parrotfish (cut-off criteria of > 20 cm) is strongly correlated with species richness but small parrotfish do not. Consequently, this measure can provide a useful tool that can be used to rapidly quantify species richness.

We were only able to sample 6 sites and reef complexity and quality was not assessed which may limit the results of the study. We speculate that the main variations in parrotfish size arose from differences in fishing pressures. In order to test that our indicator can be used in a variety of environments, future research should aim to sample different coral reefs throughout the Caribbean. Coral reefs in different locations are likely to be exposed to a multitude of environmental stressors such as nutrient input from groundwater, pollution and deviations in ocean currents and experimenting at varied sites would enable the testing of the validity of our indicator. Overall, our results provide a novel concept that builds upon previous studies though it still demonstrates a tangible result, which, ideally, could be extended spatially, and serve to preserve the unique yet endangered ecosystems that are coral reefs.

Acknowledgements

We would like to thank the McGill Bellairs Research Institute in St. James, Barbados for its accommodation and providing us with the facilities where the research was conducted. An extra big thanks to the kitchen staff who served us so many wonderful meals over our stay.

Additionally, we thank Dr. Henry Valles from the department of biological and chemical sciences of the University of West Indies at Cave Hill, Barbados for discussing his work with us, which led to the establishment of our project.

Finally, we wish to extend a special thank-you to the professors Frederic Guichard, Thomas Bureau and Neil Price of the department of biology of McGill University for their knowledge, guidance and help in the production of this paper.

References

[1] Mohammed E, Parker C, Willoughby S. Barbados: Reconstructed fisheries catches and fishing effort, 1940-2000. Fisheries Centre Research Reports. 2003; 11(6):45

[2] Streelman JT, Alfaro M, Westneat MW, Bellwood DR, Karl SA. Evolutionary history of the parrotfishes: Biogeography, ecomorphology, and comparative diversity. Evolution. 2002; 56(5):961-971.

[3] Lokrantz J, Nyström M, Thyresson M, Johansson C. The non-linear relationship between body size and function in parrotfishes. Coral Reefs. 2008; 27(4):967-974.

[4] Vallès H, Oxenford HA. Parrotfish Size: A Simple yet Useful Alternative Indicator of Fishing Effects on Caribbean Reefs? PloS one. 2014;9(1):e86291.

[5] Wilkinson C. Status of coral reefs of the world: Global Coral reef Monitoring Network and australian Institute of Marine Science. Townsville, Queensland, Australia. 2004;301.

[6] Hilty J, Merenlender, A. Faunal indicator taxa selection for monitoring ecosystem health. Biological Conservation. 2000; 92(2):185-197.

[7] Appeldoorn RS, Lindeman KC. A Caribbean-wide survey of marine reserves: spatial coverage and attributes of effectiveness. Gulf and Caribbean Research. 2003;14(2):139-54.

[8] McClanahan TR, Marnane MJ, Cinner JE, Kiene WE. A comparison of marine protected areas and alternative approaches to coral-reef management. Current Biology. 2006; 16(14):1408-1413.

[9] Walther D, Edgington DR, Koch C., editors. Detection and tracking of objects in underwater video. Computer Vision and Pattern Recognition. CVPR 2004 Proceedings of the 2004 IEEE Computer Society Conference on; 2004: IEEE.

[10] Jones GP, McCormick MI, Srinivasan M, Eagle JV. Coral decline threatens fish biodiversity in marine reserves. PNAS. 2004; 101(21):8251-8253.

[11] Hodgson G. A global assessment of human effects on coral reefs. Marine Pollution Bulletin. 1999;38(5):345-55.

[12] Mumby PJ. Herbivory versus corallivory: Are parrotfish good or bad for Caribbean coral reefs? Coral Reefs. 2009; 28(3):683-690.

[13] Mumby PJ, Dahlgren CP, Harborne AR, Kappel CV, Micheli F, Brumbaugh DR, Gill AB. Fishing, trophic cascades, and the process of grazing on coral reefs. Science. 2006; 311(5757):98-101.

[14] Bellwood DR, Hoey AS, Choat JH. Limited functional redundancy in high diversity systems: Resilience and ecosystem function on coral reefs. Ecology Letters. 2003; 6(4):281-285.

[15] Ménard A, Turgeon K, Roche DG, Binning SA, Kramer DL. Shelters and their use by fishes on fringing coral reefs. PloS one. 2012;7(6):e38450.

[16] De'ath G, Fabricius K. Water quality as a regional driver of coral biodiversity and macroalgae on the Great Barrier Reef. Ecological Applications. 2010;20(3):840-50.

[17] Done TJ. Coral community adaptability to environmental change at the scales of regions, reefs and reef zones. American Zoologist. 1999;39(1):66-79.

[18] Hourigan TF, Timothy CT, Reese ES. Coral reef fishes as indicators of environmental stress in coral reefs. Marine organisms as indicators: Springer; 1988;107-35.

RESEARCH ARTICLE

Development and Characterization of a Directional Gamma-ray Detector

Felix Cormier[1], Marcel Georgin[1]*, Stephen Koelbl[2], Robert Oda[3]

[1] Department of Physics, McGill University, Montreal, QC, Canada
[2] Department of Physics and Department of Physiology, McGill University, Montreal, QC, Canada
[3] Department of Physics and School of Computer Science, McGill University, Montreal, QC, Canada

*Email Correspondence:
marcel.georgin@mail.mcgill.ca

Keywords
High Energy Physics
Gamma Ray Detection
Directional Detector
Applied Physics
Silicon Photomultipliers

Abstract

Background: This work characterizes the first generation of detectors from the Hanna Laboratory to implement Silicon Photomultipliers and a heptagonal scintillator conguration. The purpose of the device is to determine the angle at which a radioactive source is located.

Methods: The development of the detector consisted of three phases: construction(September 2012-December 2012), simulation and characterization (April 2013). The experimental portion of the work consisted of placing a $^{137}_{55}$Cs source at an arbitrary location, measuring the count rates in each scintillator panel and analysing the results.

Results: The detector's function was validated by confirming the inverse square law with a radioactive source moving away from the detector. Furthermore, with a x^2 summation method of analysis the angular position of a source was determined with an accuracy of 10˚ and a precision of 12˚. With a normalisation method of analysis the angular position of a source was found with an accuracy of 2˚ and a corresponding precision of 2˚.

Limitations: The quality of the electronics handling the signal from the silicon photomultipliers limited our resolution. Occasional double counts occur when a large amount of energy is imparted to the scintillator. Furthermore, the custom-built circuitry lowered the signal-to-noise ratio such that large distances were not feasible due to electronic noise constraints. Finally, simulation data analysis showed that the break of one circuit only had a small effect on the x^2 method of analysis.

Conclusions: In conclusion, the design of the detector and the analysis techniques were shown to be suitable for short range angular resolution of a gamma-ray source. Both distance trials and a simulation of the detector prototype confirmed the validity of our design and of the analysis methods used. These promising results at short distances motivate further work in electronic circuit design to improve the range while maintaining both accuracy and precision.

Introduction

Motivation

The inspiration for the development of a scintillating directional gamma-ray detector is the BATSE (Burst And Transient Source Experiment), an experiment on the National Aeronautics and Space Administration's (NASA) Compton Gamma Ray Observatory Satellite looking for gamma-ray bursts (1). A scintillating detector is made of material that will release photons when struck with radiation - these photons can then be picked up by specific electronics. The BATSE experiment used eight scintillating modules to determine the direction of a gamma ray source in space. These modules were made of two scintillating components. Thallium doped Sodium Iodide was the first scintillating material used and it allowed the observatory to detect gamma-rays within an energy range of 20 keV to 2 MeV. The second component was made of pure Sodium Iodide, which extended the modules energy range to approximately 8 MeV allowing the experiment to detect more powerful sources. This device was ultimately used to detect cosmic gamma-ray sources by relying on the

fact that scintillators which had a greater effective area (thus facing the source) would have a greater count rate (1).

Luc Sagnière from the Hanna Laboratory developed an octagonal (eight sided) Gamma-ray Detector (OGD) using this proven platform. The purpose of this device was to quickly detect the angular position of a terrestrial gamma-ray source rather than detection of gamma ray sources in space. This was accomplished by orienting eight scintillating plates in an octagon and using photo-multipliers to collect and convert the light into a current, which could be converted to a count rate. The count rate in each of the eight channels is then analysed to determine the angular position of the radiation source (2).

The current iteration of the directional gamma-ray detector prototype takes advantage of developments in both the geometry and the technology; rather than using an octagonal design and photo-multipliers of the OGD, a heptagonal (seven sided) geometry and silicon photo-multipliers were chosen to create the new Heptagonal Gamma-ray Detector (HGD).

Design

Previously, the OGD difficulties determining the origin of a radiation source because of the symmetry in the octagonal shape. Due to the bilateral symmetry in the previous design, both the nearest and farthest faces would have high count rates, creating an ambiguity in the results. This is shown in the right hand side of Fig. 1.

To solve this problem, the design of the detector takes advantage of the change in the solid angle of each face with which the gamma radiation can interact. The closest face normal to the incident radiation will have the greatest cross sectional area and therefore the most interaction with the gamma rays. The faces which are at steeper angles will have a signicantly reduced effective area of interaction. This reduction in solid angle is shown clearly in Fig. 1(a). The cross sectional area in (1) from Fig. 1(a) is much greater than that of (2).

During experimental setup and calibration, the circuit connected to one of the scintillators was damaged. Several attempts to repair were made however it was not possible to complete these repairs within the allocated time frame of the project. The project was completed with the remaining six faces.

Polyvinyl Toluene

Scintillators are materials that convert short-wavelength photons, such as gamma-rays, into longer wavelength photons. This is accomplished via a process called Compton scattering where a gamma ray inelastically collides with an atomic electron and deposits energy. This excited electron then re-emits a longer wavelength photon through either fluorescence or phosphorescence. These emitted photons are contained in the scintillator until detected by an attached photomultiplier. Polyvinyltoluene (PVT) is an organic plastic scintillator which emits light at a wavelength of 423 nm (3). PVT was selected as the scintillating material because of its rapid decay time of 2.4ns. Furthermore, it is transparent to its own emissions - this is very important as opacity would result in signal loss. Beyond its physical properties, an additional reason for the selector of PVT was the low cost of the material (4).

Silicon Photomultiplier & Circuit

Silicon Photomultipliers (SiPMs) are the semiconductor analog to the traditional photomultiplier tube. Silicon photo-multipliers are built from an array of avalanche photodiodes on a common silicon substrate. An avalanche photodiode (APD) is a device which takes advantage of the photoelectric effect to generate a current from the impact of a photon at the p-n junction. A bias voltage generates an electric field at the interface between the n and p type silicon semiconductor. The field is so large ($\approx 5 \times 10^3$ V/cm) that a single photon interaction with the pixel can produce a large enough cascade of electrons to generate a detectable current (5).

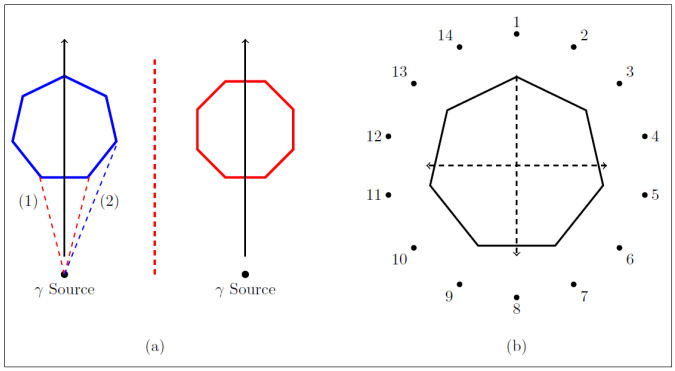

Fig. 1
(a) Basic geometry of the detector. The theory is that the change in the solid angle between (1) and (2) will cause a change in the count rate. Degenerate results were due to scintillators being parallel in the octagonal geometry of the detector (red). This was avoided by using the seven sided geometry on the left.
(b) Plan of the detector with 14 calibration points labeled around the panels. This diagram is the basis for the entire calculation of the angle. All angles will be referred to from angle 1 set as θ = 0.

For the development of the HGD, the ArraySM-4 silicon photomultiplier from SensL was implemented as the converter of optical photons into a current. This SiPM's peak absorption wavelength is at 500nm and it has an internal gain of 2.3 x 10^6 per pixel; the scintillator material, polyvinyl toluene, outputs green photons to match the 500nm absorption wavelength. In total, the ArraySM-4 has sixteen pixels each with their own output. A silicon photomultiplier was chosen over a photomultiplier tube for several reasons: it is more compact and has lower bias voltage requirements. The readout electronics used in the gamma ray detector were custom-built to operate with the SiPM as part of this project (6). This SiPM was biased by a custom designed circuit. Additionally, this same circuit was used to amplify the signal from the SiPM and transfer it to the data acquisition system described in Section 3.2.

Methods

Experimental Setup

Each PVT face is made of a 25 cm tall by 7.5 cm wide by 2 cm thick piece of PVT plastic scintillator. Each scintillator was wrapped in Tyvek to improve the internal reflectivity and then wrapped again with electrical tape to isolate the face from the ambient light. At the top of the each face, a hole was cut out in the protective wrapping to place the SiPM in contact with the PVT. The SiPM is then interfaced with its own amplifying circuit, described in Section 2.4, and then rewrapped to ensure that the system was light tight. The circuit then sends the signal to the data acquisition system. This was repeated for each individual scintillator, meaning there were seven scintillators, SiPMs and amplifying circuits.

Data Acquisition System

The data acquisition process was identical for each of the six active faces of the HGD. First the signal from the amplifying circuit was passed into a discriminator whose threshold is determined by the calibration in Section 3.4. This discriminator outputs a NIM pulse (-0.7 V) for every input pulse at greater voltage amplitude than the threshold. This signal was then passed to a scaler which counts the number of NIM pulses for each circuit. The duration of each trial and the number of trials is determined by the user through programming of a CAMAC module using C++. The CAMAC data acquisition system serves as the conversion program between NIM pulses and digital output to be analysed.

Simulation

In parallel to the construction of the detector, a simulation was created to virtually run experiments using the Geant4 system. This system was developed to simulate high energy particle physics experimentation. Written in C++, the simulation utilized Monte Carlo methods to test the detector's geometry and detection by allowing users to construct a virtual model of an experiment and programming the behavior of various types of radioactive sources (7).

One of the circuits was damaged during testing. This simulation proved to be vital to the experiment as it modelled a full working set of panels; this allowed for full calibration of the virtual system and a full set of data to compare results with the physical detector.

Calibration

The first step in calibrating the detector is setting the gain of the individual photomultiplier circuits as well as the threshold of the discriminator connected to the circuit's output. The gain is the amplitude of the voltage response to a gamma ray. This was first determined by minimizing the signal to noise ratio. Then, a threshold curve was made to calibrate the discriminator threshold for each circuit.

Gain

The gain set for each individual circuit was chosen such that two different parameters were satisfied. First, the voltage response for each scintillator to a gamma ray had to be equal for each circuit, within uncertainty. Second, the electronic noise in the output had to be less than 10% of the gamma ray voltage. Since the gain was determined by a potentiometer, there was no absolute gain measurement, however, the circuits could be compared to equalize their relative gains.

The instrument used for measurement was an oscilloscope. By viewing the circuit output with and without a radioactive source, the gamma ray voltage output and the electronic noise could be compared. This could be done using the oscilloscope digital tools which measured maximum and mean voltage.

To begin the calibration, the gain of the circuit with the lowest signal-to-noise ratio was set to have its noise be about 10% of its gamma ray voltage. Quantitatively, for a ^{137} Cs source, this equates to a voltage response of 0.68(3) V for a gamma ray, and 0.07(3) V for the electronic noise. Then, the gain of the other circuits was adjusted such that a gamma ray from a ^{137}Cs source would output a voltage of 0.68 V, within one standard deviation.

Threshold

With the gain set, a threshold curve was constructed for every circuit. This was done by incrementally decreasing the discriminator threshold and measuring the count rate. For every channel, the count rate stayed about constant until a certain threshold value was reached, then the count rate started exponentially increasing. The threshold value about 50mV before this exponential increase was chosen for every channel, so as to stay below the noise. Threshold for every channel was very similar, with values around the 200 mV range.

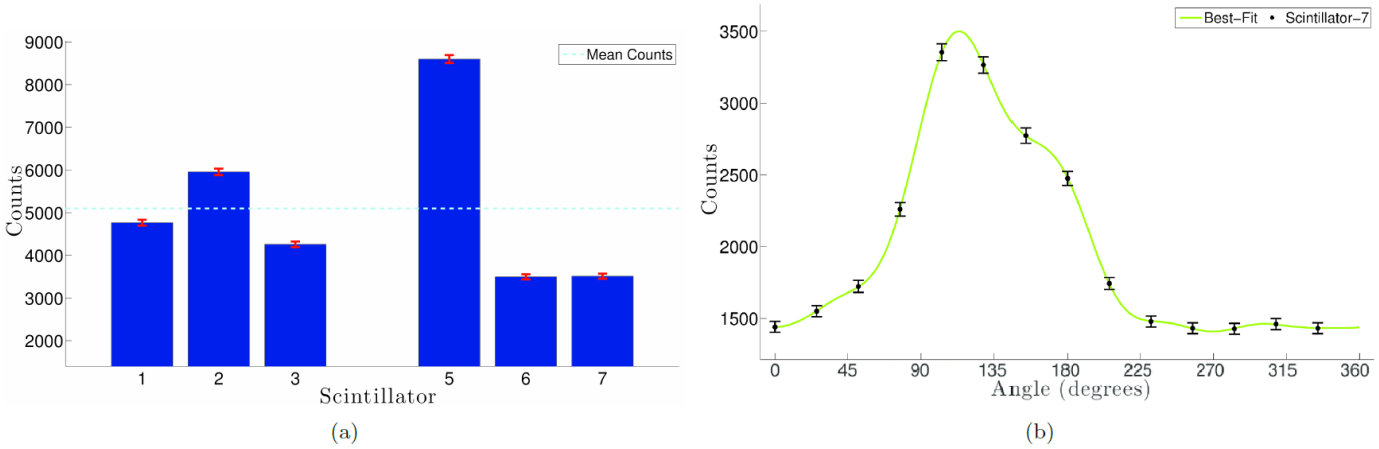

Fig. 2
(a) Calibration data for the normalization analysis method. **(b)** Calibration data for the 2 summation analysis method. This figure shows the number of counts for scintillator 7; every data point is one of the calibration angles. It is fit with a 6-term Fourier series with a period of 360.

Angle Calibration
The final step in calibrating the detector is placing the ^{137}Cs source at all the points shown on Fig. 1(b). For every point, count rates are measured for every scintillator. This gives a baseline set of data to compare to when a radioactive source is placed at a random angle. All angles will be referred to from angle 1 from Fig. 1(b) as θ = 0 rad.

This calibration procedure will output a graph such as Fig. 2b for every scintillator. By comparing results for calibration points and random points for every scintillator, a x^2 method of analysis can be used to reconstruct the random angle. Similarly, using Fig. 2a, counts can be normalized for every scintillator, and used as part of the normalization analysis method.

Distance Sensitivity

The distance sensitivity was tested by placing a radioactive source directly in front of one of the scintillators and displacing the source away from this scintillator perpendicularly to its surface. This test is designed to verify the well known $\frac{1}{r^2}$ relationship between the position of the source with respect to the detector and the intensity of the radiation at the detector. This test was completed by placing the source in front of scintillator 1 and moving it radially outward in intervals of 8.0(2) cm to a maximum of 64.0(2) cm. It will also determine the effective range of the detector; information which can be used to setup further testing as in Section 3.6.

Angular Resolution

A subsequent experiment was conducted. To do this, three random angles were chosen (63°(2), 117°(2) and 299°(2)). Using the results from the distance sensitivity trial, a distance where the scintillators counts are well above the noise was chosen. Two methods to resolve the position of the radioactive source were developed: the x^2 method and the normalisation method. Both methods were used to determine the location of a randomly positioned source. Two of the angles were also analysed in the simulation to provide a quantitative comparison.

Results

Validation of the Inverse Square Law

By changing the distance of the source with respect to one of the scintillators, the sensitivity of the detector to changes in source position can be determined. Fig. 3 shows the result of the distance test which used a x^2 minimization method to fit the data acquired. The equation obtained for scintillator 1 is shown in Equation (1).

$$y = \frac{9.1 \times 10^5}{(x + 5.1)^2} + 9.4 \times 10^2 \quad (1)$$

In this case, the inverse square law can be confirmed if it can be shown that the fit is of statistical significance. To do this, the p-value of this fit is computed, giving a value of 0.999 from which it can be concluded that the data fits an inverse square law. Finally, a distance between 10 and 15 cm was used for the random source test as these are well above the noise pedestal encountered at around 60 cm.

Angular Resolution

x^2 Method of Source Location
The first step in the x^2 method is obtaining the calibration data from the 14 points on Fig. 1(b) and fitting the data using a six-term Fourier series, as seen in Fig. 2b. This is done for each scintillator. The use of

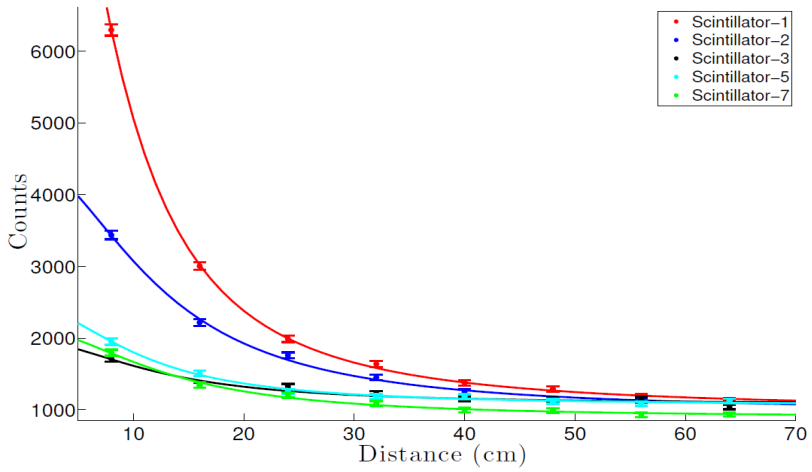

Fig. 3
The number of counts for each of the 7 scintillators as the source is moved outwardly away from the detector. The source was placed at position 1 (Fig. 1(b)). As can be seen, the best-fits follow the $\frac{1}{r^2}$ relation, as expected.

a six term Fourier series was motivated by the work done by Luc Sagniere (2), who uses a six-term Fourier series, as well as the requirement that the fit be periodic over 360°. Then the Fourier series for each scintillator is compared to the data obtained at the random point using Equation (2).

$$\chi^2 = \frac{(y_i - y_i(\theta))^2}{\alpha_i^2} \quad (2)$$

In Equation (2) y_i is the number of counts registered by scintillator *i* when the radioactive source is placed at a random point, and is thus a constant for each scintillator. $y_i(\theta)$ is the number of counts predicted by the Fourier series fit for scintillator *i* as a function of angle done during calibration as explained in the previous paragraph, and α_i is the error in the counts registered by scintillator *i*. The x^2 function for each scintillator is calculated, then all these functions are added together to give the plots seen in Fig. 5. Note that the x^2 is a function of θ. The value of θ for which the total x^2 is smallest is the location of the source determined by the HGD.

To obtain the uncertainty in the x^2 analysis, error was propagated through by changing y in Equation (2) by ±α, then recomputing x^2, giving x^2_{upper} and x^2_{lower} respectively. The error in the measurement was found by locating the angles, θ_{upper} and θ_{lower} which correspond to minima in x^2_{upper} and x^2_{lower}. Computing $\alpha_{upper} = \theta_{upper} - \theta$ and $\alpha_{lower} = \theta - \theta_{lower}$ gives the error in the measurement. This type of non-traditional error analysis is important as this detector has been designed for on-the-fly angular measurements - this method thus allows for *in situ* angle and precision measurements.

Fig. 5 is the result of the x^2 analysis for both the simulated and experimental data. A qualitative comparison between the simulated and experimental data shows that the performance of the HGD is similar to what was expected from the simulation. Results for both simulation and experimental data for the random points are shown in Table 1. Quantitative differences between experimental and simulation data will be discussed in Section 5.4. For random position 1, the radioactive source was placed at 63°(2) with respect to angle 1 in Fig. 1(b). The experimental results from the x^2 analysis method resolved the angular position of the source to be 72°(1). Equivalent analysis of the simulated data computed the angular position of the source to be 61.9°(4). Results for other positions are summarised in the above-mentioned table.

	Position Angle			
	Method	Random Point 1 (deg)	Random Point 2 (deg)	Random Point 3 (deg)
Real	x^2 Summation	72 (1)	291.4 (4)	105 (1)
	Normalization	65 (2)	290 (2)	122 (2)
Simulation	x^2 Summation	61.9 (4)	300.6 (4)	NA
	Normalization	64 (2)	293 (2)	NA
True Value		63 (2)	299 (2)	117 (2)

Table 1
A summary of the calculated position angle of the random points. The method of finding the errors of these are discussed in detail in Section 4 and Section 5.

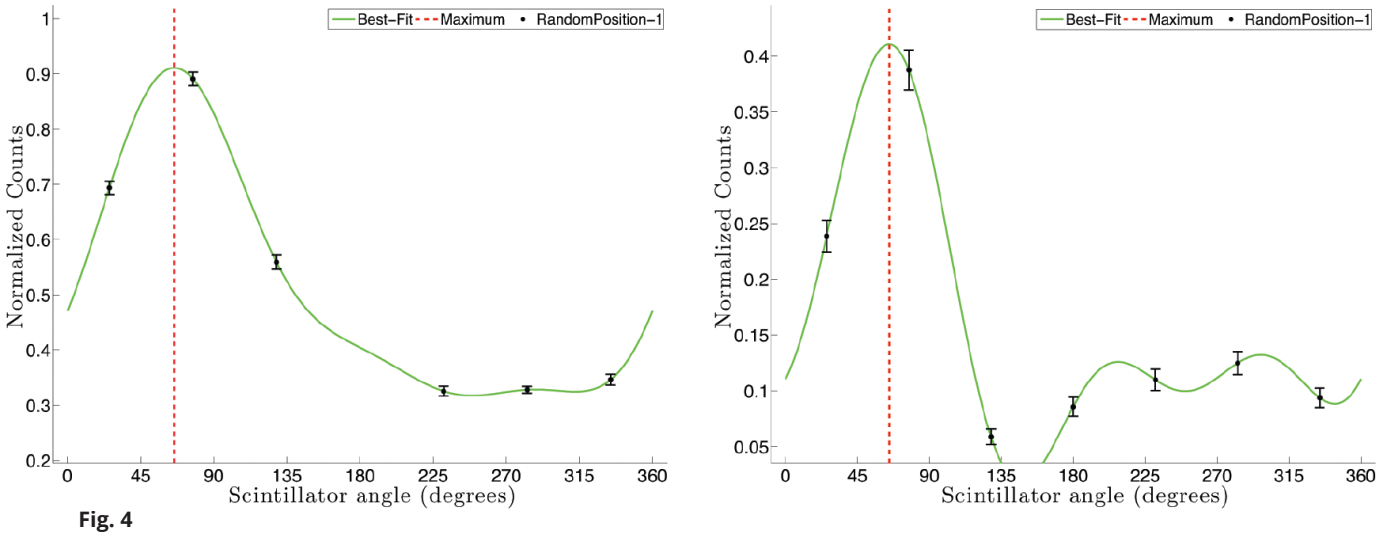

Fig. 4

After calibration, the normalised number of counts for random position 1 is shown for the real (left sub-figure) and simulated (right) data. A best-fit curve was found using a Fourier-6 (solid green line) is shown. The global maximum of the curve corresponds to the angle position of the source at random position 1.

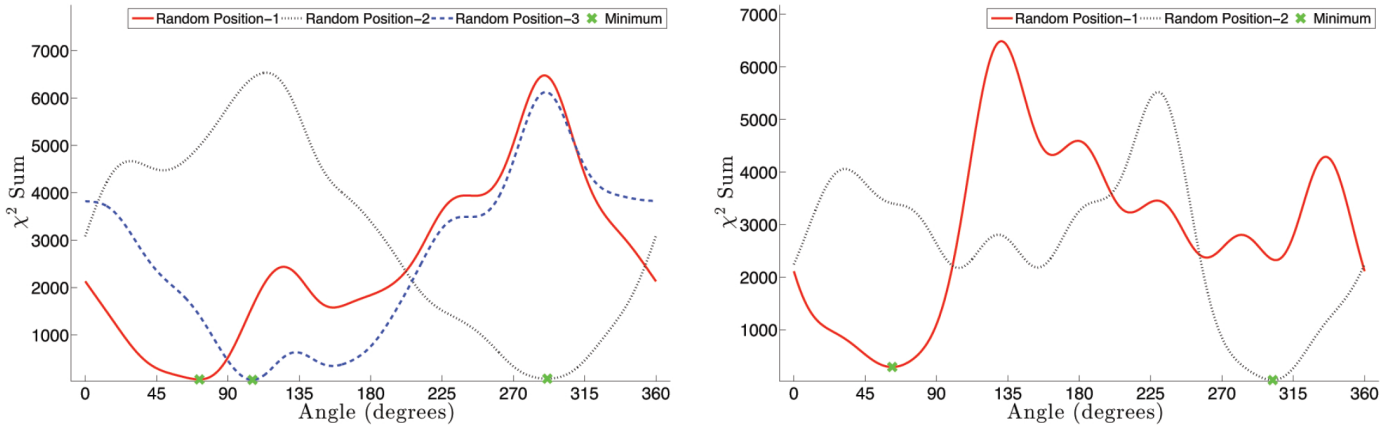

Fig. 5

For the experimental (left sub-figure) and simulated (right) data, the x^2 summation for each of the random points are shown. The minimum for each x^2 summation (green x) corresponds to the respective angle position of each random point. The determined angle position for the real and simulated data are comparable.

Normalisation Method of Source Location

The normalisation method uses the calibration points, seen in Fig. 2a, as normalisation factors for the data retrieved from the random position tests. The normalised counts in each scintillator are then fit with a six term Fourier series. The scintillator angle of the fit's maximum is the location of the source. Fig. 4 shows a comparison between the results of the simulation and the HGD. This qualitative comparison shows that the signal quality of the detector is what was expected from the Geant4 simulation.

For the normalization method, the error on the fitting parameters was negligible. Thus, the error on the normalization counts, as shown in Fig. 2a, was used. Since this was a counting experiment, the square root of the counts was used as the error, propagated through the normalization analysis method, and output as a 2° uncertainty. This again allows for an in-situ analysis of the angle, as in the x^2 analysis method.

Results for both experimental and simulated data are shown in

Table 1. For random angle 1, where the radioactive source was placed at 63°(2), the experimental results from the normalisation analysis method calculated the angular position of the source to be 65°(2). In parallel, analysis of the simulated data computed the angular position of the source to be 65°(2). The rest of the results are summarised in the above-mentioned table.

Discussion

The primary objective of this research was to demonstrate a proof of concept for a heptagonal gamma-ray detector design. To achieve this goal, a simulation as well as a two part experiment was conducted. The goal of the simulation was to first validate the design of the detector and subsequently act as reference for comparison to future experiments. Because one of the detector faces was damaged, the simulation allowed us to see the effect of the loss of a circuit. Table 1 shows that the x^2 summation analysis method was consistently less accurate *in situ* than in the simulation while the normalisation method was not affected as much by the loss of a face. The first experiment tested the radial sensitivity of the detector. Beyond testing the ability of the HGD to resolve sources at a distance, this test was designed to observe the $\frac{1}{r^2}$ law as a verication of the detector's circuitry. The second experiment tested the ability of the HGD to resolve the angular position of a source. In conjunction, these tests were able to show that the HGD was a successful initial prototype. Table 1 summarizes all the results obtained from both the x^2 and normalisation methods.

Analysing the Relationship Between Distance and Counts

By varying the of distance between a radiation source and the detector, we were able to draw several conclusions about the performance of the detector. The inverse square law for distance served as a verification of the circuit design and data acquisition methods.

Finally, the distance sensitivity shows that at around the maximum distance studied, 64 cm, the derivative approaches 0 as the data obtained becomes dominated by the noise. This leads to the conclusion that the maximum distance for which the detector could resolve the position of a radioactive source that had the same output as the radioactive sample used, is 64 cm. This restriction is due to the gain of the individual scintillator's circuits. Each circuit had a threshold as well as background noise which created counts not from the radioactive source studied this could be natural radiation like cosmic rays or natural sources in the surroundings. Efforts were made to increase the signal-to-noise ratio which led to the results shown in Section 5.1. With a refinement in the electronics used to shape the signal from each scintillator, it is very likely that a future iteration of this project could succeed at distances much larger than those seen here.

Qualitative Analysis

A qualitative comparison of the experimental and simulated results can now be made. In Fig. 4 (experimental on the left, simulated on the right), we see that the shape of the data and best fit curves are similar. The simulated data represents the number of times energy was deposited in a scintillator face. Therefore, the correlation between the shapes in Fig. 4 suggests that the SiPM in the electronics is correctly collecting the light from the scintillator in proportion to the number of incident gamma-rays.

Analysis methods

The two analysis methods used, x^2 and normalisation, were both successful at determining the angle of the radioactive source with respect to the detector. In terms of the results shown in their respective sections, the x^2 method analysed the position to be 8 times the uncertainty in the measurement from the actual position for the experimental results and 3 times the uncertainty in the measurement for the simulation. For the normalisation method, the experimental and simulated results were both only 1 times the uncertainty in the measurement from the actual value. For every position attempted, the results determined from normalisation analysis were more accurate and precise than those determined through the x^2 method of analysis.

Thus using the normalisation method of analysis gives an excellent approximation of the angle of the source with respect to the detector, and shows the success of the heptagonal detector at low distances.

Error Sources and Improvements

Several factors during the construction and testing of the device negatively affected the performance of the HGD.

The use of SIPM's reduced the size and weight of the device compared to previous models, however, during long tests, the gain within the device was found to vary signicantly with time and possibly also with temperature. This lead to difficulty in calibration and ultimately device performance.

During the construction of the HGD, there was a design change in the amplifying circuit in which the old circuit boards were modied for a new, simplied design. Using this make-shift circuitry likely induced a signicant amount of noise in the signal received from the SIPMs. The circuit used in testing also caused ringing in the pulse which occasionally resulted in double counts in the scaler. Using a new circuit board would likely significantly improve the signal to noise ratio and ultimately the performance.

The loss of the amplifying circuit from the seventh face of the detec-

tor during testing likely affected performance, however this cannot be known as the circuit could not be fixed. The results of the tests show that the detector was still able to perform despite the missing face which suggests robustness to failure in the design of the HGD.

The HGD's ability to detect a source at a distance was worse than expected. This was mostly due to the signal to noise ratio. With a 0.1 μC ^{137}Cs source, the signal from the HGD was reduced to noise levels after the source was moved 64 cm away from the detector.

Considering these aforementioned problems in the development of the HGD, the detector still qualitatively performed as predicted by the Geant4 simulation. The detector was capable of determining the location of a source accurately. Even though the distance away from the detector was small, this is still a successful proof of concept and with some modications could provide the performance required to detect more distance sources.

Conclusion

In conclusion, the design of the detector and the analysis techniques were shown to be suitable for short range angular resolution of a gamma-ray source. Both distance trials and a simulation of the detector prototype conrmed the validity of our design and of the analysis methods used. Using normalisation analysis at small distances, the detector was accurate within 2° of its true angular position. The uncertainty of the position calculation was 2°. These promising results at short distances motivate further work in electronic circuit design to improve the range while maintaining both accuracy and precision to within the values outlined in this report.

Acknowledgements

We would like to thank Professor David Hanna for allowing us to use his laboratory and his equipment for the construction and testing of the detector, Audrey MacLeod for her help with understanding the physics behind the detector, Adam Gilbert for assistance with the circuit design and testing, and Sean Griffin for help with programming the control code for the CAMAC module.

References

[1] Meegan, C , Fishman, G , Wilson, R , Brock, M , Horack, J, Paciesas, W , Kouveliotou, C . The spatial distribution of gamma-ray bursts observed by BATSE. In: AIP Conference Proceedings. vol. 265;. p. 61.

[2] Sangiere L. A Gamma-Ray Directional Detector; 2012.

[3] Birks JB. Energy transfer in organic systems VI. Fluorescence response functions and scintillation pulse shapes. Journal of Physics B: Atomic and Molecular Physics. 1968;1(5):946. Available from: http://stacks.iop.org/0022-3700/1/i=5/a=323.

[4] Rakes KD. Evaluating The Response Of Polyvinyl Toluen Scintillators Used In Portal Detectors. Air Force Institue of Technology Wright-PAtterson; 2008.

[5] Buzhan. An Advanced Study of Silicon Photomultiplier; 2003.

[6] Silicon Photomultipliers by SensL; 2013.

[7] Agostinelli S, Allison J, Amako K, Apostolakis J, Araujo H, Arce P, et al. Geant4a simulation toolkit. Nuclear Instruments and Methods in Physics Research Section A: Accelerators, Spectrometers, Detectors and Associated Equipment. 2003;506(3):250 { 303. Available from: http://www.sciencedirect.com/science/article/pii/S0168900203013688.

RESEARCH ARTICLE

Microstimulation to the Middle Temporal Area and its Effect on the Generation of Microsaccades

Haider Riaz[1]*, Ashkan Golzar[2]

[1] Department of Physics, McGill University, Montreal, QC, Canada
[2] Department of Physiology, McGill University, Montreal, QC, Canada

*Email Correspondence:
haider.riaz@mail.mcgill.ca

Abstract

It has been repeatedly shown that neural activity in different brain structures can be correlated with perceptual and cognitive functions using electrical microstimulation. Currently, microstimulation is the only method that can demonstrate causal links between neural activity and specific cognitive functions. This study investigates the effects of microstimulation to the MT area of the visual cortex on the production of microsaccades for several seconds. Microsaccades are a type of fixational eye movement characterized by their quickness and low amplitude. The preliminary findings in this paper suggest that microstimulation to the MT area causes an increase in frequency and peak velocity of microsaccades. However, a more in-depth analysis to establish a correlation between the two was unsuccessful. These results suggest further investigation into the effects of microstimulation on microsaccades – using more sophisticated and reliable data collecting and analyzing techniques – is necessary.

Introduction

Microsaccades are involuntary miniature eye movements that occur during extended visual fixation in animals with *foveal vision*. The amplitude of microsaccades varies from 2 to 120 arcminutes (1, 2). The exact physiological role of microsaccades in vision is still a debated topic. Studies have proposed microsaccades to be the mechanism that counteracts drifting of the eyes (3) and visual fading (4). Furthermore, microsaccades have been associated with an increased visual detection threshold (5, 6). This study explores the effect of microstimulation in the middle temporal (MT) area of the visual cortex on the frequency and peak velocity of microsaccades.

Microstimulation is an effective way to manipulate the activity of a small group of neurons with spatial and temporal precision since neurons communicate electrochemically and the electric current induced by the microstimulation can excite or suppress this activity. It is a powerful tool that allows us to observe the behavioral effects of an increase in the output signal of a group of classified neurons. Therefore, microstimulations are widely used to link neural activity with a particular cognitive function (3).

In this study, microstimulations are applied to the MT area of the visual cortex . This region has been shown to be highly selective for coherent motion and is also linked to the computation of three-dimensional structures (4, 5, 6). It was assumed that microstimulations produce percepts that are similar to the ones generated by natural sensory stimuli, however, Masse and Cook (4) showed that microstimulations in the MT area produced weaker but longer-lasting effects on motion perception in comparison to natural visual stimuli.

The effect of microstimulation on microsaccades has not been previously explored in any great detail. Low-amplitude and brief events such as microsaccades are difficult to detect and characterize. We will use microstimulation to explore the neural systems that control visual fixation and microsaccades. Furthermore, we hope to establish a link between the firing properties of the aforementioned neurons and the production of microsaccades.

Experimental Procedure

Two male monkeys (*Macaca mulatta*) were trained to detect a small pulse of coherent motion in a random dot patch. Eye position data was collected from the monkeys using a video based eye tracking system. For this specific study, we used two non-overlapping random dot patches (RDP). The RDPs would display coherent motion for discrete time periods (minimum 19 ms) at random moments during the experimental trial. The level of coherence of the two RDPs was different. The patch with high coherence had 95% coherence in all of

its coherent motion pulses. In other words, 95% of the dots would move in the same direction for the duration of the coherent motion stimulus. The patch with low coherence had 20 to 80% (mean of 30%) coherence in all of its coherent motion pulses. Furthermore, since neurons in area MT are directionally selective, the coherent motion pulse of a RDP was matched to the preferred direction of the overlapping receptive field. Electrical microstimulation was delivered to the receptive fields (one for each RDP) with two low impedance (250-1000 KΩ at 1KHz) microelectrodes using a constant–current dual phase simulator (Bak Electronics). The microstimulation waveform is synchronized with the motion stimulus waveform of the RDP that has low coherence but with a lag of 50 ms. An individual microstimulation pulse had a width of 200 μs and the pulses would be fired at a frequency of 250 Hz. The current levels used ranged from 3 to 50 μA with a median of 12 μA.

The trial would start when the monkey depressed a lever to signal that it had started fixating on a specified point on a screen. The trial would end if the monkey's eye position deviated more than 1.5 degrees from the fixation point. After the lever was depressed, motion started in two random dot patches close to the fixation point. A pictorial representation of this setup can be viewed in Figure 1. The monkey indicated, by releasing a lever, when motion in either of the two patches became correlated, that is to say the instance that the dots had the same pattern of back and forth motion. The coherent motion pulses would occur at random during the trial in either of the RDPs according to an exponential distribution, the flat hazard function. The time limit to indicate correlation begins at the onset of motion (correlated) and lasts until 200 ms after the end of the coherent motion pulse. Eye positions were recorded every 2 ms. (500 Hz) using the eye tracking system.

The trial would end if the lever was released, if the monkey broke fixation, or if the time limit of 200 ms since the end of the last coherent motion pulse for the trial had elapsed. For this study, only the trials where the monkey was able to indicate within the allowed time period that correlation was occurring were used. Failed trials, such as those when the monkey's response was too slow or the lever was not released, and false alarm trials, when the monkey raised the lever despite the fact that there was no correlate motion in the patches, were disregarded.

The animal's head was stabilized using steel head-posts before the beginning of trials. The monkeys were also implanted with recording chambers (Crist Instrument) and craniotomies were performed so that the microelectrodes can be inserted into area MT of the visual cortex (these procedures need only be performed once). Structural MRI scans (1.5 T) were used to verify chamber location and microelectrode placement in area MT. All animal procedures followed guidelines set forth by McGill University's Animal health Care Committee and Canadian Council on Animal Care.

Data Analysis

Microsaccades are ballistic movements and leave behind small linear sequences in the plot of the trajectory of eye movements. Microsaccades occur roughly at a rate of 2 per second. Furthermore, they typically have an average amplitude of 22.6 arc minutes in monkeys (*Macaca mulatta*) (5). Two different techniques were employed to detect microsaccades and the results obtained were identical.

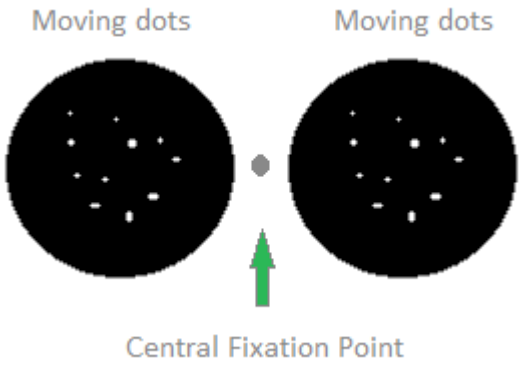

Fig. 1
A schematic of the experimental task that the monkey is trained to perform. The monkey releases a lever when the motion of the moving dots in the two patches becomes correlated.

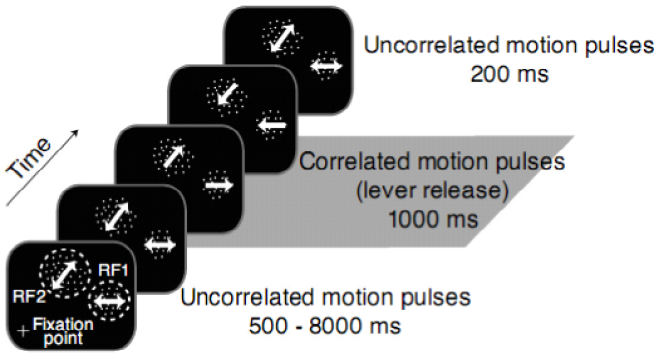

Fig.2
A schematic of the experimental task that the monkey is trained to perform. The monkey releases a lever when the motion of the moving dots in the two patches becomes correlated.

The first method is a modified version of the algorithm described by Engbert and Kliegl (2003). To detect microsaccades in two dimensional velocity space, it first transforms the time series of eye positions into velocities

$$\vec{v_n} = \frac{\vec{x}_{n+2} + \vec{x}_{n+1} - \vec{x}_{n-1} - \vec{x}_{n-2}}{6\Delta t} \qquad (1)$$

where Δt is the time delay between eye position samples, which, in the case of our experiment, would be 2 ms. Equation *(1)* represents a vector of average velocities over 4 position data points. Due to the random orientations of velocity vectors during fixation, the subsequent mean value is zero. As a result of their nature as outliers in velocity space, microsaccades can be detected by tracking their velocities.

The algorithm therefore uses the standard deviation of the velocity distribution as the mechanism for detection. Furthermore, in order to minimize the effect of background noise in the final computation, a median estimator was applied to the time series

$$\sigma_{x,y} = \langle v_{x,y}^2 \rangle - \langle v_{x,y} \rangle^2 \qquad (2)$$

where ⟨⟩ represents the median separator. The detection thresholds for the horizontal ηx and vertical ηy components are computed separately. Additionally, all trials are also computed independently as different trials may have different levels of noise

$$\eta_{x,y} = \lambda \sigma_{x,y} \qquad (3)$$

where λ is the threshold multiplier. To give the best results (see: Engbert and Kliegl (2003)), we use a value of λ= 6 .

The second technique entailed setting a series of parameters that had to be satisfied in order for an eye movement to be defined as a microsaccade. The parameters were obtained from a study on microsaccades by Martinez-Conde *et al.* (2004)(12) and slightly adjusted to compliment the experimental method used to capture eye positions (5). To be deemed a microsaccade, the eye movement had to be between 10 and 300 ms in duration, must start 20 ms after the previous microsaccade, must have a minimum length of 0.05 degrees, and must have no change in eye direction which exceeded 30 degrees for each 5 ms cut of the total time period of the microsaccade.

The accuracy of the two techniques was confirmed by visual inspection of the eye movements and enhanced by the fact that both methods provided identical results.

Results

The purpose of this investigation was to observe the effect of microstimulations on the production and characteristics of microsaccades. In order to conduct this scientific inquiry, we compared trials where there was no microstimulation with trials where microstimulation was introduced in synchrony with the low coherence motion stimulus during the motion detection experiment. An example trial with microstimulation is depicted in Figure 2. The microstimulation waveform is identical to the waveform of the motion stimulus in RDP1 (low coherence) but with a 50 ms delay.

Twenty experimental sessions containing roughly 1000 trials each were analyzed for this study. The conditions for a particular session were constant. Approximately half the trials in each session were experimental, during which we applied microstimulation to the MT of the monkeys. The other half of the trials were control trials. We measured three characteristics of microsaccades: frequency, average peak velocity, and average amplitude. For each session, the three features were computed separately for microstimulation and non-microstimulation trials. Figure 4 is a graphical illustration of the frequency comparison of the twenty sessions.

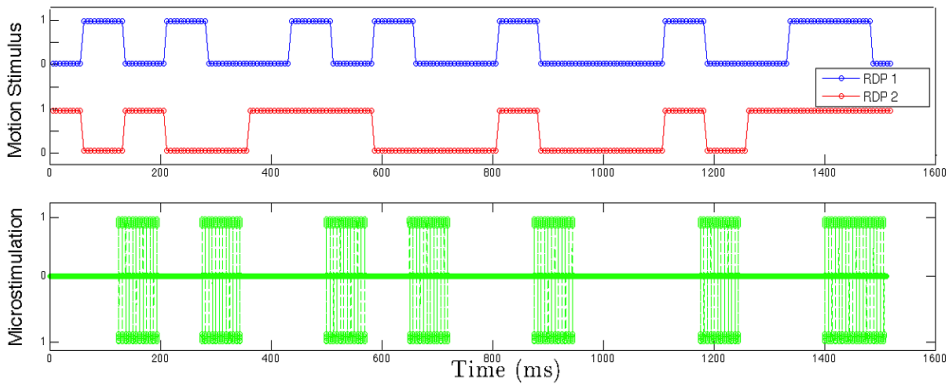

Fig. 3
Top: The motion stimuli of the two RDPs. The motion stimulus in RDP1 (blue) has low coherence (30%) at a value of 1 and no coherence (0%) at a value of 0. The motion stimulus in RDP2 (red) has high coherence (95%) at a value of 1 and no coherence (0%) at a value of 0.
Bottom: The microstimulation waveform. The waveform is in synchrony with the low coherence motion stimulus in RDP1 but with a systematic delay of 50 ms. Neurons in the receptive field overlapping RDP1 are being microstimulated when the value is 1 and there is no current being delivered when the value is 0.

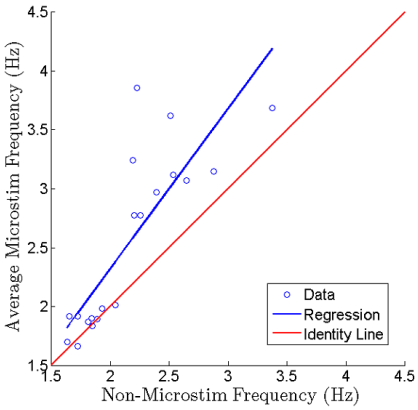

Fig. 4
The vertical axis represents the average microsaccade frequency for all trials across a session with microstimulation. The horizontal axis is the average frequency of the trials with no microstimulation for a particular session. There are twenty data points corresponding to the twenty sessions. The line of best fit has a slope of 1.326, which does not fall within the 95% confidence interval of a slope of one (the identity line), in red.

The figure's vertical axis is the average frequency of the microstimulation trials and the horizontal axis is the average frequency of the trials with no microstimulation. Each data point corresponds to one of the 20 sessions. The line of best fit, derived using a linear regression model, has a slope of 1.3626. It does not fall within the 95% confidence interval of a slope of one (the identity line). The steeper slope indicates that the microsaccade frequency increases for trials where microstimulation is applied to the MT area of the brain.

The average peak velocity across trial types is compared in Figure 5. The difference between average peak velocities of microstimulation and non-microstimulation trials is less prominent than the frequency difference. However, the line of best fit, with a steeper slope of 1.2933, fails to fall within the 95% confidence interval of the identity line. This result implies that the average peak velocity increases when area MT is microstimulated.

The difference in average amplitude was not significant as the line of best fell within the 95% confidence interval of a slope of one. Therefore, it points to no difference in amplitude upon the introduction of microstimulation.

In order to complete the analysis, and to demonstrate that the onset of microstimulation to the MT area was the cause of increase in microsaccade production, we performed a saccade-triggered average (STA) of the low coherence motion stimulus waveforms. The STA computed the average stimulus preceding a microsaccade for 500 ms. The motion stimulus was reduced to scalar values of 1 for coherent motion (low coherence) and 0 for no coherent motion. A comparison of trials with microstimulation and without microstimulation was conducted. Trials with microstimulation, had a corresponding microstimulation pulse for every coherent motion pulse (of the low coherence RDP) after a lag of 50 ms. This synchrony between the two waveforms allowed us to use STA to try to temporally link microstimulation to the generation of microsaccades. The results of the STA are illustrated graphically in Figure 5. It is evident upon inspection that the STA fails to conclusively reveal any correlation between microstimulation and the onset of microsaccades because the difference between the average stimulus for microstimulation and non microstimulation is not strong enough to be satisfactorily distinguished from noise.

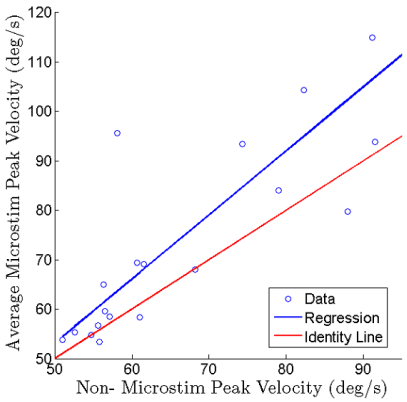

Fig. 5
The vertical axis represents the average peak velocity for all trials across a session with microstimulation. The horizontal axis is the average peak velocity for trials with no microstimulation for a particular session. There are twenty data points corresponding to the twenty sessions. The regression line has a slope of 1.2933 and this value is not within the 95% confidence level of the slope of the identity line (red).

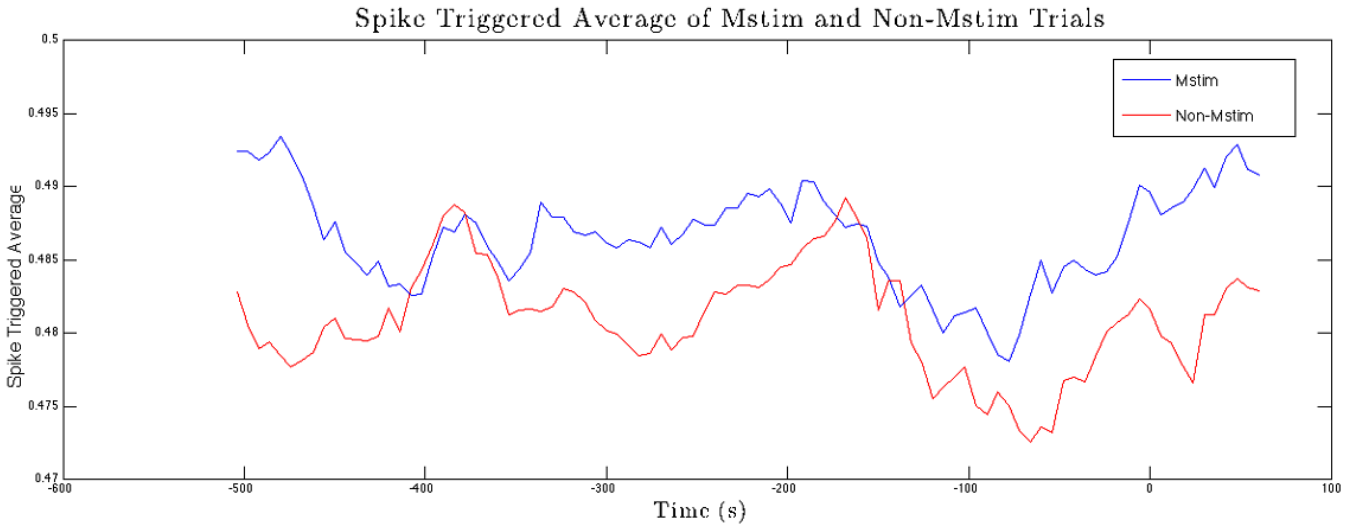

Fig. 6

Saccade-triggered average for trials with microstimulation and without microstimulation. The plot depicts the average motion stimulus 500 ms before the onset of a microsaccade. The motion stimulus used in the STA was from the RDP with low coherence and the stimulus was reduced to two scalar values for computing the average. A value of 1 was assigned when there was coherent motion and a value of 0 was assigned when there was no coherent motion.

Discussion

The initial analysis suggested that microstimulation caused an increase in microsaccade frequency and average peak velocity. Figures 3 and 4 revealed increases in microsaccade frequency and average peak velocity within the microstimulation trials of a session. The frequency appeared to be more affected than the average peak velocity, possibly due to the fact that microsaccades have a very specific velocity range (discussed in Data Analysis). This signifies that they cannot undergo radical velocity change, otherwise they would not be deemed a microsaccade. The STA analysis mentioned in the results section computed the average motion stimulus (from the low coherence RDP) amplitude preceding every microsaccade. This method was carried out in order to locate the burst of microstimulations that caused the extra microsaccdes in microstimulation trials. This was possible since the microstimulation pulses occurred almost concurrently (50 ms delay) with the coherent motion pulses (which were used in the STA analysis) in trials with microstimulation. If microstimulation had caused the increased generation of microsaccades in microstimulation trials, then within a certain time period preceding the microsaccade, we should find a coherent motion pulse, and therefore a corresponding microstimulation pulse. Since the coherent motion pulse has a scalar value of 1, this will cause a peak at some point in time preceding a microsaccade in the STA trace for microstimulation trials. This peak was not found from our STA analysis; as can be observed in Figure 6, there is no significant difference in amplitudes for microstimulation and non-microstimulation trials.

The disparate results of the two analyses creates an ambiguity surrounding the cause of the increase in microsaccade frequency. We were unable to satisfactorily establish any correlation between microstimulation and microsaccades; other explanations must therefore be entertained. The enigma surrounding the results of this study may be explained by the difficulty and unpredictability inherent in delivering microstimulation to MT neurons. For example, the tip position of the electrode can easily be repositioned between trials of the same session; this is due to pulsation of the brain and the moistness of its texture. Also, the two monkeys may have been reacting to the auditory stimuli generated by the onset of microstimulation, since microsaccade generation has known oculomotor mechanisms (7). In order to conclusively determine the effect of microstimulation on microsaccades, further analytical techniques need to be applied to do an exhaustive search for a temporal link between microstimulation and the generation of microsaccades.

Conclusions

The effects of microstimulation to the MT area on the generation of microsaccades were studied. Our preliminary results suggest that microstimulation caused microsaccades to occur more frequently and with a higher velocity. However, a deeper analysis revealed no correlation between the two. Although inconclusive, the results in this paper make this a rewarding avenue for future vision research, with implications for other microstimulation centered studies.

Acknowledgements

Haider Riaz would like to acknowledge his supervisor, Erik Cook, for introducing and allowing him to work on this project. Haider Riaz would also like to thank Felix Cormier and Shehla Wazir for advice on writing this paper. The authors would also like to thank the other members of the Cook Lab for their help and support at various stages during this project.

References

[1] Darwin, R. W.; Darwin, E. "New Experiments on the Ocular Spectra of Light and Colours". Philosophical Transactions of the Royal Society of London 76, 313-348 (1786).

[2] Martin Rolphs. "Microsaccades: Small steps on a long way". Vision Research 49, 2415–2441 (2009).

[3] T.N. Cornsweet. "Determination of the stimuli for involuntary drifts and saccadic eye movements." Journal of the Optical Society of America, 46 pp. 987–993 (1956).

[4] S Martinez-Conde, SL Macknik, XG Troncoso, TA Dyar. "Microsaccades counteract visual fading during fixation". Neuron 49 (2), pp. 297-305 (2006).

[5] Bridgeman B, Palca J. "The role of microsaccades in high acuity observational tasks". Vision Res 20:813-817 (1980).

[6] Rucci M., Iovin R., Poletti M., Santini F. "Miniature eye movements enhance fine spatial detail". Nature, 447 (7146), 851–854 (2007).

[7] Cohen and Newsome. "What electrical micros- timulation has revealed about the neural basis of cognition". Current Opinion in Neurobiology 14, 169–177 (2004).

[8] Masse and Cook. "Behavioral Time Course of Microstimulation in Cortical Area MT". Journal of Neurophysiology 103, 334–345, (2010).

[9] Harrington et al. "The Effect of Microsaccades on the Correlation between Neural Activity and Behavior in Middle Temporal, Ventral Intrapari- etal, and Lateral Intraparietal Areas". The Journal of Neuroscience 29 (18), 5793–5805 (2009).

[10] Bradley, D.C., Chang, G.C., and Andersen, R.A. "Encoding of three-dimensional structure-from-motion by primate area MT neurons." Nature 392: 714-717 (1998).

[11] Engbert, R, Kliegl, R. (2003). "Microsaccades uncover the orientation of covert attention.Vision Research." 43, 1035-1045 (2003).

[12] Martinez-Conde et al. "Microsaccades: A neurophysiological analysis". Trends in Neuroscience 32 (9), pp 463-475 (2009).

RESEARCH ARTICLE

High UV Excitation Intensity Induces Photoconversion of DAPI During Wide-Field Microscopy

Stefan Rodic[1]*, Claire Brown[2], Erika (Tse-Luen) Wee[3]

[1] Department of Biology, McGill University, Montreal, QC, Canada
[2] Department of Physiology, McGill University, Montreal, QC, Canada
[3] Advanced Bioimaging Centre, McGill University, Montreal, QC, Canada

*Email Correspondence:
stefan.rodic@mail.mcgill.ca

Keywords:
***DAPI:** 4',6-diamidino-2-phenylindole (DAPI) is a fluorescent stain that binds strongly to A-T rich regions in DNA.*
***Photoconversion:** A photochemical alteration of chemical structure upon the absorption of electromagnetic radiation.*
***Fluorescence Microscopy:** The use of an optical microscope that measures/visualizes electromagnetic radiation emitted from a substance in response to shorter wavelength incident radiation.*
***Photobleaching:** Loss of fluorescence by a pigment when illuminated due to photochemical reactions.*

Abstract

Background: Multi-color fluorescence microscopy is dependent on the spectral specificity of the dyes and probes used for localization. One of the most commonly used fluorescent DNA dyes is DAPI, which is usually excited by UV light to emit in the blue visible light range. Herein, we describe a pattern of decreasing DAPI fluorescence upon extended UV exposure, closely followed by an increase in emission maxima in the green range.

Methods: UV-induced photo-conversion of DAPI to green-fluorescing photoproducts was studied on Chinese hamster ovary cells using wide-field fluorescence microscopy, at different UV exposure times and intensities. Imaging was done in repetitive cycles, by alternating between a DAPI and FITC filter cube and following this with a 1 second UV excitation time. The effect of differing UV light intensities on the photo-conversion process was not previously described in the literature.

Results: Upon image analysis from a large sample of cells, the rate of photo-conversion was shown to be dependent on both the duration of UV excitation and the intensity of the UV light source. Both the process of DAPI depletion and photo-product growth showed biphasic exponential patterns of change. Furthermore, the level of DAPI fluorescence intensity was found to be negatively correlated with the green fluorescence of the photo-product.

Limitations: This study did not examine the effect of differing mounting media or a variation in DAPI concentration on the rate of DAPI photo-conversion. Also, the exact light dosage to the system was not measured from the 100W Hg bulb. Photo-bleaching of green fluorescence in cells not stained with DAPI was not measured to control for bleaching of endogenous cell molecules.

Conclusion: Based on our findings, a set of recommendations was formulated in order to help reduce the effects of UV-induced DAPI photo-conversion.

Introduction

Immunocytochemistry has proven to be tremendously useful in localizing and identifying molecules of interest within cells. The fluorescent dye 4',6-diamidino-2-phenylindole dihydrochloride (DAPI) is commonly used for visualizing the nucleus and DNA regions of the cell (1-3). DAPI binds to the minor groove of DNA strands, particularly A-T rich clusters (2, 3). Therefore, this common fluorescent dye has a multitude of applications either as a DNA-probe for flow cytometry or a dye for chromosome staining and simple DNA visualization in a variety of biochemical assays (3). Upon binding with DNA molecules, DAPI is most readily excited at 364nm wavelengths but has emission maxima in the 454nm range (4). By emitting within blue regions of the visible spectrum, DAPI nuclear staining can be used in concordance with other dyes emitting in different ranges of visible light. It is essential that the spectral properties of separate dyes remain unique and consistent, facilitating accurate fluorescence microscopy.

Besides simply exciting DAPI molecules to induce maximum fluorescence, UV light has also been shown to readily convert blue-emitting dyes such as DAPI or Hoechst 33258 into forms with green emission maxima (4-6). This UV-induced conversion generates photoproducts that not only emit light at longer wavelengths, but are also most readily excited by blue light. Through a complete spectral shift, the properties of these photo-products mimic those of fluorescein derivatives (FITC) or green fluorescent protein (GFP). If left unaccounted for, such photo-conversion could be severely detrimental to precise multi-color fluorescence microscopy due to false positive green signals in the nucleus.

Photo-conversion has also been shown to be dependent on the duration of UV-exposure yet independent of DNA binding, environment acidity/alkalinity or even the presence of a water solution (4, 6). The mechanism of this conversion is believed to be UV-induced oxidation, as studies have shown treatment of Hoechst 33258 with H_20_2 solution yielded similar increases in green intensity, although the effect was weaker with DAPI (4). Furthermore, mass spectroscopy analysis showed both UV exposure and H_20_2 increased the percentage of double protonated forms of DAPI. The photoproduct is likely the dye in this protonated state, a slight change in configuration that substantially alters the wavelengths of the excitation and emission maxima. A detailed study of DAPI can be complicated by its tendency to undergo photo-bleaching, which may or may not be a related process to photo-conversion. Likewise, the created photoproducts themselves have low stability and exhibit photo-bleaching after extended excitation. Interestingly, Zurek-Biesiada *et al.* noted that bleached DAPI signals regained ~50% of their initial levels after 1hr, while corresponding levels of the green-emitting photoproduct dropped ~50% over the same period (4). Such observations lead to speculation that the process of UV-induced photo-conversion is reversible in a subpopulation of molecules within this nuclear dye.

While planning a multi-color fluorescent assay using DAPI, it is important to consider a wide variety of factors that may potentially impact the rate of photo-conversion. Firstly, DAPI concentration has been found to be related to the rate of photo-conversion at levels between 0.1-1μM, where a higher concentration provides a larger pool of reactants to facilitate a faster conversion process (6). At high DAPI concentrations (7-10μM), fluorescent signaling is shown to decrease likely due to self-quenching, but this complication does not slow down photo-conversion (4). The increase in green intensity following UV excitation of DAPI was found when using a variety of mounting mediums and fixation protocols (5, 6). However, the use of glycerol as a mounting medium is particularly problematic as very high concentrations of glycerol in the system are proportional to the level of photo-conversion (6).

These considerations lead us to select the mounting reagent ProLong® Gold for experimentation. Despite being glycerol based, ProLong Gold reduces the extraneous impact of photo-bleaching, is a commonly used laboratory medium and would allow better comparison to previous studies which used it (4-6). Experiments using high powered lasers (e.g. 100mW and 1.25mW for excitation and imaging respectively)(4) or mercury metal halide lamps (100W)(6) have characterized DAPI photo-conversion in confocal microscopy. This study will use a metal halide lamp with a wide-field approach as done by Jez *et al.* (6)

Herein, we observe the increase of green signaling as UV exposure time increases, which will be referred to as FITC signaling due to the use of a FITC filter cube. It is the aim of this study to identify a set of protocols to reduce the rate of photo-conversion while further exploring the relationship between DAPI and its respective photoproduct. In addition, the previously unstudied effects of different UV intensities on this process were described.

Materials and Methods:

Sample preparation

Samples of Chinese hamster ovary cells expressing the focal adhesion adaptor protein Paxillin-GFP were cultured and prepared using standard protocols. The cells were stained with 100 μL of DAPI (5 mg/ml stock, 1:5000 dilution to 1 μg/ml) for 15 minutes at 23°C. They were then washed 3 times with 1ml PBS-and subsequently mounted on slides using ProLong® Gold antifade reagent (Life Technologies, Carlsbad CA, U.S).

Image acquisition

Observation of samples was done using a Zeiss AxioVert200M Inverted Microscope with motorized stage and a 63x/1.4NA oil immersion lens. Cells were first imaged using a FITC filter cube (467-498nm excitation, 513-556 emission), then using a DAPI filter cube (352-402nm excitation, 417-477nm emission) and finally were simply excited with UV light (100W Hg bulb) for a total of 1 second UV exposure per cycle. Exposure times for imaging were adjusted for optimal conditions based on the UV intensity, but total UV exposure was kept consistent. Sample cells were imaged alternately with the FITC and DAPI filter cubes for a total of 200 cycles (200s total UV exposure). Thirty different cells were imaged on 3 separate occasions for a total of 90 cells. This process was repeated for 100%, 50% and 10% intensities of the 100W mercury halide lamp for a total of 270 cells imaged.

Image analysis

Sample images were analyzed using MetaXpress 5.0 (Molecular Devices LLC, Sunnyvale CA, U.S) software. Images were first corrected for background fluorescence using the software tools and then the mean nucleic DAPI and FITC fluorescence changes was obtained for each cell. After confirming that there was no difference between the

3 sampling periods, the normalized nucleic fluorescence data of 90 cells per time-point per UV intensity were averaged together and statistical analysis was performed.

Results

Fixed and mounted Chinese hamster ovary cells with a paxillin-GFP marker were stained with DAPI. Blue and green fluorescence was observed using the DAPI and FITC filter cubes for differing UV light exposure times and intensities. It should be noted that any green signaling was referred to as "FITC signaling," but this involves green fluorescence from GFP and converted DAPI, imaged by a FITC filter cube. There is no FITC staining present, only the use of a FITC filter cube for the imaging of green fluorescence.

UV exposure causes a decrease in DAPI fluorescence

Upon exposure to UV light, there was an exponential decay in DAPI signaling probably due to both photo-bleaching and photo-conversion (Graphs 1-3, Fig.1). When comparing different UV intensities, there was a significant difference in the overall DAPI fluorescence change during the entire 200 second time course (Table 1). Among the differing intensities levels, DAPI signaling decayed most rapidly in the initial phases of UV exposure, followed by a considerably slower exponential decay component. Therefore, the following biphasic exponential decay regression was used to model this interesting trend.

$$f(x) = y_0 + a \cdot e^{-b \cdot x} + c \cdot e^{-d \cdot x}$$

The variables *b* and *d* represent the rate constants of the faster curve and slower curve respectively. All three DAPI models were well representative of the data with R^2 values of 0.9999, 0.9998 and 0.9998 for the 100%, 50% and 10% experiments and had random residual distribution (Graphs 8,10,12). The biphasic nature of this regression model is itself indicative of two separate decay process, the fast one perhaps representing photo-bleaching occurring in unison with the slower photo-conversion process.

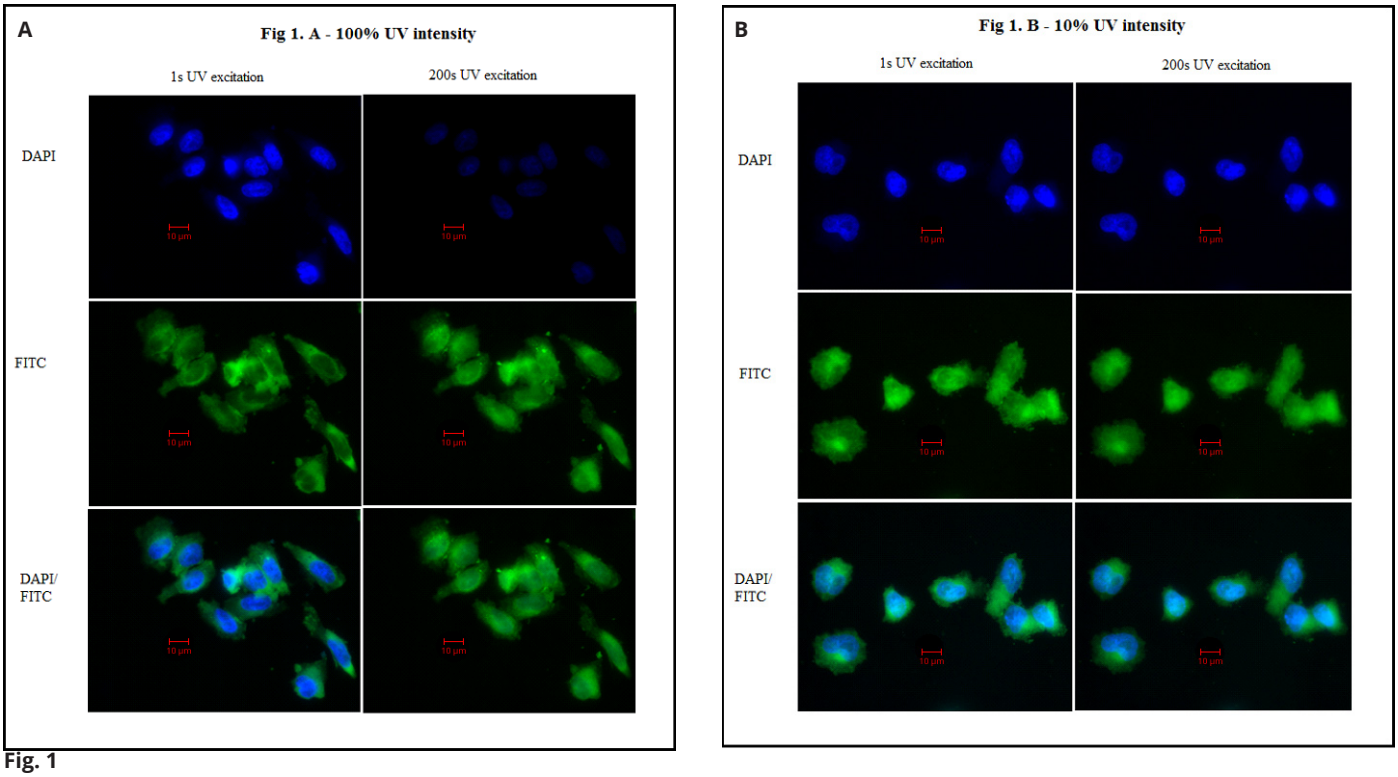

Fig. 1

Fluorescent imaging of 100% and 10% UV-induced DAPI photoconversion

A) The scale bars are 10μm in length. High DAPI fluorescence is shown in the upper left panel prior to extended 100% UV exposure. Following 200 seconds of UV excitation, the DAPI signal is almost completely extinguished while there is a corresponding increase in FITC fluorescence shown the in the middle two panels. Note that the increase in FITC fluorescence is primarily localized in the nucleus without substantial change in the cytoplasm, this supports the notion that it is the nucleic dye DAPI that is being photoconverted.

B) The scale bars are 10μm in length. The extent of DAPI depletion is not as noticeable after 200 seconds of 10% UV excitation while FITC signaling does not seem to be significantly effected also. When both the DAPI and FITC signals are overlain on top of each other, there appears to a minimal change in fluorescence due to photoconversion at this UV intensity.

	T-Test probability between different intensity groups		
Dye	100% and 50%	50% and 10%	100% and 10%
DAPI	2.11×10^{-70}	5.32×10^{-38}	9.86×10^{-93}
FITC	1.04×10^{-22}	3.42×10^{-10}	9.44×10^{-37}

Table 1. Probability associated with t-test between differing intensity groups.
Very low P-values were obtained when comparing the change in fluorescence between time points 1s and 200s, among differing intensity groups (i.e. comparing overall change in fluorescence during the time course between intensity groups). Although the differences between all three groups were significant, the greatest difference was between 100% and 10% groups, followed by the 100% and 50% groups.

Category	Fast Component			Slow Component		
UV intensity	100%	50%	10%	100%	50%	10%
Plateau (y_o)	0.083	0.218	0.365	0.083	0.218	0.365
Curve span (a or c)	0.2148	0.673	0.555	0.744	0.104	0.071
Rate constant in s^{-1} (b or d)	0.285 ± 0.032	0.147 ± 0.093	0.082 ± 0.043	0.0107 ± 0.0003	0.006 ± 0.0057	0.003 ± 0.005
Time constant (s)	3.50 ± 0.392	6.77 ± 4.28	12.1 ± 6.34	94.4 ± 2.65	158 ± 150	278 ± 463
Half-Life (s)	2.43 ± 0.273	4.69 ± 2.96	8.39 ± 4.39	64.7 ± 1.82	110 ± 104	192 ± 307

Table 2. Regression constants and half life of fast and slow DAPI curves.
The regression constants are indicated for each curve at differing UV intensity levels. 'Plateau' indicates the asymptotic value at which the curve converges after decaying over the entire curve span. The variables *a* and *b* belong to the fast component while *c* and *d* are from the slow component. The time constant is the inverse of the rate constant value, while the half life was calculated as ln2/(rate constant). The standard deviation values of the rate constant, time constant and half life are based on three separate trial curves obtained for each intensity experiment.

The three separate UV intensities differed substantially in the rate, at which DAPI signaling decreased, with the fastest rates present at higher UV intensities. The regression models predicted different plateaus for each of the three intensities. The plateau value for 100% UV intensity as a fraction was 0.08 of the original standardized maximal value, 0.22 for 50% UV intensity and finally 0.37 for 10% UV intensity (Table 2). Although these differences may be attributed to inaccuracies in the model, they suggest that higher UV intensity achieves more complete depletion of the DAPI pool. There also appear to be inherent threshold values determining the extent of DAPI depletion using the given apparatus as the model predicts 8% of the pool will always remain in theory, while closer to 18% remained in the 200 seconds actually tested (Table 2).

Comparatively, the fast components had a smaller span (distance between the plateau and starting point) than their faster counterparts for all UV intensities. Since the plateau is dependent on the span of the two separate components, the component with the greater span has a greater overall impact on how high the plateau of the regression will be. Despite having a slower rate constant, the slower process (photo-conversion) may have a larger final impact on DAPI depletion than photo-bleaching since this component has a larger 'span.' It is likely that the fast component has a reduced significance after the initial phases of UV exposure. Likewise, the rate constants of the fast components were over an order of magnitude greater than those of the slower components for all intensities. Among the fast/slow components themselves, the rate constants became smaller as the UV intensities decreased. This is subsequently reflected in the half-lives of the experiments, where there is a doubling in half-life between 100% UV intensity and 50%, followed by another doubling between 50% and 10%. This asymmetric trend in doubling indicates that a decrease in DAPI depletion is not related to UV intensity in a linear fashion, rather lower UV intensities have less of a decrease in depletion rate. In this respect, both the fast curves and slow curves mirrored each other and UV intensity seems to affect both processes equally. The standard deviation for the rate constant and half-life were based on three separate trial curves made per experiment. The standard deviations between these three trial regressions were greatest in the 50% and 10% UV intensities, particularly for the fast components.

The standard deviation of mean DAPI fluorescence was based on 90 samples for each intensity (all three trials averaged together) and gradually increased as UV exposure time went up. Although this increase in variation is to be expected in normalized data where nearly

all samples were initially at 100% fluorescence prior to UV exposure, it is indicative of differing rates of DAPI depletion among cells. These differing rates could be attributed to the differing individual contributions of photo-bleaching and photo-conversion within each sampled cell. The standard deviation was the highest at 10% UV intensity, it is likely that this UV level does not meet the threshold needed to induce a change in DAPI fluorescence in certain cells, thus causing more variability in the data than at high UV levels.

UV exposure causes an increase in FITC/GFP fluorescence

Concordant with an apparent decrease in DAPI fluorescence was an increase in the strength of FITC signaling that was reflective of exponential association (Fig. 1, Graphs 4-6). Once again, the data was noted to express two separate phases while increasing, therefore the following biphasic regression model was used:

$$f(x) = y_0 + a\cdot(1 - e - b\cdot x) + c\cdot(1 - e - d\cdot x)$$

The regression curves generated R^2 values of 0.9999, 0.9998 and 0.9977 for the 100%, 50% and 10% UV intensities respectively, while the residual values were low and random if the initial outlier values were excluded (Graphs 7,9,11). These outlier values present during the first few seconds of UV exposure were excluded from curve modeling (indicated by black dots in Graphs 4-6). Apart from possessing high variability and large standard deviation values, the outlier values were exceptions to the general increasing trend as they indicated rapid drops in fluorescence within the initial phases of UV excitation. The drop in fluorescence may be explained as initial photo-bleaching of the control levels of green fluorescence already within the cell prior to conversion (paxillin-GFP label), where this initial drop is quickly overcompensated for by the slower but more substantial DAPI photo-conversion process. In addition, the biphasic nature of the regression independent of these outliers could point to both a fast and slow conversion processes for increasing FITC fluorescence.

The vast majority of the 200 time points were fitted to exponential association curves, with initial starting points of 0.44, 0.63 and 0.80 for the 100%, 50% and 10% UV intensities (Table 3). A lower starting point from the maximal normalized value of 1 (often reached near the last time point) indicated a greater overall percentage of conversion. Although the general trend of increasing FITC signal strength was apparent at 100% UV intensity and to a lesser extent in the 50% UV data, the initial drop attributed to FITC photo-bleaching often canceled out photo-conversion at 10% so that FITC fluorescence levels would simply reach their starting point at the end of 200 seconds in many cells. The large standard deviation during these initial time points reflected a wide range of spectral behaviors among cells, where some did not exhibit bleaching phenotypes while others had a massive drop in FITC fluorescence that was only later followed by a conversion increase.

The slow components showed the same trend described in the DAPI models where there was a doubling in half time between 100% and 50%, followed by another doubling between 50% and 10%. In contrast, the fast FITC components showed a half-time doubling between 100% and 50% UV intensities, but a 25-fold increase between 50% and 10%. Thus, instead of there being an order of magnitude difference between the rate constants of the fast and slow components, they were the exact same at 10% UV intensity. This may indicate that the slow process increasing FITC fluorescence follows an expected trend at 10% UV, while the faster component is substantially inhibited from what is expected and may be the reason for an inhibited photo-conversion process. Additionally, it was half lives of the 10% fast and slow components that displayed the greatest standard deviation, which was calculated between the three separate trial curves for each experiment. Thus, there was substantial variation in the rate constants even among individual 30 cell trials, where 10% UV strength was not enough to induce a unanimous photo-conversion response.

Category	Fast Component			Slow Component		
UV intensity	100%	50%	10%	100%	50%	10%
Initial point (y_o)	0.443	0.635	0.801	0.443	0.635	0.801
Curve span (a or c)	0.211	0.094	0.382	0.386	0.393	0.375
Rate constant in s^{-1} (b or d)	0.080 ± 0.008	0.038 ± 0.014	0.002 ± 0.002	0.011 ± 0.001	0.005 ± 0.0005	0.002 ± 0.002
Time constant (s)	12.5 ± 1.20	26.0 ± 9.58	666 ± 666	94.3 ± 8.57	185 ± 18.5	666 ± 666
Half-Life (s)	8.63 ± 0.863	18.1 ± 6.67	462 ± 462	65.4 ± 5.94	128 ±1 2.8	462 ± 462

Table 3. Regression constants and half time of fast and slow FITC curves.
The regression constants are indicated for each curve at differing UV intensity levels. 'Initial point' indicates the value at which the curve meets the y-axis at 0 seconds. The variables a and b belong to the fast component while c and d are from the slow component. The time constant is the inverse of the rate constant value, while the half time was calculated as ln2/(rate constant). The standard deviation values of the rate constant, time constant and half life are based on three separate trial curves obtained for each intensity experiment.

Negative correlation between DAPI and FITC fluorescence

To better evaluate whether the decreases in DAPI signal strength were more attributable to photo-bleaching or photo-conversion, the level of both DAPI and FITC fluorescence were compared at equal UV exposure time points with linear regressions (R^2 values of 0.99). For all three intensities, a direct negative correlation was apparent between DAPI and FITC fluorescence (Graph 13). The ratio of DAPI:FITC fluorescence was not 1:1, instead the slope was -1.7, -1.5 and -1.4 for the 100%, 50% and 10% UV intensities respectively. Thus, there is a greater drop in DAPI fluorescence than increase in FITC fluorescence. It can therefore be concluded that the UV-induced decrease in DAPI signal could mostly be attributed to photo-conversion to green-emitting photoproducts. Photo-bleaching still does have a significant impact on DAPI depletion despite the use of ProLong Gold and its effect was greater at higher intensities than lower ones (more negative slope). Cells exposed to lower UV intensities did have higher DAPI to FITC ratio starting points compared to their counterparts samples exposed to higher UV intensities.

Additionally, outside of each linear regression there was a tail pattern that became more apparent at lower UV intensities. FITC signaling quickly dropped at high-DAPI/low-FITC levels (corresponding to early UV exposure time-points). This peculiarity could once again be attributed to early photo-bleaching of the control FITC fluorescence in the cell prior to conversion, where the green emitting molecules are bleaching faster than can be compensated by early photo-conversion.

Discussion

The depletion of DAPI in response to UV excitation has been demonstrated to be directly related to an increase in FITC fluorescence and thereby an increase in green-emitting DAPI photoproducts. At all intensities, the duration of UV exposure was related to the level of photo-conversion. Lower conversion rates and partial saturation of the system occurred at around 100 seconds at 100% UV intensity. Previous studies have observed a conversion plateau between 32 seconds and 4 minutes, probably attributable to the initial size of the conversion reactant pool (DAPI concentration) and the power of the UV light source (4-6). We used a similar set-up to Jez *et al*, (100W metal halide lamp/wide-field) who found a plateau of 32 seconds at 100% UV intensity. However, this was done using a mounting medium with a high glycerol concentration, while using ProLong Gold they too described the response as significantly less robust (6). Although the automated intermittent FITC imaging during UV excitation may have slowed down the rate of DAPI photo-conversion by giving time for a reverse reaction, this is unlikely significant as reversal occurs on the order of minutes to hours and not fractions of a second (4).

DAPI fluorescence decayed in a biphasic exponential manner, likely due to the initial fast process of photo-bleaching followed by slower photo-conversion. The reason that photo-bleaching was hypothesized to be the slower process is due to the lagging increase in the FITC signal behind the initial DAPI drop. The green-emitting molecules already present in the cells experienced their own photo-bleaching effect, but this was short lived during early UV exposure times and quickly compensated for by an increase in photo-conversion products. The photoproducts themselves also showed a biphasic pattern of growth, ultimately leveling off as DAPI substrate concentrations decreased. One hypothesis for the two-phase nature of this growth could be that the direct and fast process of DAPI-to-photoproduct conversion occurs alongside a slower indirect process of bleached DAPI-to-photoproduct conversion. As the initial pool of pure DAPI disappears, the growth curve shifts more and more to this secondary slower process that requires additional steps before the substrate can indirectly be converted to the photoproduct. An alternative mechanism would involve an increase in the rate of the reverse reaction, alongside a decrease in the availability of DAPI substrate as the photoproduct concentration increases. These two factors would gradually shift the equilibrium towards a slower increase and potentially reduce the intensity of FITC signaling completely below the sensitivity of the assay if observed long enough.

The rate of photo-conversion was substantially lower while using 10% UV concentrations, where most of the conversion inhibition seemed to originate from an inhibition of the fast component rate constant. Instead of being an order of magnitude faster than the slow component as was the case with the other intensities, the 10% fast component has the same half-life as the slow component. It is possible that 10% UV intensity is below a given threshold needed to sufficiently allow the fast process to overcome the initial dip in FITC fluorescence due to bleaching of green-emitting molecules. This study did not examine the effect of differing mounting media or a variation in DAPI concentration on the rate of DAPI photo-conversion. Also, the exact light dosage to the system was not measured from the 100W Hg bulb. Photo-bleaching of green fluorescence in cells not stained with DAPI was not measured, thus the speculated photo-bleaching quickly occurring at the beginning of excitation was not controlled for. Instead of looking at the change in green fluorescence in cells labelled with Paxillin-GFP, using a cell line with no endogenous green fluorescence and a red counterstain could have avoided the problem of inherent green photo-bleaching within the cell's endogenous molecules.

Conclusions

Based on these findings, the following set of protocols were formulated in order to reduce the potential negative consequences of unexpected DAPI photo-conversion:

1. UV intensities should be kept at 10% that of standard levels (100% intensity of a 100W Hg bulb) or less whenever possible, despite the needed increase in imaging exposure times.
2. Limit total UV exposure times to a few seconds at 100% UV intensity and up to 50 seconds at 10% intensity (at which point FITC fluorescence returns to control levels after dipping initially).
3. The use of lowest DAPI staining concentrations possible and mounting agents with lower glycerol levels (6).
4. Acquire DAPI images after all other higher wavelength images in order to eliminate green emission false positives.
5. Use alternate DNA dyes such as DRAQ5 which fluoresce in the far red regions of the spectrum and has not been shown to exhibit photo-conversion (7). Hoechst 3258 and Vybrant DyeCycle blue dyes are not suitable alternatives as they experience photo-conversion at a comparable level to DAPI (4).

Acknowledgments

A special thanks to the tireless help and guidance of Dr. Claire Brown and Erika Wee throughout this project. Their expertise and kindness was invaluable for the completion of this study.

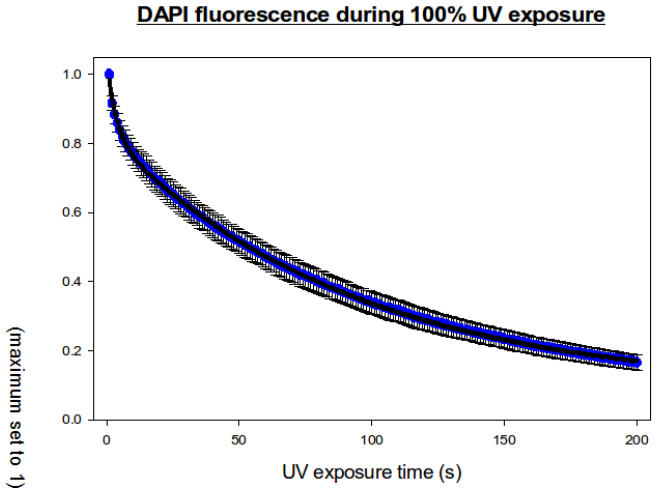

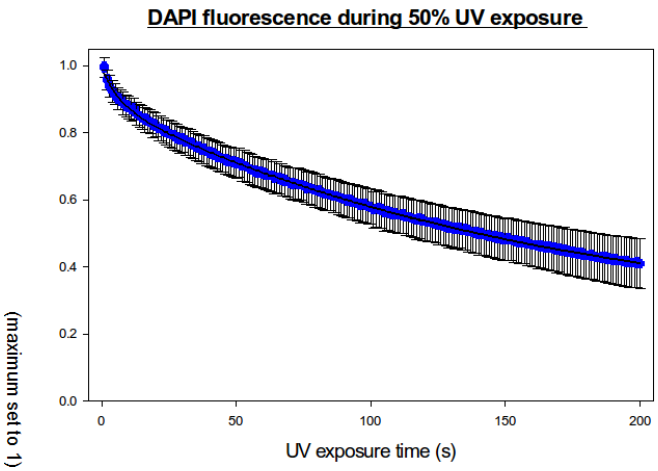

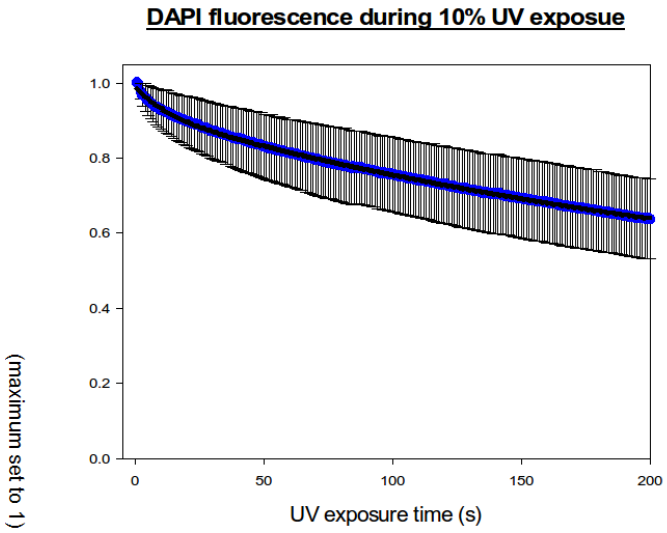

Graph 1-3. DAPI fluorescence during UV exposure. **Graph 1** shows a substantial decrease in normalized DAPI fluorescence after 200 seconds of 100% UV excitation. This trend is not as apparent in **Graph 2** and is even weaker in **Graph 3** at 10% UV exposure levels, where there was large variability in fluorescence at individual time points as indicated by the large error bars representing the fluorescence standard deviation. When the UV intensity is high, most cells follow expeirence biphasic exponential DAPI signal decay, however at lower UV levels many cells do not experience this effect uniformly.

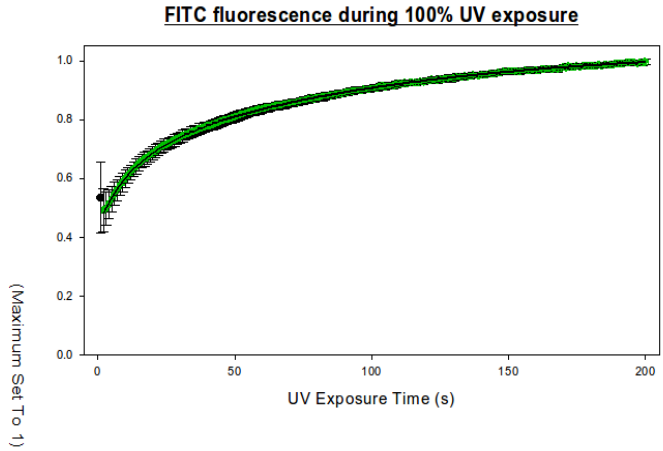

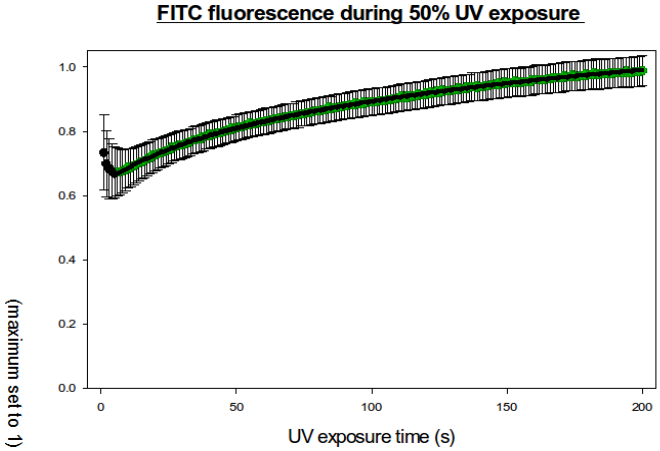

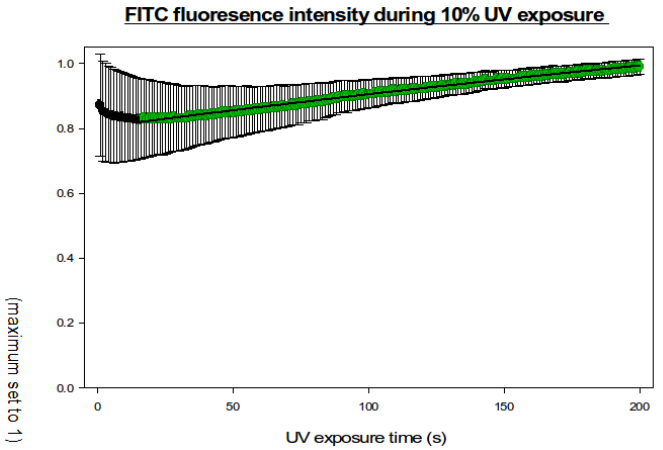

Graph 4-6. FITC fluorescence during UV exposure. **Graph 4** shows a substantial increase in normalized fluorescence of FITC after 200 seconds of 100% UV excitation. This exponential biphasic trend is only interruppted by variable outliers in the initial phase of excitation, represented by black dots with large error bars. The exponential association is not as apparent in **Graph 5** and is even weaker in **Graph 6** at 10% UV exposure levels, where there was large variability in fluorescence at individual time points as indicated by the error bars

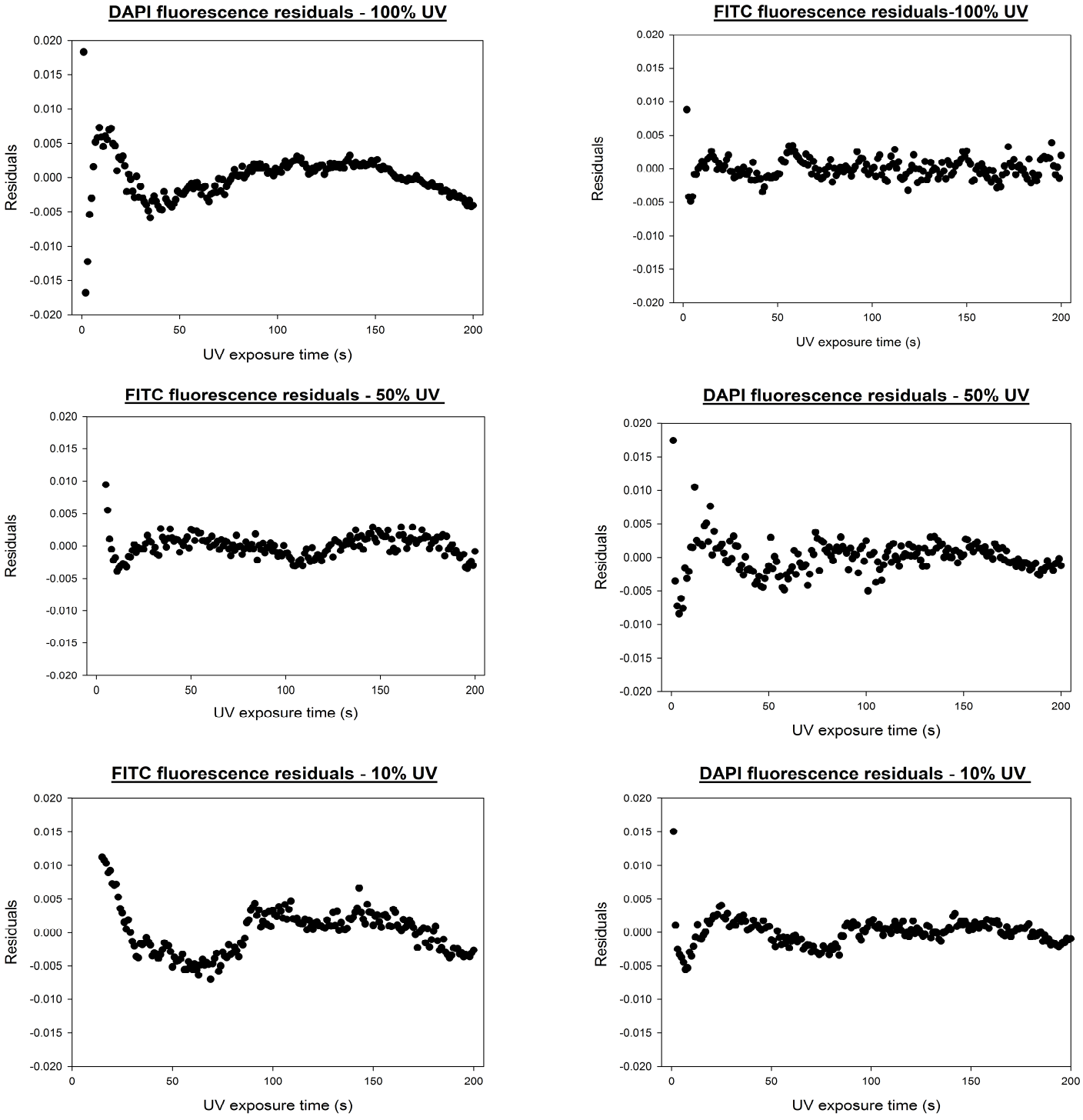

Graph 7-12. Regression residuals.

The residuals of Graphs 1-6 are shown individually to assess the quality of the exponential regression used for modeling. All residual data indicates a random distribution alongside relatively insignificant distances between the predicted values and the actual experimental values, indicating the regressions are a good fit. It should be noted that the initial decreasing outliers for the previous FITC graphs were not included as part of the regressions and therefore do not have representative residual values.

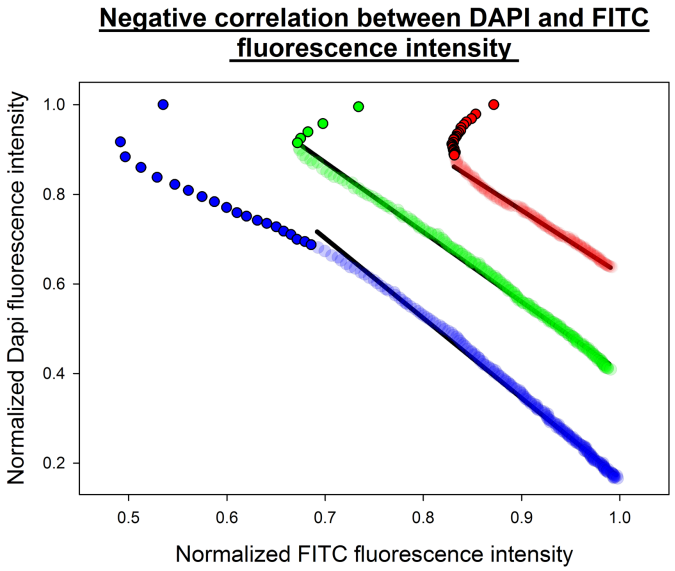

Graph 13. Negative correlation between DAPI and FITC fluorescent intensity.
The right, middle and left circles indicate 10%, 50% and 100% UV intensity time point values respectively. The transparent datapoints represent those included in the linear regression formula. The solid color datapoints are outliers to this linear correlation trend Linear regression are indicated by black lines, with slopes of -1.78, -1.56 and 1.41 for the 100%, 50% and 10% UV intensities.

References

[1] Waggoner, A., Taylor, L., Seadler, A. & Dunlay, T. Multiparameter fluorescence imaging microscopy: reagents and instruments. Human pathology 27, 494-502 (1996).
[2] Chazotte, B. Labeling nuclear DNA using DAPI. Cold Spring Harbor protocols 2011, pdb prot5556 (2011).
[3] Kapuscinski, J. DAPI: a DNA-specific fluorescent probe. Biotechnic & histochemistry : official publication of the Biological Stain Commission 70, 220-233 (1995).
[4] Zurek-Biesiada, D., Kedracka-Krok, S. & Dobrucki, J.W. UV-activated conversion of Hoechst 33258, DAPI, and Vybrant DyeCycle fluorescent dyes into blue-excited, green-emitting protonated forms. Cytometry. Part A : the journal of the International Society for Analytical Cytology 83, 441-451 (2013).
[5] Piterburg, M., Panet, H. & Weiss, A. Photoconversion of DAPI following UV or violet excitation can cause DAPI to fluoresce with blue or cyan excitation. Journal of microscopy 246, 89-95 (2012).
[6] Jez, M., et al. The hazards of DAPI photoconversion: effects of dye, mounting media and fixative, and how to minimize the problem. Histochemistry and cell biology 139, 195-204 (2013).
[7] Martin, R.M., Leonhardt, H. & Cardoso, M.C. DNA labeling in living cells. Cytometry. Part A : the journal of the International Society for Analytical Cytology 67, 45-52 (2005).

RESEARCH ARTICLE

Development of a Cellular System to Identify Modulators of B-Raf Induced Senescence in Human Fibroblasts

Ran Shu[1]*

[1] Department of Biochemistry, McGill University, Montreal, QC, Canada

*Email Correspondence:
ran.shu@mail.mcgill.ca

Keywords:
Tumorigenesis: *The transformation of normal cells-which grow only under favorable conditions- to cancer cells, which grow uncontrollably.*
Oncogene: *A gene that has the potential to cause cancer when mutated.*
Oncogene Induced Senescence: *A state of growth arrest in cells driven by the expression of an oncogene.*
Genetic Screen: *An experimental technique used to identify potential genes involved in the expression of a phenotype of interest.*

Abstract

Background: B-Raf is one of the earliest and most common genetic mutations observed in many different types of cancers. A single mutation in B-Raf cannot cause full-blown cancer, but may cause an observed phenotype called oncogene induced senescence (OIS). This suggests the need for cooperation between B-Raf and other genes for successful tumorigenesis.

Objective: We look to characterize Human Fibroblast cells that are able to senesce in response to elevated oncogenic expression of B-Raf.

Methods: We introduced ectopic expression of inducible B-Raf into human fibroblast cells. We characterized the successfully infected cells based on their ability to induce senescence.

Results: We isolated cells of clonal origin and we identified the clone most responsive to B-Raf expression.

Conclusions and Future Research: Our methodology proved to be effective in creating a model of B-Raf expression that can be used to study OIS. The next step is to screen the cells to identify genes that enable the cells to evade senescence. These genes could prove to be valuable chemotherapeutic targets.

Introduction

The MAPK/ERK pathway plays an important role in the regulation of cell proliferation, differentiation, survival and apoptosis in many organisms (1). This signal cascade starts with the binding of a mitogen to a cell surface receptor, activating members of the Ras GTPase family (1). Activation of Ras involves switching from a GDP-bound state to GTP-bound state and activating the downstream element Raf (1). There are 3 homologs of Raf proteins, *A-RAF*, *B-RAF*, and *C-RAF*, but research has been focused on B-Raf as its mutations have been observed in melanomas, thyroid and, colorectal cancers (2). Raf is a serine/threonine protein kinase that activates the downstream element MEK by phosphorylation. Activation of MEK, another serine/threonine kinase, allows it to phosphorylate p42 and p44 Erk kinases, converting them to the active states p42 phospho-Erk and p44 phospho-Erk (1). Finally, the Erk kinases can phosphorylate other transcription factors, ultimately leading to cell growth and proliferation. The loss of function or gain of function of any component of this pathway can have detrimental effects to the overall function of the organism.

Normal expression of Ras and Raf causes cell growth, however, constitutive expression of Raf and Ras in normal cells induces the phenotype of oncogene-induced senescence (OIS) (3, 4). This state of irreversible growth arrest is thought to be a protective mechanism used by the cell as a defense against tumorigenesis and to allow for the repair of cell cycle machinery (5). Senescent cells display special cell properties such as an elongated cell morphology and beta-galactosidase activity (6). OIS greatly resembles replicative senescence

where a cell's telomeres are shortened to the point where cells can no longer proliferate (7).

The biochemical mechanisms governing how senescence is induced are unknown, however candidates include p53, cyclin-dependent kinase inhibitors (CDK) inhibitors, $p21^{Cip1}$, $p16^{Ink4a}$, and other factors involved in telomere maintenance, such as telomerase, TRF1 and TRF2 (3). Aberrant expression of p53, p16, and p21 genes often leads to tumorigenesis, likely due to the ability of the cancerous cells to bypass the senescent mechanism (8). The loss of p53 may promote transformation through evasion of apoptosis as well(9). On the other hand, overexpression of telomerase can bypass the Hayflick limit - the number of times a normal cell will divide before cell division stops, and lead to the immortalization of cells(10).

Upregulation of the oncoproteins Ras or Raf is insufficient to induce uncontrolled growth in normal cells- rather cells need the cooperation of other genes in order to successfully transform (11). A likely mechanism of transformation is the loss of tumour suppressor genes, as their expression usually inhibits cell growth. The candidate approach and looking at specific genes greatly limited previous studies scope, and these experiments likely missed many relevant genes involved in the senescence mechanism. The question is also raised of whether or not changes in gene expression are of causality or of correlation.

We used a lentiviral vector containing the conditionally active ΔB-Raf-ER* construct to successfully transfect the cells. ΔB-Raf-ER* is stabilized by 4-hydroxy-tamoxifen (4-HT) binding, causing dimerization of the chimeric protein, translocation into the nucleus and increased B-Raf expression. We screened multiple clones obtained from infection based on responsiveness to 4-HT and B-Raf signaling, and the induction and maintenance of senescence. Having clones being able to grow in the presence of 4-HT and B-Raf signaling would result in false positives. After careful selection, we identified clone 2 as the best candidate.

The next step of the experiment would be to screen the genome through the systematic knockdown of genes with clone 2. The identification of these genes as requisites for B-Raf driven oncogenic transformation would provide new targets for drug development and a better understanding of oncogenic mechanisms.

Materials and Methods

Construction of Lentivirus Expression Vectors

We conducted the experiment using immortalized HF-E1T cells (human fibroblasts) transduced with the appropriate pLEGblast lentiviral stocks.

Lentiviral vectors encoded either ΔB-Raf-ER* or mCherry. ΔB-Raf-ER* is a fusion protein consisting of the protein kinase domain of mouse B-Raf linked to mouse estrogen receptor (ERα). The ER receptor is engineered to be non-responsive to β-estradiol, but retains responsiveness to 4-hydroxy-tamoxifen (4-HT) and the ICI series of estrogen receptor antagonists (12). We gateway cloned the B-Raf-ER* cassette from the pBabe vector into the pLEG vector (13). mCherry is a monomeric fluorescent protein. Cells with the mCherry vector lack an estrogen receptor and are not responsive to 4-HT.

Cell Culture, Lentiviral Production, and Infection

We cultured all cells in Dulbecco's modified Eagle's Medium (DMEM) supplemented by 10% Fetal Bovine Serum, penicillin and streptomycin. We cultured cells in a humidified environment containing 5% (v/v) CO2 at 37 °C. We prepared 4-HT (Sigma) as 1 mM stock solution in ethanol, stored at -20 °C and diluted to appropriate concentrations.

We obtained lentiviral stocks by polyethylenimine transfection of the appropriate vectors along with lentiviral packaging plasmids into 293T cells. We cultured targeted cells in blasticidin to select for successfully infected cells. We isolated individual cell clones into different plates. We obtained 9 independent clones, labeled as clones 1-3, 6,7, 9-12. Following selection we isolated cells into individual plates and allowed to grow on their own. We tested their responsiveness to 4-HT in the Characterization of B-Raf clones experiment, dose-response curves and time courses.

Cell Characterization

Characterization of B-Raf Clones

We seeded the clones and cells expressing mCherry at 40,000 cells per well in a 6-well plate which was left for a day in normal media. We then treated wells with either 1 uM of Ethanol or 10 nM of 4-HT. Each condition was done in triplicate. We allowed the cells to grow for 4 days before counting them with a hemocytometer.

Dose-Response Curve and Time Course

For dose-response curves, we seeded the cells at 15,000 cells per well in a 12-well plate and left for a day. We then treated wells with increasing concentrations of 4-HT. Each concentration was done in triplicate. We allowed the cells to grow for 7 days before counting. We replaced media containing 4-HT after 3 days with media containing the same concentration of 4-HT. We constructed the characterization of B-Raf clones and time course experiments in a similar manner to that of dose-response curves, except that the wells were all treated with 100 nM 4-HT. The cells were counted using a hemocytometer on days 2,4, and 6.

Screen for Escape Frequency

We seeded mCherry cells and HF-E1T:ΔB-Raf-ER* , clones 2,6, and 12

at 106 cells in 150 mm dishes. We either seeded clones 2,6, and 12 alone or with 100 or 1000 mCherry cells. We the treated all cells with 100 nM 4-HT for 4 days. We replaced the media with normal media without 4-HT and changed every 3-4 days over the span of 2 weeks. We seeded the mCherry expressing cells with clones to insure that the 4-HT media allows cell growth. We then stained the plates with Giemsa and visualized for colonies that grew out. Giemsa stains for DNA, therefore the darker the shade of purple from Giemsa stain, the more colonies that are present. The experiment was conducted twice.

Preparation of Cell Extracts and analysis by Western Blotting

We serum starved cells through treatment with DMEM with penicillin and streptomycin for 12 h. For the first Western blot, we treated ΔB-Raf-ER* human fibroblast clones with increasing amounts of 4-HT (0-100 nM) for 24 hours. We treated mCherry cells with 0 and 100 nM of 4-HT and used these cells as a control. For the second Western blot, we treated ΔB-Raf-ER* human fibroblast clones with 100 nM 4-HT for increasing periods of time. We counted 510,000 cells from each condition and lysed in 100 uL of 1X Laemmli Lysis Buffer. We directly loaded and electrophoresed aliquots of cell lysates through 12% polyacrylamide gels. We transfered the gels to PVDF membranes (Bio-RAD) and incubated in primary antibodies overnight at 4 °C. Primary antibodies used are as follows: Polyclonal rabbit anti-ERα (Santa Cruz Biotechnology, sc-543) used at a dilution of 1:200, monoclonal mouse anti-p-ERK (Cell Signalling Technology, 9106) used at a dilution of 1:2000, and monoclonal rabbit anti-ERK (Cell Signalling Technology, 9102) used at a dilution of 1:1000. Horseradish peroxidase-conjugated anti-mouse and anti-rabbit immunoglobulins were from Amersham and used at a dilution of 1:5000. We developed Western blots with the ECL Western Blotting detection kit (Amersham).

Results

We obtained 9 independent clones after infection with pLEG-B-Raf-ER* vector and blasticidin selection. In order to test responsiveness to 4-HT, the characterization of B-Raf clones experiment was conducted. The results are shown in Fig. 1. 4-HT treatment caused all clones to adopt pronounced morphological changes. Cells displayed an extended shape with a spherical cell body. Relative cell numbers were obtained by dividing the cell count from 4-HT treatment by the cell count obtained from ethanol treatment. The relative cell counts are shown in Fig. 2. Varying levels of growth arrest were observed in the clones. Clone 1 showed a very low level of growth arrest whereas clones 2,6 and 12 showed the highest levels. Clones 2, 6 and 12 were selected for further characterization with dose-response curve and time course experiments.

Dose-Response Curves

We wanted to determine the minimal concentration of 4-HT required for the activation of B-Raf and senescence induction in the maximal number of cells. A concentration that was too low would result in insufficient levels of 4-HT and B-Raf signaling, whereas too much could result in cell apoptosis(14). We incubated cells in full media containing increasing concentrations of 4-HT (0-100 nM) for 7 days before their numbers were quantified. The values obtained were normalized to that of cells treated with 0 nM of 4-HT. The results are shown in Fig. 3.

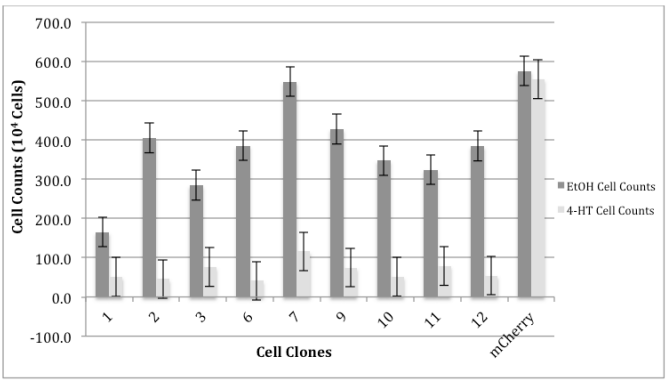

Fig. 1

Characterization of B-Raf Clones: B-Raf induced senescence of HF-E1T cells. Average cell count comparison between ethanol and 4-HT treatments for clones and mCherry cells. Growth curve I was conducted by first seeding 40,000 cells into 6 well plates and leaving them for a day. The cells were then treated with either Ethanol or 10 nM 4-HT and allowed to grow for 4 days before counting. Each condition was done in triplicate.

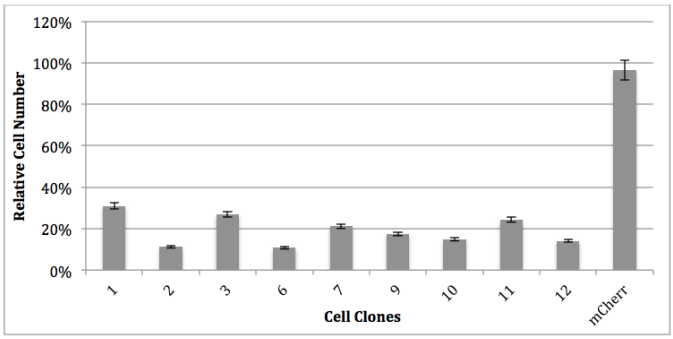

Fig. 2

Characterization of B-Raf Clones: B-Raf induced senescence of HF-E1T cells. Relative cell counts were obtained by dividing the cell count obtained from 4-HT treatment by the cell count obtained from ethanol treatment. Growth curve I was conducted by first seeding 40,000 cells into 6 well plates and leaving them for a day. The cells were then treated with either Ethanol or 10 nM 4-HT and allowed to grow for 4 days before counting. Each condition was done in triplicate.

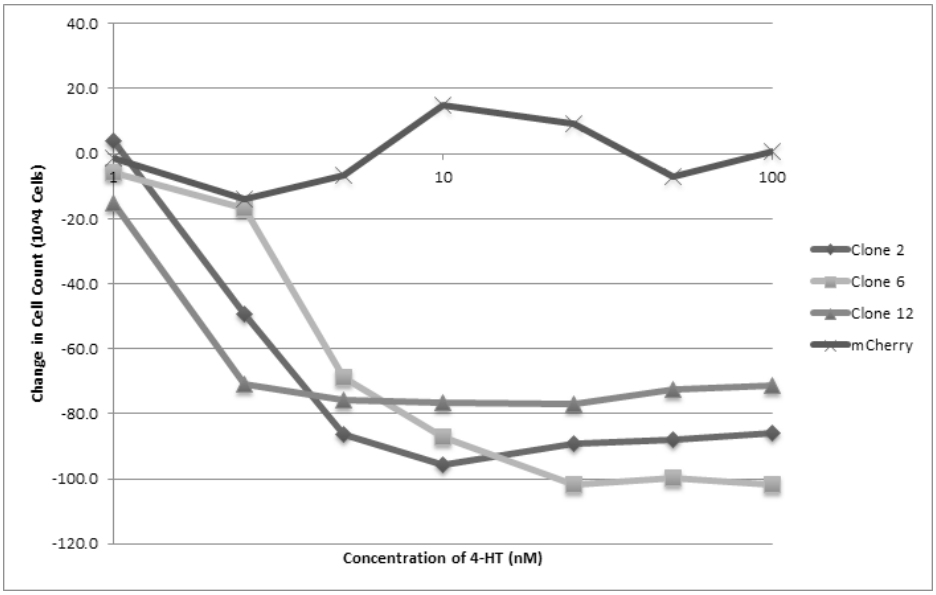

Fig. 3
Dose Response Curve: B-Raf induced senescence of HF-E1T cells with increasing concentrations of 4-HT. The cell counts were normalized to the cell count obtained at a concentration of 0 nM. Dose response curves were conducted by first seeding 15,000 cells into 12 well plates and leaving them for a day. The cells were then treated with increasing concentrations of 4-HT and allowed to grow for 7 days before counting. Each concentration of 4-HT treatment was done in triplicate.

mCherry cells were unresponsive to 4-HT treatment and show relatively consistent cell counts across the concentrations of 4-HT. Clones 2, 6 and 12 show growth arrest at increasing concentrations of 4-HT. Clones 2 and 6 have more of a gradual decrease in cell count as concentration increases, whereas clone 12 has a more abrupt drop in cell count. 25 nM appears to be the minimal concentration required to induce cellular senescence. However, concentrations 25-100 nM may also show the ratio of apoptosis and proliferation near one.

Time Course

The amount of time required for the induction of senescence is directly dependent on the activation of ΔB-Raf-ER*, its downfield cascade and growth arrest machinery. We wanted to determine how quickly cells would respond to ΔB-Raf-ER* activation and how its activation would affect cell proliferation. We chose a concentration of 100 nM of 4-HT to treat the cells, well above the minimal concentration required for senescence induction determined from the dose-response curves. We chose a concentration of 100 nM to make sure that the least number of cells would escape senescence and to keep it consistent with the Characterization of B-Raf Clones experiment. We normalized the results obtained to the cell counts obtained on day 0. The results are shown in Fig. 4.

In all cases, treatment with ethanol did not affect growth of cells. mCherry cells treated with 4-HT were unaffected and grew as quickly as in ethanol. Clones 2, 6 and 12 all exhibit senescence after 2 days of 4-HT treatment and stay at a similar cell count until day 6.

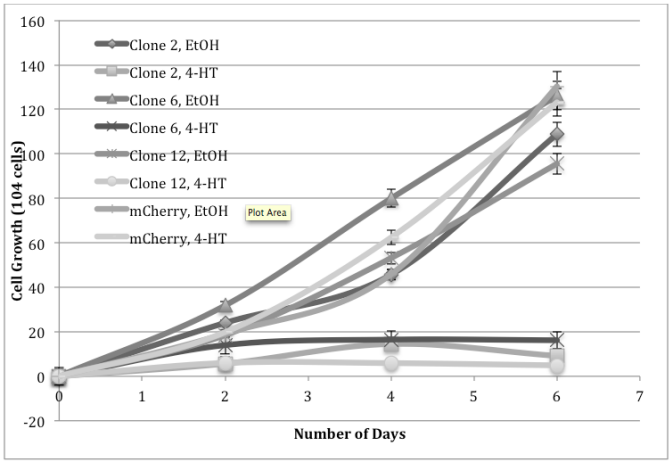

Fig. 4
Time Course: B-Raf induced senescence of HF-E1T cells with increasing time of exposure to 4-HT. The cell counts were normalized to the cell count obtained at day 0. Growth curve II was conducted by first seeding 15,000 cells into 12 well plates and leaving them for a day. The cells were then treated with 100 nM of 4-HT and counted on days 0, 2, 4 and 6. Each condition was done in triplicate.

Screen for Escape Frequency

The ultimate goal of the genetic screen is the determination of genes that are involved in the evasion of senescence. It's therefore imperative that cells are responsive to 4-HT and B-Raf signaling to become senescent. Any cells able to evade the senescence mechanism without the knock down of a gene would lead to a false positive. We conducted the screen for reversion frequency as described in methods.

Clones 2 and 12 without any mCherry cells had uniformly lightly coloured plates without any dark spots illustrating that no colonies had escaped senescence. Clone 6 without any mCherry cells had many colonies grow out and had a much darker stain compared to that of clone 2 and 12. The plate with only mCherry cells had a uniformly darker shade compared to that of clones 2 and 12 without mCherry cells, and was similar in colour to that of clone 6 without mCherry cells. This observation illustrates that mCherry cells and clone 6 cells had a similar number of cells in the wells. Clones 2 and 12 with mCherry cells showed darker regions on the plates due to mCherry cells being unaffected by 4-HT and growing out. There was very little difference in colour between clone 6 plates with and without mCherry cells, demonstrating that clone 6 cells were able to evade senescence. The ability of clone 6 to grow out in the presence of 4-HT removed it from any further experiments. The results are shown in Fig. 5.

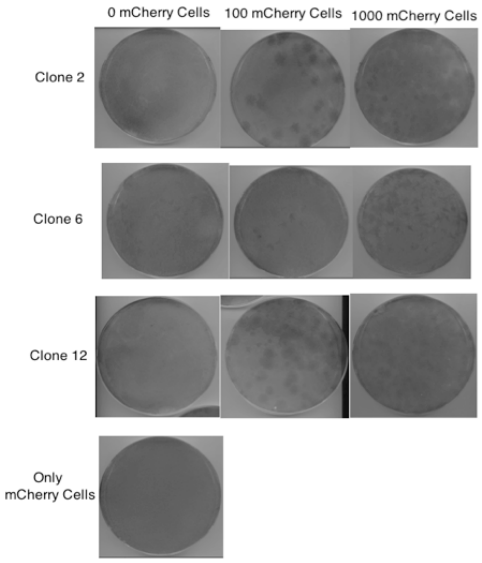

Fig. 5

Screen for Escape Frequency: B-Raf induced senescence of HF-E1T cells in the presence of 4-HT with or without mCherry cells. The screen for escape frequency was conducted by first seeding 10^6 mCherry cells, clones 2,6 and 12 into 150 mm plates. The plates of clones were either seeded alone or with 100 or 1000 mCherry cells. After a day, all the plates were treated with 100 nM of 4-HT for 4 days before replacement with normal media for two additional weeks.

ΔB-Raf-ER* Signaling in 4-HT treated Cells

We wanted to demonstrate that 4-HT treatment caused an increase in ΔB-Raf-ER* signaling in cells by conducting Western blots. We conducted the first blot by treating cells with increasing concentrations of 4-HT; we conducted the second one by treating cells with increasing times of exposure. We blotted both Western blots for estrogen receptor ERα, protein kinase Erk and its phosphorylated form phospho-Erk (p-Erk). Estrogen receptor is usually degraded by the proteasome (15), however 4-HT binding stabilizes it (16). Also, human fibroblasts should not have estrogen receptor present, therefore any expression of estrogen receptor would be from 4-HT binding and stabilizing the estrogen receptor of ΔB-Raf-ER*. Stabilization of receptors causes dimerization and translocation into the nucleus, leading to increased B-Raf expression. To ensure that stabilization of the receptor does indeed lead to the activation of the MAPK/ERK pathway, we also blotted for downstream element of B-Raf, p-Erk. We used Erk as a loading control.

We rendered plates of almost confluent cells quiescent by serum starvation. For the first part of the experiment, we treated clones with increasing concentrations (0-100 nM) of 4-HT for 24 hours. We treated cells expressing mCherry with either 0 or 100 nM of 4-HT and used them as a control. For the second part of the experiment, we treated clones with 100 nM of 4-HT for increasing periods of time (0-24 hours). After exposure to 4-HT, we lysed cells with 1X Laemmli buffer. We ran the lysates on a Western blot and blotted with ERα, Erk and p-Erk antibodies. The Western blots are shown in Fig. 6, Fig. 7 whereas the levels of expression of ERα, Erk and p-Erk are shown in Table 1 and Table 2.

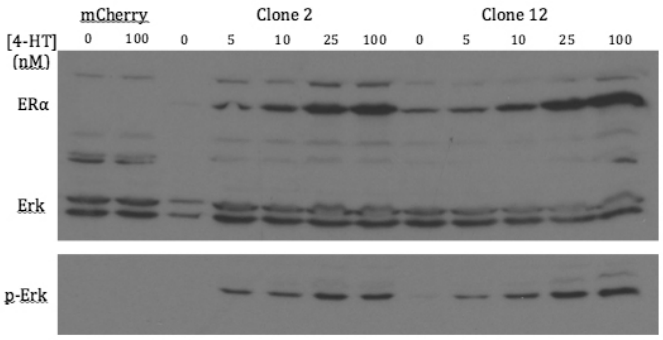

Fig. 6

ΔB-Raf-ER* signaling in HF-E1T cells. Effect of increasing concentration of 4-HT on protein expression. Almost confluent plates of mCherry cells and clones 2 and 12 were serum starved overnight. They were then treated with increasing concentrations of 4-HT for 24 hours. Cell lysates were prepared, and Western blotting assessed the levels of expression of ERα, Erk and p-Erk.

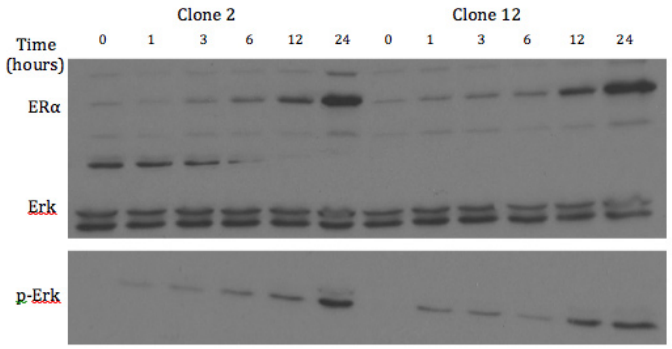

Fig. 7
ΔB-Raf-ER* signaling in HF-E1T cells. Effect of time of treatment to 4-HT on protein expression. Almost confluent plates of mCherry cells and clones 2 and 12 were serum starved overnight. They were then treated with increasing times of exposure to 100 nM of 4-HT. Cell lysates were prepared, and Western blotting assessed the levels of expression of ERα, Erk and p-Erk.

Cell Type	**mCherry**		**Clone 2**				
[4-HT]	*0 nM*	*100 nM*	*0 nM*	*5 nM*	*10 nM*	*25 nM*	*100 nM*
p-Erk Level	2367.39	2002.64	2703.39	14558.15	15365.56	24312.86	21386.27
			Clone 12				
p-Erk Level			2479.86	9367.56	15703.10	26386.98	29542.22
Cell Type	**mCherry**		**Clone 2**				
[4-HT]	*0 nM*	*100 nM*	*0 nM*	*5 nM*	*10 nM*	*25 nM*	*100 nM*
ERα Level	1109.08	890.64	1277.69	8893.81	14866.15	26636.51	30717.64
			Clone 12				
ERα Level			8647.74	10285.98	17220.81	30188.46	44964.61
Cell Type	**mCherry**		**Clone 2**				
[4-HT]	*0 nM*	*100 nM*	*0 nM*	*5 nM*	*10 nM*	*25 nM*	*100 nM*
Erk Level	29068.81	28656.10	11706.29	27977.05	28844.76	30007.51	27867.69
			Clone 12				
Erk Level			25207.34	26512.66	24335.22	24685.83	23928.51

Table 1
Calculated levels of expression of ERα, Erk and p-Erk for clones 2 and 12 treated with increasing concentrations of 4-HT for 24 hours.

	Clone 2					
Time	*0 hours*	*1 hours*	*3 hours*	*6 hours*	*12 hours*	*24 hours*
p-Erk Level	3823.91	5354.44	7099.05	9734.81	12945.10	20688.46
	Clone 12					
p-Erk Level	2432.15	6840.98	7162.39	3870.27	14199.56	26072.93
	Clone 2					
Time	*0 hours*	*1 hours*	*3 hours*	*6 hours*	*12 hours*	*24 hours*
ERα Level	4545.22	2719.74	4642.56	7067.86	12735.86	27392.69
	Clone 12					
ERα Level	2782.74	4048.61	4828.98	5454.74	14586.56	34587.29
	Clone 2					
Time	*0 hours*	*1 hours*	*3 hours*	*6 hours*	*12 hours*	*24 hours*
Erk Level	28091.69	26433.81	26837.44	27245.56	26734.39	24582.74
	Clone 12					
Erk Level	24596.98	24097.2	24936.81	23721.56	23599.98	22947.58

Table 2
Calculated levels of expression of ERα, Erk and p-Erk for clones 2 and 12 treated with increasing times of exposure to 100 nM of 4-HT.

From the first Western blot, we observe that increasing concentrations of 4-HT caused increased levels of the estrogen receptor and increased levels of p-Erk. We can observe that there are consistently higher levels of p-ERK and ERα for Clone 12 compared to clone 2. The similar levels of Erk present in each sample confirmed equal loading of the Western blots. From the second Western blot, we observe that increasing time of exposure to 4-HT caused increased levels of estrogen receptor and increased levels of p-Erk. We can observe that there are consistently higher levels of p-ERK and ERα for Clone 12 compared to clone 2. Again, the similar levels of Erk present in each sample confirmed equal loading of the Western blots.

Discussion

Virus infection of human fibroblast cells generated multiple clones, numbered 1-3, 6,7, and 9-12. We screened the clones for their ability to induce senescence through B-Raf signaling and their ability to remain growth arrested after the removal of 4-HT. Clones 2 and 12 were the most efficient clones at senescence induction and its maintenance. We measured the activity of the kinase cascade. ΔB-Raf-ER* showed increased activation with increased concentration or time of exposure to 4-HT for both clones. We eventually abandoned clone 12 because of its low cells counts, likely due to increased expression in the MAPK/ERK pathway leading to apoptosis. We can confirm this observation by looking at the increased levels of ERα and p-Erk of clone 12 compared to clone 2 in the Western Blots in Fig. 6, 7 and Tables 1 and 2.

The results obtained from the current experiment agree with the literature where constitutive expression of oncogenic Ras and Raf in cells elicits premature senescence in fibroblast cells(3, 4). Raf mediated senescent cells exhibited irreversible withdrawal from the cell cycle, elongated morphology, retention of viability, and the induction of senescent enzymatic marker β-galactosidase(4). All these characteristics were also observed in the current experiment, except that the activity of β-galactosidase was not tested, but likely to be present. The question still remains, how do cells achieve senescence, what proteins are involved in the process?

Through FACS, a tool used to identify cells in different stages of the cell cycle, previous work demonstrated that Raf mediated cell senescence arrested in G1 and G2/M(4). Arresting in these two stages of the cell cycle could suggest different proteins and mechanisms involved at each of these stages. Alternatively, it could also suggest the same protein involved in two different stages of the cell cycle. It would be intriguing to see if the HF-E1T immortalized cell line would exhibit similar properties and arrest in the same cell cycle stages.

Senescent cells are known to express elevated levels of p53, $p21^{Cip21}$, and $p16^{INK4a}$ (17, 18), but evidence suggests that the level and role in senescence these genes may play is still not well understood. In IMR-90 cells, a type of human lung fibroblast, Raf induced senescence did not correlate with induction of p53 or $p21^{Cip21}$, but rather with $p16^{INK4a}$ (4). On the other hand, ectopic expression of $p15^{INK4b}$, $p16^{INK4a}$, $p21^{Cip21}$ and $p27^{Kip1}$ elicited cell cycle arrest in TIG-3 human lung fibroblasts (19). A possible explanation for these results it that, different mechanisms may mediate oncogene-induced senescence in different cell lines.

Finally, much work has also been done on Ras, the upstream regulator of Raf proteins. Ras mediated OIS exhibits similar characteristics to the senescence induced by Raf but has a difference in morphology (20). Ras induced senescence is distinctive in that it has a flattened phenotype like non-senescent cells, as opposed to the elongated phenotype of that of Raf (20). The difference in morphology may be attributed to the additional cell signaling pathways Ras can regulate, such as those involving Rho GTPases. The difference in morphology could also suggest different mechanisms involved in their senescence. Other studies have also been conducted on MEK, the downstream substrate of Raf. MEK mediated OIS exhibits all the same characteristics as Raf mediated OIS including the elongated morphology (21). These observations would be expected as Raf directly activates MEK and has very few substrates (21).

The genes mentioned above in the discussion could all be part of the senescence mechanism; however the increased expression of these genes may at times be observed due to coincidence rather than by causation. In the locus coding for $p16^{INK4a}$, another protein known as $p19^{ARF}$ is also present (22). It has been proven that mice lacking $p19^{ARF}$ but have normal expression $p16^{INK4a}$ develop tumours (22). These results suggest that the elevated expression of $p16^{INK4a}$ observed in senescent human fibroblasts may be indication of correlation rather than the causation of senescence (4). It's possible that $p16^{INK4a}$ may have a role in tumour suppression, however its role in senescence is still not well understood.

Conducting a genetic screen involving the systematic interrogation of the human genome would avoid the problem of correlation and provide results based on causation since we would obtain a visible phenotype. We would also be able to screen thousands of genes at once rather than focus on the expression of specific genes. In a genetic screen conducted by Wajapeyee and al. on human fibroblasts and melanocytes, secreted protein IGFBP7 was identified as a major player in B-Raf oncogene induced senescence (14). However a paper published not long after contradicted this result and concluded that IGFBP7 was actually not required for B-Raf oncogene induced senescence (23). The explanation for this discrepancy was that the tissue culture conditions used in the original experiment allowed activated B-Raf to cause genetic changes. These genetic changes resulted in the selective outgrowth of antibiotic-resistant clones that had escaped oncogene-induced senescence. This scenario is unlikely to occur in our experiment, as our cells are less prone to escape senescence. Our screen for escape frequency of clone 2 did not yield an outgrowth

of a single cell colony. In another genetic screen conducted on epithelial cells, genes previously implicated in proliferative control such as PTEN were confirmed (24). In addition, new genes such as REST that is involved in the transcriptional repression were also identified (24).

For our experiment, we will be using barcoded, retroviral based short hairpin RNA (shRNA) library to enable stable gene knockdown. We will be able to systematically screen the human genome for genes whose loss of function will transform cells into an oncogenic state and bypass senescence. We propose a pooled screen paradigm where cells will be treated with shRNAs to knockdown genes. Cells with successful gene knockdown will be selected for and the ectopic expression of B-Raf will be upregulated to induce senescence. The cells with successful senescence evasion will have the barcode of the shRNA sequenced to determine the gene that was knocked down. There is the possibility that some cells with senescence evasion have more than one gene knocked down. In this case, we will sequence all the barcodes from the shRNAs and identify them. We will then treat senescent cells with the shRNAs individually to determine the gene causing senescence. The genetic screen we would conduct will likely first identify already defined tumour suppressors in the literature, but additionally it may identify novel genes previously undefined in the literature. The newly identified genes would provide novel targets for drug therapies and markers of tumorigenesis.

Acknowledgements

I'd like to thank Dr. David Dankort for giving the opportunity to apply my knowledge in a lab and to have this whole experience. Samantha Garnett, for her help and guidance from the beginning of the experiment to today. Thank you Angeline De Bruyns, Ben Geiling, Kendall Dutchak and Eve Bigras for showing me the way around the lab and answering all of my questions.

References

[1] Seger R, Krebs EG. The MAPK signaling cascade. FASEB journal : official publication of the Federation of American Societies for Experimental Biology. 1995;9(9):726-35.

[2] Mercer KE, Pritchard CA. Raf proteins and cancer: B-Raf is identified as a mutational target. Biochimica et biophysica acta. 2003;1653(1):25-40.

[3] Serrano M, Lin AW, McCurrach ME, Beach D, Lowe SW. Oncogenic ras provokes premature cell senescence associated with accumulation of p53 and p16INK4a. Cell. 1997;88(5):593-602.

[4] Zhu J, Woods D, McMahon M, Bishop JM. Senescence of human fibroblasts induced by oncogenic Raf. Genes & development. 1998;12(19):2997-3007.

[5] Bartkova J, Rezaei N, Liontos M, Karakaidos P, Kletsas D, Issaeva N, et al. Oncogene-induced senescence is part of the tumorigenesis barrier imposed by DNA damage checkpoints. Nature. 2006;444(7119):633-7.

[6] Dimri GP, Lee XH, Basile G, Acosta M, Scott C, Roskelley C, et al. A Biomarker That Identifies Senescent Human-Cells in Culture and in Aging Skin in-Vivo. Proceedings of the National Academy of Sciences of the United States of America. 1995;92(20):9363-7.

[7] Hayflick L, Moorhead PS. The serial cultivation of human diploid cell strains. Experimental cell research. 1961;25:585-621.

[8] Lees E. Cyclin dependent kinase regulation. Current opinion in cell biology. 1995;7(6):773-80.

[9] Fulda S. Evasion of apoptosis as a cellular stress response in cancer. International journal of cell biology. 2010;2010:370835.

[10] Wu X, Kemp B, Amos CI, Honn SE, Zhang W, Walsh GL, et al. Associations among telomerase activity, p53 protein overexpression, and genetic instability in lung cancer. British journal of cancer. 1999;80(3-4):453-7.

[11] Oldham SM, Clark GJ, Gangarosa LM, Coffey RJ, Jr., Der CJ. Activation of the Raf-1/MAP kinase cascade is not sufficient for Ras transformation of RIE-1 epithelial cells. Proceedings of the National Academy of Sciences of the United States of America. 1996;93(14):6924-8.

[12] Littlewood TD, Hancock DC, Danielian PS, Parker MG, Even GI. A Modified Estrogen-Receptor Ligand-Binding Domain as an Improved Switch for the Regulation of Heterologous Proteins. Nucleic acids research. 1995;23(10):1686-90.

[13] Geiling B, Vandal G, Posner AR, de Bruyns A, Dutchak KL, Garnett S, et al. A modular lentiviral and retroviral construction system to rapidly generate vectors for gene expression and gene knockdown in vitro and in vivo. PloS one. 2013;8(10):e76279.

[14] Wajapeyee N, Serra RW, Zhu X, Mahalingam M, Green MR. Oncogenic BRAF induces senescence and apoptosis through pathways mediated by the secreted protein IGFBP7. Cell. 2008;132(3):363-74.

[15] Nawaz Z, Lonard DM, Dennis AP, Smith CL, O'Malley BW. Proteasome-dependent degradation of the human estrogen receptor. Proceedings of the National Academy of Sciences of the United States of America. 1999;96(5):1858-62.

[16] Wijayaratne AL, Nagel SC, Paige LA, Christensen DJ, Norris JD, Fowlkes DM, et al. Comparative analyses of mechanistic differences among antiestrogens. Endocrinology. 1999;140(12):5828-40.

[17] Zindy F, Quelle DE, Roussel MF, Sherr CJ. Expression of the p16INK4a tumor suppressor versus other INK4 family members during mouse development and aging. Oncogene. 1997;15(2):203-11.

[18] Woods D, Parry D, Cherwinski H, Bosch E, Lees E, McMahon M. Raf-induced proliferation or cell cycle arrest is determined by the level of Raf activity with arrest mediated by p21(Cip1). Molecular and cellular biology. 1997;17(9):5598-611.

[19] McConnell BB, Starborg M, Brookes S, Peters G. Inhibitors of cyclin-dependent kinases induce features of replicative senescence in early passage human diploid fibroblasts. Current biology : CB. 1998;8(6):351-4.

[20] Thorburn J, McMahon M, Thorburn A. Raf-1 kinase activity is necessary and sufficient for gene expression changes but not sufficient for cellular morphology changes associated with cardiac myocyte hypertrophy. The Journal of biological chemistry. 1994;269(48):30580-6.

[21] Lin AW, Barradas M, Stone JC, van Aelst L, Serrano M, Lowe SW. Premature senescence involving p53 and p16 is activated in response to constitutive MEK/MAPK mitogenic signaling. Genes & development. 1998;12(19):3008-19.

[22] Kamijo T, Zindy F, Roussel MF, Quelle DE, Downing JR, Ashmun RA, et al. Tumor suppression at the mouse INK4a locus mediated by the alternative reading frame product p19ARF. Cell. 1997;91(5):649-59.

[23] Scurr LL, Pupo GM, Becker TM, Lai K, Schrama D, Haferkamp S, et al. IGFBP7 is not required for B-RAF-induced melanocyte senescence. Cell. 2010;141(4):717-27.

[24] Westbrook TF, Martin ES, Schlabach MR, Leng Y, Liang AC, Feng B, et al. A genetic screen for candidate tumor suppressors identifies REST. Cell. 2005;121(6):837-48.

REVIEW ARTICLE

Neuroplasticity and Post-Synaptic Rebound-Induced Spiking at Purkinje Cell-Deep Cerebellar Nuclei Synapses

Jenna Hotton[1]*

[1] Department of Biology, McGill University, Montreal QC, Canada

*Email Correspondence:
jenna.hotton@mail.mcgill.ca

Abstract

Background: Within the cerebellum white matter are located four pairs of nuclei, collectively known as the deep cerebellar nuclei (DCN) (1). In the cerebellum, signal integration from pre-cerebellar structures via excitatory parallel fibers and climbing fibers in the cerebellar cortex occurs in GABAergic Purkinje cells (PC) (2). The main target of these PC cells is the DCN (2) and approximately 85% of GABAergic input on the DCN is from PCs (3). Furthermore, PCs outnumber DCN neurons (26:1) (2). Therefore, despite receiving substantial inhibition from Purkinje cells, DCN neurons are still active at rest showing regular spiking or spontaneous bursts (4). DCN neurons fire spontaneously at approximately 10-50 Hz (5). Given this unique anatomy of PC-DCN synapses, characterization of this synaptic circuit is important in understanding the overall role of the DCN in the brain.

Methods: The findings of 28 studies, including a few reviews, are reported in this paper. Studies selected focused principally on characterization of DCN circuitry properties and the role these properties have in the functioning of the DCN. Most studies employed in vivo and/or in vitro cellular recordings in rodents, among other models. Studies ranged from 1984 to 2013.

Summary: This review outlines current findings on the forms of plasticity found in the DCN, the function of the DCN and the connections between the DCN and other brain regions. In short, neurons in the DCN demonstrate both synaptic and non-synaptic plasticity. Cerebellar involvement in motor activity has been extensively studied therefore, not surprisingly; DCN neurons form connections with the motor cortex but also the prefrontal cortex. PC input on the DCN influences spike rate and timing through fluctuations in PC synchrony, and rebound depolarization.

Introduction

Nestled within the cerebellum are four pairs of nuclei, known as the deep cerebellar nuclei (DCN) (2). The cerebellum, in general, receives input from pre-cerebellar regions (2). This information is conveyed to the cerebellar cortex via excitatory MF and CF (2). Within the cerebellar cortex, these inputs are processed by the Purkinje cells (PC). Projections from PCs are the sole output of the cerebellar cortex. Notably, the DCN receive 85% of its inhibitory input from PCs (3). Furthermore, the DCN also receive excitatory input from MF and CF collaterals (2). Purkinje cells do not innervate the DCN in a uniform pattern (2). Of the types of neurons in the DCN, four are projection neurons (large and small) and two are interneurons (4). Large glutamatergic neurons have excitatory projections to extracerebellar non-olivary nuclei, small/medium nucleo-olivary GABAergic neurons have inhibitory projections to the inferior olive, large GABAergic and glycinergic neurons have inhibitory role in local circuitry and other glycinergic neurons have inhibitory feedback to cortex and feedforward to the brainstem nuclei (4,5). In turn, the DCN provide excitatory and inhibitory output to other brain regions such as the brainstem, thalamus and inferior olive (2). Not surprisingly, the DCN have connections to the motor cortex. However, connections between the prefrontal cortex and the DCN suggest that the DCN may also function within a wider behavioural context. While the anatomy and circuitry of the cerebellar cortex is well-studied, the circuitry of the DCN has received less attention. Nowadays, the DCN are often studied with very little differentiation between the individual nuclei and their circuitry within. More research must be done to map the connections within the DCN and the roles of the individual deep cerebellar nuclei. This paper aims to review current research on the circuitry and function of the DCN, with an emphasis on the PC-DCN synapse and plasticity. Briefly, the DCN has shown both changes in synaptic strength and intrinsic excitability mediated by changes in Ca^{2+} with PC synchrony, as well as rebound-induced spiking being proposed to influence DCN activity.

Neuroplasticity

Neuroplasticity can either return neurons to homeostasis or form a new set point such as non-homeostatic (6). Neuroplasticity in the DCN has mainly been studied in relation to its putative role in motor learning. Aizenman and Linden (7), who have studied both use-dependent synaptic plasticity and non-synaptic plasticity, propose that both forms of plasticity may work together to provide "a flexible and informationally rich engram" (7). An engram refers to the hypothetical representation of memory traces in the brain. In general, the DCN show bidirectional long-term synaptic plasticity, short-term synaptic depression and increases in intrinsic excitability.

Neurons in the DCN show bidirectional long-term synaptic plasticity

The PC-DCN synapses demonstrate long-term synaptic or use-dependent plasticity (8). This form of plasticity can cause a bidirectional change in synaptic strength – either enhancing the synapse's strength of depressing it. This bidirectional synaptic plasticity is induced by changes in post-synaptic Ca^{2+} influxes. Large Ca^{2+} transients induce long-term potentiation (LTP) and small transients induce long-term depression (LTD) (9).

Bidirectional synaptic plasticity at PC-DCN synapses has been studied by Aizenman *et al.* (9). They concluded, using intracellular recordings from the DCN of rats, that bidirectional long-term synaptic plasticity does exist at inhibitory synapses due to IPSP triggered Ca^{2+} influxes (9). Their results indicated that a burst of short, high frequency (10 pulses at 100 Hz) IPSPs applied at resting potential generated large Ca^{2+} transients - thereby inducing LTP for more than 20 minutes (9). Hyperpolarizing pulses also triggered LTP and generated large Ca^{2+} transients (9). However, when a burst of IPSPs (10 pulses at 100 Hz) is applied at a tonic hyperpolarized potential (-67 mV), this induces LTD with reduced Ca^{2+} transients (9). A burst of short, high frequency IPSPs at resting potential or at hyperpolarized potential also generated sizable rebound-induced spiking or limited rebound-induced spiking respectively (9). Rebound-induced spiking is a burst of spikes which are elicited at a depolarizing membrane potential following a release from inhibition (10). This long-term bidirectional synaptic plasticity is mediated in part by Ca^{2+} channels: blocking of Na^{+} spikes (using QX-314) also induces LTD with limited rebound spiking, (9) thereby showing that rebound is not mediated by Na^{+} channels. The contribution of Ca^{2+} influxes during rebound has been further studied: Dendrites in the DCN are capable of calcium-based excitation and dendritic calcium transients require T-type Ca^{2+} channels but not sodium channels (11). Both hyperpolarizing pulses and IPSPs (through inhibition of action potentials) induce a hyperpolarizing membrane potential. Furthermore, it is thought that rebound spiking induces the Ca^{2+} transients in DCN neurons. The amount of rebound spiking thereby determines whether LTP or LTD will be evoked, that is, in which 'direction' the change in synaptic strength will be (9).

Following Aizenman *et al.*'s (9) conclusion that IPSPs and hyperpolarization can elicit rebound-induced spiking, Aizenman and Linden (10) studied the conditions necessary to induce rebound in rats (10). Results indicated that IPSPs are more efficient at inducing rebound spiking than hyperpolarizing bursts (10). Rebound-induced spiking is evoked following a release from inhibition. Therefore, the more depolarization, the stronger rebound activation, with a peak activation at membrane potentials of -60 to -70 mV (this is within the low threshold, voltage-gated T-type Ca^{2+} channel's activation range (10). This provides further evidence that rebound-induced spiking is being mediated by Ca^{2+} channels, specifically T-type channels (9,10) being de-inactivated after hyperpolarization (9). T-type Ca^{2+} channels are involved in all forms of rebound activity exhibited in DCN cells (12). Furthermore, rebound-induced spiking is blocked in DCN cells when a T-type Ca^{2+} antagonist, mibefradil is applied (13) and rebound evoked by synaptic inhibitory input or current injection is suppressed by the T-type Ca^{2+} antagonist, TTA-P2 (12).

Nonetheless, Ca^{2+} transients can be mediated by more than just T-type Ca^{2+} channels. Plasticity may also depend upon NMDA receptors (6), as moderate or large Ca^{2+} influxes via activation of NMDA receptors as well as or L-type Ca^{2+} channels can also evoke cell-wide LTD or LTP of IPSC. L-type Ca^{2+} channels also play a role in eliciting LTP at MF-DCN synapses excitatory post-synaptic currents (EPSCs) (14). Hyperpolarization and disinhibition following high frequency excitation are necessary to generate LTP of EPSPs in DCN cells (15). Each of the above steps requires calcium regulation: Excitation activates calcium-dependent calcineurin while inhibition decreases L-type Ca^{2+} influxes (14). Lastly, disinhibition allows for calcium-activated α-CAMKII to triggers potentiation following the release from inhibition (14).

Neurons in the DCN show short-term depression

Short-term depression induces a less sustained decrease in synaptic strength than long-term depression. Because of the high PC to DCN convergence ratio, DCN cells are continuously bombarded with inhibitory input from PC neurons yet still have a constant basal firing rate (16). Short-term depression of PC-DCN synapses may therefore allow for such basal firing to occur in the DCN.

In a study by Telgkamp and Raman (16) identified two stages of short-term depression: A fast, frequency dependent stage and a slow, frequency independent stage (16). As a consequence, IPSC recovery from the first stage of depression is more rapid (~100 millisecond) than recovery from the second stage of depression (~10 second) (16). Increases in presynaptic activity therefore lead to "steady-state"-depressed IPSCs, most probably due to IPSCs never fully recovering from the second, slower stage of depression between the applications of high frequency stimuli (16). On the other hand, decreased presynaptic activity leads to larger IPSC that fully recover between applied stimuli (16). Inhibitory post-synaptic currents evoked at the sponta-

neous firing rate of PCs depress by 60% (16).

In all, the spontaneous activity of PC activity is thought to lead to short-term depression at the PC-DCN synapses allowing for basal DCN activity despite the high convergence of inhibitory PC cells (16). In this sense, short-term synaptic depression at the PC-DCN synapse functions to moderate inhibition of DCN cells (16). Such depression at the PC-DCN synapses occurs at varying firing frequencies and persists through glutamate blocking (MCPG blocker) but not through GABA blocking (SR95531 blocker) (16).

Neurons in the DCN show non-synaptic plasticity

Non-synaptic plasticity does not modify the strength of the synapse but induces changes in intrinsic excitability. Changes in the intrinsic excitability in DCN excitatory cells can manifest as an increase in firing rate or a decrease in intrinsic spike threshold (7). Tetanization protocols, NMDAR activation and depolarizing currents can all induce intrinsic excitability in DCN neurons (6,7,15).

In one study conducted by Aizenman and Linden (2000) (7), a tetanization protocol was applied. In their study, a tetanus of 10 high frequency bursts of 10 pulses at 100 Hz was applied at a frequency of 4 Hz (7). Results indicate that tetanization lead to sustained increases in intrinsic excitability of DCN cells compared to cells that did not receive a tetanus (7). Similarly, activation of NMDA receptors also lead to a sustained increase in intrinsic excitability of DCN cells recorded from rat cerebellar slices (7). Additionally, when cells are bathed in NMDA antagonist, D-AP5, no increase in spiking occurs (7), further supporting the role of NMDA receptors in intrinsic excitability. In both tetanization and NMDA receptor activation paradigms, Ca^{2+} is required. Ca^{2+} influxes can be achieved through depolarizing currents leading to Ca2+ voltage-gated calcium channel activation or Ca^{2+} coming into the cell via NMDA receptors (7). These calcium influxes might be a result of "burst-pause" input from PCs on DCN neurons (7).

Neuron spine index is correlated with the changes in intrinsic excitability in DCN cells

A study of neuronal morphology of mostly large and multipolar DCN projection neurons *in vivo* in rats between 6 to 9 post-natal days-old (P6-9) and P13-16 demonstrated a correlation between spine index (a measure of how spiny and sinuous dendrites are) and intrinsic excitability properties (8). An increase in spine index is correlated with a decrease in basal firing rate, larger after hyperpolarizing potentials (AHP) and a more negative resting membrane potential (8). Intrinsic excitability also increases with age. At P6-9 and P13-16, large DCN projection neurons have similar morphology, but cells at P6-9 show less intrinsic excitability (8). Furthermore, as Aizenman *et al.* (8) report, dendritic morphology of DCN projection neurons mature during pre-natal development and PCs innervate DCN cells in late pre-natal development (8). However, intrinsic excitability properties only mature later in post-natal development (8).

Neuroplasticity and Eye-Blink Conditioning

In general, long-term bidirectional synaptic plasticity is involved in associative learning (17). The role of neuroplasticity in the DCN has been studied in relation to eye-blink conditioning (EBC) (17,18,19). EBC is a form of classical conditioning of the eyelid or nictitating membrane (18) which involves the association of an unconditioned stimulus (US) and a conditioned stimulus (CS) (19). Naïve animals will blink in reaction to an US (e.g. puff of air) thus eliciting an unconditioned response (UR) (19). On the other hand, trained animals will also blink in reaction to a CS (e.g. tone) thus eliciting a response similar to the US known as a conditioned response (CR) (19). It has been proposed that MF and CF of the cerebellum convey information of the CS and US respectively (17). An early study by McCormick and Thompson (18) studied the relative contribution of the cerebellar cortex and the DCN, in particular the ipsilateral lateral cerebellum including the dentate and interpositus nuclei, in EBC. In this study, the dentate-interpositus region was shown to be necessary for learning the CR (18). Lesions in the dentate-interpositus region abolish CR while lesions in the cortex failed to abolish CR (18). This suggests that the lesions disrupt the output of the dentate-interpositus nuclei rather than the connection between the cortex and this DCN region (18). Furthermore, McCormick and Thompson proposed that these results suggest that plasticity necessary for EBC learning is restricted to the dentate-interpositus region (18). Chen *et al.* (17) reported similar results with lesions in the interpositus nucleus abolishing EBC learning (17). However, the cerebellar cortex is nonetheless involved in EBC. In a study by Chen *et al.* (17), because of the unique anatomy of the PC-DCN synapses, PC mutants mice have no neural output from the cortex to the DCN (17). These mutants showed impaired learning of CR compared to wild-types but with further training, were able to achieve minimal EBC (17), therefore the cerebellar cortex is also required for normal EBC. Various forms of synaptic plasticity may be involved in EBC (19). For example, Kim and Thompson (19) demonstrated that EBC impairment correlates with LTD at PF-PC synapses.

Function of the DCN

In general, the role of the cerebellum in motor activity and learning is well-studied. Both inhibitory and excitatory inputs from the cerebellar cortex influence DCN output and subsequently its function. In an early study by Llinas and Muhlethaler (20), intracellular recordings in guinea pigs demonstrated that DCN neurons generated EPSPs in response to input from CF collaterals, originated from the inferior olive, and MF collaterals, originated from precerebellar nuclei (2,20). DCN neurons also generate IPSPs in response to PC input (20), which can These PCs convey information via spike frequency alternations

and spike timing (5). Subsequently, the DCN provide excitatory output to the brainstem and thalamus, as well as inhibitory output to the inferior olive (2). Since PCs influence DCN activity, they subsequently affect motor activity. Graded PC activation leads to graded inhibition in DCN (21).

Influence of PC Synchrony on DCN

PCs convey information through inhibitory input from the cerebellar cortex to the DCN. Synchronized PC firing influences both spike rate and timing of DCN cells (22). An increase in PC synchrony leads to an increase in DCN spike rate (22). Synchrony of CF evoked spikes in PCs is due to gap junctions, which allow CFs that innervate separate PCs to be "electronically coupled" (5). PC synchrony plays a crucial role in information processing. Blocking olivary neuron coupling disrupts synchrony and rebound activity, leading to impaired and ill-timed reflex movements in some cases (5).

Furthermore, pauses in PC firing elicit DCN spikes with higher PC synchrony leading to more precisely timed DCN responses to inhibitory input (22). Spiking in PCs may also be generated intrinsically (23). Each of these spikes individually has a minimal influence on the DCN; however, due to high PC-DCN convergence, synchronized spikes can influence DCN firing via feed-forward inhibition (5).

Along with conveying information via spike rate, DCN neurons are thought to be able to transmit the timing of synchronized PC neurons spikes (24). Person and Raman (24) demonstrated that *in vitro*, desynchronized IPSPs which mimics PC input generate no spiking in DCN; while synchronized IPSPs do (24). As a consequence, DCN neurons fire spikes in-between the synchronized inhibitory PC input, that is, the DCN neurons fire spikes that are time-locked (24). Such as time-locked computational model may provide a model to describe the coordination of movement by the cerebellum, however, Medina (25) debates the generality of these results under physiological in vivo conditions. Medina (25) points out that further study is necessary to determine how the DCN balances both the synchronized, as Person and Raman (24) proposed, inhibitory PC input and excitatory MF and CF input (25). Khodakhah (25) also questions whether complete synchronization of two PC is probable and proposed optogenetic *in vivo* studies to increase specificity of PC activation to further test the time-locking model. Both Medina and Khodakhah (25) point out that the current model of cerebellar control of movement, rate code (an averaging of the rate of firing frequency to convey information) has not been refuted and thus time-locking may work in conjunction with a rate code computational model (25). In vivo, desynchronized IPSPs inhibit firing in DCN while synchronized IPSPs causes an increase in DCN spiking rate but only when performed at near physiological temperature (36 °C) (24). After synchronized IPSPs, there were short latency, well-timed action potentials generated because of the high PC-DCN convergence ratio (40:1), high post-inhibitory intrinsic firing rate (~90 Hz) and rapid IPSC decay (τ_{decay}=2.5 ms is significantly briefer than that at 22°C) (24). Faster IPSC decay allows for full decay of the inhibitory current between stimuli (24). Phase-locking of spikes to synchronized input also occurs in the DCN (24). DCN cells' spiking peaks at intervals corresponding to the intervallic generation of synchronized IPSPs allowing for the DCN to encode temporal information (24). As a consequence, faster decay periods would lead to more decay of IPSCs which may contribute to a fuller recovery from the second, slower state of short-term depression (16).

Influence of Rebound Activity on DCN

Rebound activity occurs following release of DCN cells from PC-generated IPSPs. Furthermore, rebound-induced spiking follows the offset of PC inhibition and not the onset (21). The release of this inhibitory input leads to an increase in firing (5,21). Mechanistically, rebound spiking is due to the opening of low-threshold, voltage-gated Ca^{2+} channels (10). Ca^{2+} channels de-inactivate with hyperpolarization and open with the return to a resting potential (20).

Synchrony of PC firing has an influence on generating rebound activity in the DCN. When individual PC neurons fire spikes together, there is both an increase in synchrony and an increase in the probability of eliciting rebound activity due to a decrease in PC background input (5,22). Computational models have postulated that rebound activity functions to trigger motor activity (22). GABAergic neurons in the DCN demonstrate rebound activity, which acts in an inhibitory feedback loop to the inferior olive (5). Non-GABAergic DCN neurons also demonstrate rebound activity which may act to influence motor and premotor areas (5).

A single, individual IPSP provides a small effect on the DCN (26). Therefore, concerted modulation from PC would be necessary to evoke rebound activity *in vivo* (26). With low PC synchrony, DCN cells are subject to a tonic inhibitory input (26). However, with synchrony of PC cells as discussed above, DCN cells produce large compound IPSP and rebound activity (26). Witter *et al.*'s (21) optogenetic study allowed for the synchronized activation of only PCs. In this method, a variant of the channelrhodopsin-2 is expressed in PCs in mice thus allowing for light to activate PCs specifically (21). Results confirmed that strong synchronized stimulus of PC led to more precisely timed rebound in the DCN (21). With this, the end of synchronized PC corresponded to movement in awake mice (21). Witter *et al.* (21) provide a PC control model of motor activity. In this model, a PC network is activated leading to graded control of rebound activity in the DCN which ultimately leads to the onset of motor activity (21).

The implications of PC activity triggering rebound-induced firing requires more study considering the majority of research (e.g. 9,10) has been conducted *in vitro*. As mentioned, a recent 2013 study by Witter *et al.* circumvented one limitation of electrophysiology, which is ensuring activation of specific cell types by using an optogenetic method (21). Using this method, Witter *et al.* (21) concluded that re-

rebound firing followed the offset of PCs activity and that even weak activation of PCs led to rebound *in vivo* (21). Nonetheless, further research is necessary as the exact role of rebound-induced spiking *in vivo* remains (13).

Connections to the prefrontal cortex

The cerebellum is known to be involved in motor activity, particularly motor learning (2). However, connections between the DCN and other physiological regions extend beyond motor function (27). While cerebellar involvement in motor activity and motor disorders has been well-studied, recent studies also indicate the DCN is involved in prefrontal activity. For example, multi-synaptic pathways have been found between the interpositus nucleus in rodents (equivalent to the fused emboliform and globose nuclei in humans), and the motor cortex and prefrontal cortex (27). Labelling neurons in the prefrontal cortex, area 46 and the motor area (M1) with rabies virus demonstrated that the interpositus nucleus has synaptic pathways to both the prefrontal cortex and the motor cortex (27). Neurons labelled from M1 were found in the dorsal portion of the posterior interpositus nuclei, in the anterior interpositus nucleus and in the dorsal portion of the dentate nucleus (27). On the other hand, neurons labelled from area 46 were found in the ventral portion of the posterior interpositus nucleus and in the ventral portion of the dentate nucleus (27). Moreover, the PCs from the C2 cerebellar cortex zone were found to project to the posterior interpositus nucleus, while PCs from the C1/C3 zones project to the anterior interpositus nucleus (27). Therefore, there are separate cerebellar output pathways to the prefrontal cortex and the motor cortex in the interpositus nucleus and the dentate nucleus (27).

Conclusions

The DCN receives excitatory input from MF and CF, and inhibitory input from the cerebellar cortex via PCs. Both synaptic and non-synaptic plasticity has been shown to occur in the DCN. For example, long-term synaptic changes occur at the inhibitory PC-DCN synapses and at excitatory PF-DCN synapses. Rebound-induced spiking is thought to mediate Ca^{2+} influxes which dictate whether long-term plasticity will involve an increase in synaptic strength or a decrease in synaptic strength. Short-term depression is also seen in DCN cells and can be broken down into two stages. Due to high PC inhibitory input on the DCN, spontaneous PC firing is thought to evoke short-term depression which allows for DCN cells to demonstrate basal firing. Furthermore, non-synaptic changes in large DCN projection neurons include changes in intrinsic excitability which correlates with dendritic spine index. Functionally, PC synchrony and IPSP-driven rebounds have been postulated to influence DCN function although the exact role that PC synchrony and rebound play is debated. PC synchrony may function to provide concerted PC firing on the DCN. The DCN firing has shown time-locking and phase-locking to synchronized PC firing which may allow for the DCN to convey temporal information. In addition to bidirectional plasticity, rebound may function to trigger motor activity. The cerebellum's involvement in motor activity has been extensively studied. The importance of the DCN in motor activity is demonstrated with congenital diseases which include DCN pathologies such as dentate nucleus atrophy and symptoms including a lack of coordination of movements, difficulties swallowing and difficulties articulating speech (28). However, the DCN also shows synaptic pathways to prefrontal cortex regions.

Acknowledgements

Many thanks to Alanna Watt for her guidance and the opportunity to undertake this research. Also, thanks to Sriram Jayabal, Oliver Russell and Ahmed Hamam for their direction and feedback.

References

[1] Crossman AR, Neary D. Neuroanatomy. Spain: Elsevier; 2005. p. 115-121.

[2] Uusisaari M, De Schutter E. The mysterious microcircuitry of the cerebellar nuclei. The Journal of physiology. 2011;589(Pt 14):3441-57.

[3] Garin N, Escher G. The development of inhibitory synaptic specializations in the mouse deep cerebellar nuclei. Neuroscience. 2001;105(2):431-41.

[4] Uusisaari MY, Knöpfel. Neurons in the deep cerebellar nuclei. In: Manta M, Gruol DL, Schmahmann JD, Koibuchi N, Rossi F, editors. Handbook of the Cerebellum and Cerebellar Disorders. New York: Springer; 2013. p. 1101-1110.

[5] De Zeeuw CI, Hoebeek FE, Bosman LW, Schonewille M, Witter L, Koekkoek SK. Spatiotemporal firing patterns in the cerebellum. Nature reviews Neuroscience. 2011;12(6):327-44.

[6] Zheng N, Raman IM. Synaptic inhibition, excitation, and plasticity in neurons of the cerebellar nuclei. Cerebellum. 2010;9(1):56-66.

[7] Aizenman CD, Linden DJ. Rapid, synaptically driven increases in the intrinsic excitability of cerebellar deep nuclear neurons. Nature neuroscience. 2000;3(2):109-11.

[8] Aizenman CD, Huang EJ, Linden DJ. Morphological correlates of intrinsic electrical excitability in neurons of the deep cerebellar nuclei. Journal of neurophysiology. 2003;89(4):1738-47.

[9] Aizenman CD, Manis PB, Linden DJ. Polarity of long-term synaptic gain change is related to postsynaptic spike firing at a cerebellar inhibitory synapse. Neuron. 1998;21(4):827-35.

[10] Aizenman CD, Linden DJ. Regulation of the rebound depolarization and spontaneous firing patterns of deep nuclear neurons in slices of rat cerebellum. Journal of neurophysiology. 1999;82(4):1697-709.

[11] Schneider ER, Civillico EF, Wang SS. Calcium-based dendritic excitability and its regulation in the deep cerebellar nuclei. Journal of neurophysiology. 2013;109(9):2282-92.

[12] Boehme R, Uebele VN, Renger JJ, Pedroarena C. Rebound excitation triggered by synaptic inhibition in cerebellar nuclear neurons is suppressed by selective T-type calcium channel block. Journal of neurophysiology. 2011;106(5):2653-61.

[13] Alvina K, Ellis-Davies G, Khodakhah K. T-type calcium channels mediate rebound firing in intact deep cerebellar neurons. Neuroscience. 2009;158(2):635-41.

[14] Person AL, Raman IM. Deactivation of L-type Ca current by inhibition controls LTP at excitatory synapses in the cerebellar nuclei. Neuron. 2010;66(4):550-9.

[15] Pugh JR, Raman IM. Potentiation of mossy fiber EPSCs in the cerebellar nuclei by NMDA receptor activation followed by postinhibitory rebound current. Neuron. 2006;51(1):113-23.

[16] Telgkamp P, Raman IM. Depression of inhibitory synaptic transmission between Purkinje cells and neurons of the cerebellar nuclei. The Journal of neuroscience : the official journal of the Society for Neuroscience. 2002;22(19):8447-57.

[17] Chen L, Bao S, Lockard JM, Kim JK, Thompson RF. Impaired classical eyeblink conditioning in cerebellar-lesioned and Purkinje cell degeneration (pcd) mutant mice. The Journal of neuroscience : the official journal of the Society for Neuroscience. 1996;16(8):2829-38.

[18] McCormick DA, Thompson RF. Cerebellum: essential involvement in the classically conditioned eyelid response. Science. 1984;223(4633):296-9.

[19] Kim JJ, Thompson RF. Cerebellar circuits and synaptic mechanisms involved in classical eyeblink conditioning. Trends in neurosciences. 1997;20(4):177-81.

[20] Llinas R, Muhlethaler M. Electrophysiology of guinea-pig cerebellar nuclear cells in the in vitro brain stem-cerebellar preparation. The Journal of physiology. 1988;404:241-58.

[21] Witter L, Canto CB, Hoogland TM, de Gruijl JR, De Zeeuw CI. Strength and timing of motor responses mediated by rebound firing in the cerebellar nuclei after Purkinje cell activation. Frontiers in neural circuits. 2013;7:133.

[22] Jaeger D. Mini-review: synaptic integration in the cerebellar nuclei--perspectives from dynamic clamp and computer simulation studies. Cerebellum. 2011;10(4):659-66.

[23] Person AL, Raman IM. Synchrony and neural coding in cerebellar circuits. Frontiers in neural circuits. 2012;6:97.

[24] Person AL, Raman IM. Purkinje neuron synchrony elicits time-locked spiking in the cerebellar nuclei. Nature. 2012;481(7382):502-5.

[25] Medina JF, Khodakhah K. Neuroscience: Spikes timed through inhibition. Nature. 2012;481(7382):446-7.

[26] Bengtsson F, Ekerot CF, Jorntell H. In vivo analysis of inhibitory synaptic inputs and rebounds in deep cerebellar nuclear neurons. PloS one. 2011;6(4):e18822.

[27] Lu X, Miyachi S, Takada M. Anatomical evidence for the involvement of medial cerebellar output from the interpositus nuclei in cognitive functions. Proceedings of the National Academy of Sciences of the United States of America. 2012;109(46):18980-4.

[28] Koeppen AH, Davis AN, Morral JA. The cerebellar component of Friedreich's ataxia. Acta neuropathologica. 2011;122(3):323-30.

REVIEW ARTICLE

Human Health and the Microbiota: Interactions Between Gut Microbes, Hygiene, and The Immune System

Simon Fukada[1]*

[1] Department of Biology and Technology Mount Royal University, Calgary, Alberta, Canada

*Email Correspondence:
Sfuka591@mtroyal.ca

Keywords:
Helper T cell (Th): *Type of lymphocyte that via cytokines activates parts of adaptive immune system*
Cytokine: *proteins secreted by immune cells*
Interleukin (IL): *Type of Cytokine*
T regulatory cell (Treg): *Type of T cell which regulate immune responses*
Xenobiotics: *unnatural substance found in an organism*
Eosinophil: *Type of immune cell that targets parasites and contributes to allergic disease*
Dendritic Cells: *Antigen presenting cell*
Antigens: *Substance that may induce an immune response*

Abstract

Background: In the past, much of the scientific research on microbes focused on mechanisms of infection and disease. This was not in vain, as we gained valuable knowledge about our immune system, as well as the ability to develop vaccines and antibiotics. However, the relationship between humans and microbes is complex. These species have been co-evolving since multicellular organisms evolved on Earth.

Summary: Recently, it is beginning to be appreciated that the majority of relationships between humans and microbes are beneficial. From this follows an understanding that beneficial microbes are vital to the normal physiological development of our gut and immune system. This beneficial relationship between the human host and the multitude of microbial communities is well established. However, currently in the developed world epidemiological studies are showing dramatic increases in autoimmunity, allergies, and obesity. It is thus suggested that within westernized societies hygiene is altering the relationship between the gut and the human host in a way that makes humans susceptible to conditions not seen in less developed countries. This understanding advanced the "hygiene hypothesis," and more recently the, "old friends hypothesis" and "disappearing microbiota hypothesis" as possible explanations for the observed epidemiological phenomena. What follows is a review of the relationship between gut microbes and the host's immune system, with a focus on how hygiene (antibiotics, chlorination of water, etc.) is beginning to alter this relationship. This review concludes that a further understanding of how hygiene affects the relationship between humans and microbes will be crucial for developing effective therapies considerate of our microbial friends.

Introduction

Bacterial life inhabited earth billions of years before humans evolved. Therefore, it is well accepted that during the evolution of complex multi-cellular organisms, the microbial world played a role in influencing the structure and function of humans (1,2). This proposition is further supported by the evidence that there are an order of magnitude more microbial cells than somatic cells in and on the human body (3,4). For these reasons, it is common to view the relationship between the host and most microbes as mutually symbiotic (2,5,6). The recognized ecologic definition of symbiosis put forth by Anton de Bary is a prolonged association between two or more organisms of different species. Mutualistic if both organism benefit and parasitic

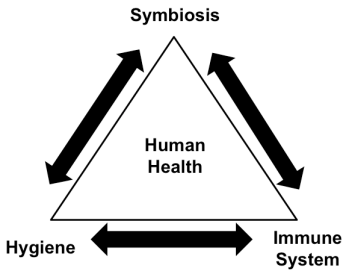

Fig. 1
This review will explore how the symbiotic microbes in our gut, hygiene (e.g., increased use of hand sanitizer, cleaning products, antibiotics and vaccinations), and the immune system interact with each other to contribute to human health.

if one is harmed while the other benefits. The relationship is mutually symbiotic in the sense that the microbiota access nutrients not attainable through host digestive mechanisms and help to guide the proper development of the host's immune system (2,3,4,5). In return the collaborating microbiota gain a safe, nutrient rich ecosystem (2).

Much of the microbiota that consists of bacteria, viruses, fungi, and other microeukaryotes live symbiotically within the human gastrointestinal tract (2,3,5). Thus, the gut serves as a useful setting to understand the benefits of this symbiotic relationship. In order to maintain this safe environment it is likely that the gut microbiota evolved to function closely with our own immune system, which would selectively destroy pathogenic agents and maintain the non-pathogenic populations (2).

Additionally, the gut microbiota play a vital role in immune homeostasis, or the maintenance of a stable immune system that neither overreacts or is too passive (5). However, this cooperation between species can be delicate due to the extreme microbial load present in the gut. The massive amount of microbes is a constant threat to the host systemically (7). If a usually symbiotic microbe's cost of cooperating becomes higher than the benefit it receives from the host, it has the potential to become pathogenic and invade systemically (7). Thus, those with immunodeficient disorders are at risk of infection from usually symbiotic bacteria, such as, *Enterococcus faecalis* and *Bacteroides fragilis* (7). For this reason the immune system must be able to maintain the balance of many different microbes while not knocking them out completely (7). The responsibility to differentiate between pathogens and commensal microbes, and to organize and maintain the location, in which these microbes inhabit their host, falls to the host's immune system (8, 9). The innate immune system seems to be primarily responsible for this intricate control of the mucosal environment (9). It must both protect against many pathogens as well as cooperate with innumerable amounts of symbionts. It accomplishes this by isolating all the microbes to specific locations within the host, as the symbiotic bacteria are often only symbiotic in the location in which they harbor, such as the gut, vagina, or skin to name a few (10). The innate immune system performs this task by sampling at the molecular level and can be induced by the components of microbial cell walls alone (11). For example, lipopolysaccharides, and peptidoglycans or microbial-associated molecular patterns (MAMPS), are ligands for pattern recognition receptors (PRR) on innate immune cells, such as, macrophages, and include tole-like receptors and mannose receptors (9, 11, 12, 13). More specifically gram-positive bacteria express lipopolysaccharides, and gram negative bacteria express teichoic acids (9). Through the recognition of specific MAMPs it is possible for the innate defence to differentiate between friendly MAMPs (symbionts) and pathogenic MAMPs or PAMPs (Pathogen associated molecular patterns) (9). If cells of the innate immune system (Antigen presenting cells) are activated via MAMPs interacting with PRRs, it is possible for an adaptive immune response to be activated (9).

Therefore, understanding the symbiotic relationship that the immune system shares with the microbiota may be a powerful tool to understand and improve human health. However, this relationship can be frustrated and strengthened with the addition of hygiene (Increased use of hand sanitizers, cleaning products, antibiotics etc.). This review will begin with an overview of the relationship between the host and its symbiotic microbes and conclude with a discussion on how hygiene fits into this relationship.

Evidence for symbiosis

The 20th century focus on pathogenic microbes led to an understanding of immune response to pathogens and medical advances in vaccinations and antibiotics. However, it is now being appreciated that most interactions humans have with microbes are either commensal (one organism benefits, while the other receives no benefit, but remains unharmed) or mutually symbiotic, where both organisms benefit in some way (8, 14, 15).

Within a successful host-microbe relationship, microbes may benefit the host by releasing molecules that inhibit pathologic microbes (8). This means that in addition to the chemical (e.g., intestinal mucosa containing immunoglobulins, cytokines, chemokines and antimicrobial peptides) and physical (e.g., gastrointestinal epithelium) barriers offered by the host immune system, the symbiotic microbes also assist the immune system in this defense (12). Microbes contribute to the gastrointestinal physical barrier defense by creating competition for nutrients against the pathogens (8,12), and also by modulating cytokine production (12).

Microbes may also attain nutrients for the host. Examples include the digestion of plant material (cellulose or host-derived mucin) by microbes required for their own growth, which are delivered to the microbes via the host's diet (8, 16). In return, the fermentation products can act as an energy source (e.g. butyrate as energy for colonocytes), gene expression regulators, and as inflammatory mediators to the host (8, 16). Other non-digestible materials such as inulin and fructo-oligosaccharides ingested by the host can act as energy sources (prebiotics) for the healthy microbes in our gut as well (16). Most interactions with microbes are not pathogenic, instead they are mutually symbiotic.

Evolution of normal host Immunity

Host immunity evolved in the presence of the microbiota. Due to a technique known as 16S ribosomal RNA gene sequencing much more accurate records of gut microbes can now be established when compared to only using culture based studies (8, 11, 16). 16S ribosomal RNA gene sequencing is beneficial taxonomically because it is found within most bacteria, has a conserved function and is large enough

to be detected (17). From 16S ribosomal RNA gene sequencing, it has been shown that microbial communities consist of a few phyla (8, 11, 16). Examples include Firmicutes, Bacteroidetes, Actinobacteria, Proteobacteria, Chlamydiae, Cyanobacteria, Defferribacteres, Deinococcusthermus, Fusobacteria, Spirochaetes, Verrucomicrobia (8, 11). Although, at first glance this may not seem like a lot of variation, at a species and strain level there is much diversity (8). This is thought to be due the many years of co-evolution between microbes and humans, resulting in only the successful symbionts persisting and evolving within the human gastrointestinal tract ecosystem (11).

In order to elucidate the interactions between the microbiota and the host, a technique called gnotobiology is commonly used (11). Gnotobiology is the study of germ-free animals while observing the consequences when re-colonized with certain microbes (11, 17). A germ free animal is one aseptically derived such that it has never had a microbiota. These studies have shown that the microbiota tremendously influence the host's immune system, intestinal epithelial cells, metabolism of materials present in gut, absorption of nutrients and even endocrine function (11). One example of the microbiota's effects on the intestinal epithelial cells comes from studies involving *Bacteroides thetaiotamicron*. When germ-free mice were populated with only these microbes and transcriptional responses were observed with DNA microarrays, complement reactive protein-ductin receptor expression was observed (11). This receptor is known to aid in epithelial repair (11). However, it is important to remember that mono-colonization studies are limited in their interpretation because it is the net function of microbial communities that drives host function.

Without the microbiota present in the gut the host organism suffers in the way of undeveloped tissues, underdeveloped immune function, malnutrition, and a serious vulnerability to infection (11). As demonstrated by germ-free animal experiments, a reduction in IgA antibodies, smaller Peyer's patches, and a reduced number of T cells has been found, all important contributors to a normal immune system (17). Furthermore, without the continuous presence of microbes in the gut, the antimicrobial substances usually ubiquitously present that act as part of the innate defense to control not only pathogens but all microbial populations are drastically reduced (17). All these changes culminate to produce an underdeveloped, immature immune system. This is demonstrated by evidence showing that with germ free mice, secondary immune organs (i.e. spleen and lymph nodes) also contain underdeveloped lymphoid follicles and reduced B and T cell populations (17, 10). Thus, the host immune system requires the presence of microbes in the gut to develop properly.

Where does hygiene fit in?

Now that the importance of the host-microbe relationship has been established, how hygiene gets involved can be explored. In 1989, David Strachan observed a huge increase in the amount of allergies such as hay fever and could not explain this huge increase with genetics alone, and thus, the hygiene hypothesis was born (19,21,26). If genetics alone could not explain this increase, then the environment must also be playing a role (21). He suggested that although increased hygiene (e.g. increased antibiotic use, vaccinations, and better cleaning procedures such as, pasteurization, sewage treatment and chlorination) has made great contributions to human health, it also altered our immune system such that we are more susceptible to the development of allergy and autoimmune disease (26). This "hygiene hypothesis" was advanced because such increases in allergies were not seen in undeveloped countries where hygiene was less controlled (22). Additionally, epidemiological studies in 1998 showed that atopic diseases such as asthma afflicted one in five children, with the numbers reaching epidemic levels today (22). Furthermore, autoimmune diseases such as type 1 diabetes, rheumatoid arthritis, and multiple sclerosis have also had an increased prevalence in developed countries as compared to undeveloped countries (22). In other words, the hygiene hypothesis suggests that the increased hygiene has altered the symbiotic relationship between the host and the microbiota to such an extent that the host's immune system becomes reactive to the host and harmless antigens.

It is important to note that the interactions occurring are complex, and with so many compounding variables it is difficult to say with certainty that the rise in allergy and autoimmune diseases is truly a result of increased antibiotic use and hygienic practices. For example, opponents to the hygiene hypothesis suggest that perhaps the increase in autoimmune diseases may be simply due to better techniques for diagnosing such conditions in the developed world (22). Nevertheless, with epidemiological studies showing a difference between prevalence of allergies and autoimmune diseases between developed and undeveloped countries, combined with the clear difference in hygiene and medical practices, the hygiene hypothesis is worth considering (26).

One of the first mechanisms put forward to explain the observation of increased allergies and autoimmunity in Westernized societies is an imbalance between Th1 and Th2 cells, to key immune cells known to play a role in both autoimmunity and allergy respectfully (26). This hypothesis was explained by the knowledge that most allergies are associated with an increase of the immunoglobulin E (IgE) antibody, which is secreted by B cells via assistance from Th2 cells (22). In undeveloped countries where early childhood infection is common, antigen-presenting cells such as dendritic cells promote Th1 differentiation through secretion of IL-12 and IL-18 (20). However, in developed countries where early childhood infection is low, Th1 differentiation is also low. Because Th1 and Th2 cells can inhibit each other's differentiation, a loss of Th1 cells may lead to a skewed Th2 population of cells in the body resulting in inappropriate production of IgE and development of allergic disease (22).

This hypothesis may be too simple, as there are many paradoxes that cannot be explained. For example, in undeveloped countries there are also high levels of parasitic infection as well as bacterial and viral infections. Parasites such as intestinal helminths, or worms, elicit a potent Th2 response. Another paradox also presents itself with the increased prevalence of autoimmune diseases observed in developed countries. This is because autoimmune diseases are known to be associated with an inappropriate Th1 response, and if there are truly a lower number of Th1 cells due to less infection, there should not be an increase in autoimmune diseases (20, 21, 22).

Due to the above conflicts, researchers began to explore the possibility that T regulatory (Treg) cells, an immune cell responsible for the down regulation of inflammation, may be responsible for the protection observed in undeveloped countries (20, 21, 25, 26). Perhaps helminths do increase the Th2 response and also induce Treg cells to secrete interlukin-10, a potent anti-inflammatory cytokine to assist in their own survival within the host (20, 25). However, the confusion only deepens with more conflicting evidence. With some groups suggesting findings that helminths offer protection from allergies with increased interlukin-10 production (20, 25), while others groups have reported no difference in cytokine production (23). To further convolute the investigation, a report done in the United States surveying approximately 20,000 Americans on physician diagnosed autoimmune and allergic disorders found that an increase in allergy was positively associated with an increase in autoimmune disease (24). This data weaken the hypothesis that an imbalance in Th1 and Th2 cells provokes allergy and autoimmune disease (21). Although this explanation is now out of date, it was one of the first attempts made to explain the phenomena of the hygiene hypothesis.

Since then other suggestions have been put forward with an updated understanding of the hygiene hypothesis. Currently it is defined as the idea that the increased incidence of allergic and autoimmune diseases in developed countries may be linked to a lack of exposure to microbes in early childhood. This allowed for the old friends hypothesis, another possible explination for the increased prevelance of autoimmunity and allergy in developed countries (21, 25, 26). The old friends hypothesis suggestes that in undeveloped countries, chronic exposure to pathogens, including parasites that can establish themselves in the host, induces a chronic and harmful aggressive immune response that can damage healthy host tissue (21, 25). The immune system has adapted by up regulating the number of dendritic cells able to sample antigens from these chronic pathogens (21, 25, 26). As a result of this increased sampling, dendritic cells enhance the differentiation and/or function of Treg cells to these pathogens (i.e., "Old Friends"). These Tregs are constantly present, and thus, prevent damaging immune responses (21, 25, 26). Quite coincidentally, with increased number of dendritic cells sampling antigens, they also sample self-antigens and allergens more often as well, and similar to their response to the continuous exposure to "Old Friends" there is a corresponding up regulation of Treg cells towards self-antigens and allergens as well (21, 25). Hence, the lower prevalence of autoimmune disease and allergies in undeveloped countries as compared to developed countries can be explained by dendritic cells increased presentation of self-antigens (21). Therefore it has been suggested that increased prevalence of allergy and autoimmunity may be the result of humans being able to adapt to their changing environment with technology much faster than our genetics are able to keep up (21). However, this hypothesis is not widely accepted on its own. To make this explanation more plausible it must be explained with the disappearing microbiota hypothesis (27, 28). In this hypothesis it is suggested that although antibiotics are a powerful tool we have to fight infection they also destroy the host's symbiotic microbial communities (27). This collateral damage to the host's symbiotic microbes is then hindered in its recovery by chlorination and pasteurization etc. that not only destroy pathogenic microbes but symbiotic ones in our environment as well (27). This lack of symbiotic microbes in the environment makes it difficult for the host to repopulate it's benifical microbial communities (27, 28). One example of a disappearing microbe is *Helicobacter pylori*, a microbe found in our stomachs (27, 28). Thus, this pattern of collateral damage to our microbiota and lack of symbiotic microbes in our environment slowly depletes our stores of healthy microbes (Hunter). The consequences of this are not only allergy and autoimmunity but obesity as well (27, 28). A key difference between the disappearing microbiota hypothesis and the previous two explanations put forward is that in the disappearing microbiota hypothesis emphasis is put on the lack of exposure to healthy microbes while the other two put emphasis on the lack of exposure to infectious disease (28).

These three hypotheses together prove that a complete mechanism to explain the epidemiological observation of increased autoimmunity and allergy in developed countries is not simple. However, they clearly outline the fact our increased hygiene in developed countries is altering the host's relationship with symbiotic microbes. Moreover, this altered relationship is affecting the host's immune system. I do not want to suggest that the use of antibiotics and hygienic practices such as chlorination of water are negative and thus should be stopped. The purpose here is to call attention and emphasize that the majority of our interactions with microbes is not pathogenic, and that we should be cautious and considerate of our microbial friends.

Conclusion

Over billions of years, we have co-evolved with the microbes that call us home. The gastrointestinal microbiota, a complex and dynamic ecosystem, is home to trillions of harmless microbes. These microbes are essential to the normal development and function of our immune system, and pivotal in absorbing nutrients and vitamins. Gnotobiotic animal studies have demonstrated the devastating effects on the host's ability to defend itself against various pathogens when the microbial community composition is altered.

It is clear that there is still much to learn. The mechanisms of the three hypotheses have proven to be elaborate, representing a challenge to find solid experimental evidence to explain the epidemiological patterns being observed, especially with regard to allergy and autoimmunity. Despite the complexity, it is clear that with a better understanding of our symbiotic relationship with microbes and our hygiene may affect the function of our immune system, it will be possible to incorporate better therapies for various ailments, and improve the quality of life for residents in both developing and developed countries.

Acknowledgments

Tremendous thanks to Dr. Trevor Day for his editorial advice, valuable discussion, guidance and continuing support throughout the process of writing this review.

References

[1] Hickmann C, The influence of cooperative Bacteria on Animal Host Biology: How have bacteria contributed to the evolution of multicellular animals? Cambridge, New York, USA: Cambridge Univ. Press; 2005.

[2] Lee YK, Mazmanian SK. Has the microbiota played a critical role in the evolution of the adaptive immune system? Science. 2010; 330(6012), 1768-1773.

[3] Gill SR, Pop M, Deboy RT, Eckburg PB, Turnbaugh PJ, et al. Metagenomic analysis of the human distal gut microbiome. Science. 2006; 312(5778), 1355-1359.

[4] Turnbaugh PJ, Ley RE, Hamady M, Fraser-Liggett CM, Knight R, et al. The human microbiome project. Nat. 2007; 449(7164), 804-810.

[5] Geuking MB, Cahenzli J, Lawson MA, Ng DC, Slack C, et al. Intestinal bacterial colonization induces mutualistic regulatory T cell responses. Immunity. 2011; 34(5), 794-806.

[6] Neish AS. Microbes in gastrointestinal health and disease. Gastroenterology. 2009; 136(1), 65-80.

[7] Hooper LV, Machpherson AJ. Immune adaptions that maintain homeostasis with the intestinal microbiota. Nat. Reviews Immunol. 2010; 10(3), 159-169.

[8] Dethlefsen L, McFall M, Relman DA. An ecological perspective on human microbe mutualism and disease. 2007; Nat. 449(7164), 811-818.

[9] Didierlaurent A, Sirard JC, Kraehenbuhl JP, Neutra MR. How the gut senses its contents. 2002; Cell Micrbiol. 4(2), 61-72.

[10] Machpherson AJ, Uhr T. Compartmentalization of the mucosal immune responses to commensal intestinal bacteria. Annals of the New York Academy of Sciences. 2004; 1029, 36-43.

[11] Chow J, Lee Sm, Shen Y, Khosravi A, Mazmanian SK. Host bacterial symbiosis in health and disease. Advances in Immunology. 2010; 107, 243-274.

[12] Servin AL. Antagonistic activities of lactobacilli and bifidobacteria against microbial pathogens. FEMS Microbial Rev. 2004; 28(8), 405-440.

[13] Stahl PD, Ezekowitz RA. The mannose receptor is a pattern recognition receptor involved in host defense. Curr.Opin. Immunol. 1998; 10(1), 50-55.

[14] Mazmanian SK, Liu CH, Tzianabos AO, Kasper DL. An immunomodulatory molecule of symbiotic bacteria directs maturation of the host immune system. Cell. 2005; 122(1), 107-118.

[15] Mazmanian SK, Kasper DL. The love-hate relationship between bacterial polysacharrides and the host immune system. Nat. Rev. Immunol. 2006 ;6(11), 849-858.

[16] Flint HJ, Duncan SH, Scott KP, Louis P. Interactions and competition within the microbial community of the human colon: links between diet and health. Environmental Microbiology. 2007; 9(5), 1101-1111.

[17] Janda JM, Abbott SL. 16S rRNA gene sequencing for bacterial identification in the diagnostic laboratory: pluses, perils, and pitfals. J. Clin. Microbiol. 2007; 45(9), 2761-2764.

[18] Smith K, McCoy KD, Macpherson AJ. Use of axenic animals in studying the adaption of mammals to their commensal intestinal microbiota. Semin. Immunol. 2007; 19(2), 59-69.

[19] Strachan DP. Hay fever, hygiene, and threshold size. BMJ (Clinical Research Ed.). 1989; 299(6710), 1259-1260.

[20 Romagnani S. Immunologic influences on allergy and the TH1/TH2 balance. The Journal of Allergy and Clinical Immunolog.2004; 113(3), 395-400.

[21] Rook GA. Review series on helminths, immune modulation and the hygiene hypothesis: the broader implications of the hygiene hypothesis. Immunology. 2009; 126(1), 3-11.

[22] Okada H, Kuhn C, Feillet H, Bach JF. The hygiene hypothesis or autoimmune and allergic disease: an update. Clinical and Experimental Immunology. 2010 ;160(1), 1-9.

[23] Boef AG, May L, Van Bodegom D, Van Lieshout L, Verweij JJ, et al. Parasitic infections and immune function: Effect of helminth infections in a malaria endemic area. Immunobiology. 2012; 706-711.

[24] Sheikh A, Smeeth L, Hubbard R. There is no evidence of an inverse relationship between TH2-mediated atopy and TH1-medicated autoimmune disorders: Lack of support for the hygiene hypothesis. The Journal of Allergy and Clinical Immunology. 2003; 111(1), 131-135.

[25] Rook G, Brunet L. Microbes, immunoregulation, and the gut. Gut. 2005; 54(3):317-320.

[26] Sironi M, Clerici M. The hygiene hypothesis: an evolutionary perspective. Microb Infect 2010; 12(6):421-427.

[27] Hunter P. The changing hypothesis of the gut. EMBO Rep. 2012; 13(6), 498-500.

[28] Blaser MJ, Falkow S. What are the consequences of the disappearing human microbiota? 2009; 7(12), 887-894.